Computational Studies of Sulphide-Based Semiconductor Materials for Inorganic Thin-Film Photovoltaics

Dufton, Jesse

Award date:
2013

Awarding institution:
University of Bath

Computational Studies of Sulphide-Based Semiconductor Materials for Inorganic Thin-Film Photovoltaics

Submitted by

Jesse T.R. Dufton

for the degree of Doctor of Philosophy of the
University of Bath
Department of Chemistry
July 2013

Contents

Abstract

New thin-film solar cell materials and a greater understanding of their properties are needed to meet the urgent demand for sustainable, lower-cost and scalable photovoltaics. Computational techniques have been used to investigate Cu_2ZnSnS_4, $CuSbS_2$ and $CuBiS_2$, which are potential absorber layer materials in thin-film photovoltaics. Their low cost, low toxicity and their constituent's relative abundance make them suitable replacements for current thin-film absorbers, which are CdTe or $Cu(In, Ga)(S, Se)_2$ based systems. Firstly, we have used hybrid Density Functional Theory (DFT) calculations to study $CuSbS_2$ and $CuBiS_2$. We calculate band gaps of 1.69 eV and 1.55 eV respectively, placing $CuBiS_2$ within the optimal range for a viable absorber material. The density of states for both these materials indicate that formation of electron hole charge carriers will occur in the Cu d^{10} band. Consequently, photoexcitation leads to the oxidation of Cu(I). Secondly, we have derived interatomic potentials which describe the complex structure of Cu_2ZnSnS_4 accurately. We find that the Cu/Zn antisite defect represents the lowest energy form of intrinsic defect disorder. For these antisite defects, we find a preference for small neutral defect clusters, which suggests a degree of self-passivation exists. Investigations of Cu-ion transport find V'_{Cu} migration is possible via a vacancy hopping mechanism. There are pathways which can be connected to give 3D long-range diffusion. Investigations of the Cu/Zn site disorder in Cu_2ZnSnS_4 find that configurations which are kesterite-like will dominate synthetic samples. However, perfectly ordered kesterite will not be formed due to entropic effects. The simulations indicate the stannite and stannite-like polymorphs are less favourable, and can only account for $\approx$2.5% of a sample. Investigations of the surfaces of Cu_2ZnSnS_4, suggest that the vast majority of the low index surfaces are dipolar and that only the (1 1 2), (0 1 0) and (1 0 1) surfaces have low surface energies.

Acknowledgements

There are many people who have helped during the course of this work, and I would like to thank them all.

I would especially like to thank my supervisor, Saiful Islam for his patience, guidance and helpful discussions throughout the course of this work. Aron Walsh for his help with the revised lone-pair model and VASP know-how. Pooja Panchmatia for her help with DFT and Densities of States. Chris Eames for his help with SOD and METADISE. Grahame Gardiner for help with LaTeX.

Diego Colombara for useful discussions on all of the materials which I have studied. Dan Staff for discussions on more general photovoltaics and quantum effects.

Also thanks to the remaining members of the MSI group (past and present) who have helped with their useful discussions and humour; David Tompsett, Craig Fisher, John Clark, Paul Weaver and Steve Stokes.

Thank you to Molly Thompson for her eagle eyes and Helen Alderson for some of the photographs.

This work was funded as part of the Engineering and Physical Sciences Research Council EPSRC's PV21 consortium, and would not have been possible without the help of the Materials Chemistry Consortium (MCC), which has provided access to HECToR, the UK's high-end computing facility.

Lastly, a final thanks goes to the unknown developers of some of the open source software that I have used. Special thanks go to the developers of VESTA and the KDE applet Jovie, which has proved to be invaluable.

Concentrating solar thermal power in Tibet; sunlight is focused onto a kettle using a pair of mirrors in the mountain monastery Gārdān Sì, Tibet, altitude 4500m ©*Molly Thompson 2006*.

List of Publications and Presentations

Publications

2012

- J.T.R. Dufton, A. Walsh, P.M. Panchmatia, L.M. Peter, D. Colombara and M.S. Islam, Structural and electronic properties of $CuSbS_2$ and $CuBiS_2$: potential absorber materials for thin-film solar cells, Physical Chemistry Chemical Physics, 2012, **14**, 7229-7233
- D. Colombara, L.M. Peter, K. Hutchings, K.D. Rogers, S. Schfer, J.T.R. Dufton and M.S. Islam, Formation of Cu_3BiS_3 thin films via sulfurization of BiCu metal precursors, Thin Solid Films, 2012, **520**, 51655171

Presentations

2011

- RSC Solid State Group Christmas meeting, Liverpool
  Poster: *Simulation studies of the potential photovoltaic material $CuSbS_2$*
- EPSRC PV21 meeting, OpTIC Glyndwr
  Talk: *Hybrid-DFT investigations of emerging photovoltaic materials*
- CCP5 Annual conference, Bath
  Poster: *Computational modelling of $CuSbS_2$ a potential thin-film solar cell material*
- Postgraduate symposium, Bath
  Talk: *Simulation studies of new solar cell materials*

2010

- SWCC meeting, Bristol
  Talk: *Atomistic simulation studies of the Cu_2ZnSnS_4 solar cell material*
- Chemistry Postgraduate Seminar, Bath
  Talk: *Atomistic simulation studies of new solar cell materials*

2009

- Postgraduate Symposium, Bath
  Poster: *Compuatational modelling of materials for solar cells*

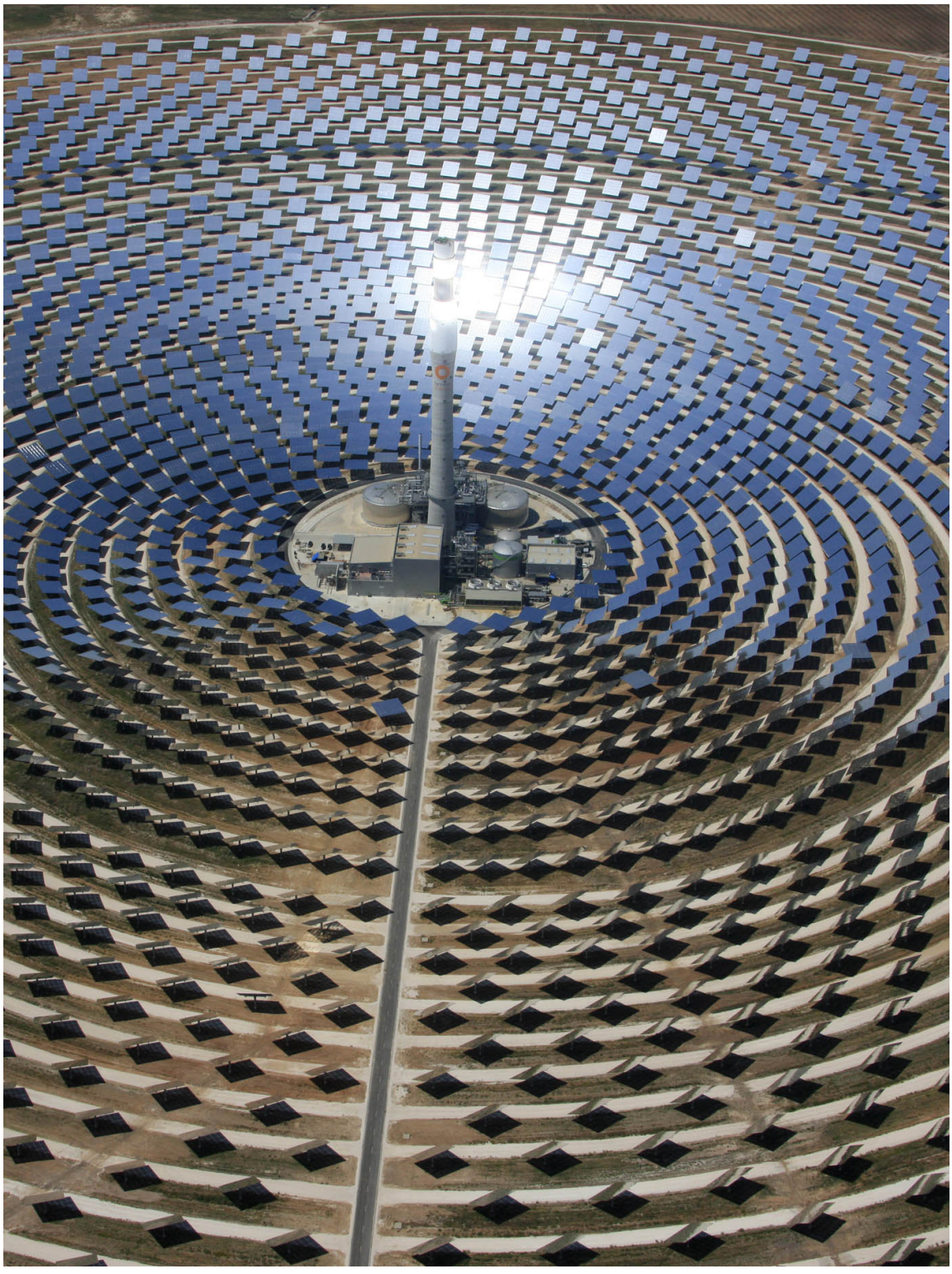

The Gemasolar power plant, Spain. A 19.9MW$_p$ concentrating thermoelectric solar power plant, concentric mirrors focus sunlight onto the tops of towers where the associated heat produces steam to spin a turbine. Excess heat can be stored in molten-salts to allow energy generation at night.

Chapter 1

Introduction

1.1 Background

Currently humanity is reliant on the combustion of fossil fuels for the majority of global energy generation. In recent decades this dependence has become a cause for considerable concern. This is primarily due to the fact that supplies of fossil fuels are limited, a desire for security of energy supply and concerns about global climate change as a result of continued CO_2 emissions. Clearly there is a pressing need to break our dependence on fossil fuels by restructuring our energy generation infrastructure, so that we can provide energy which is both "clean" and "sustainable".

Breaking the dependence upon fossil fuels is therefore one of the principal challenges of the 21^{st} century. It will necessitate greatly increased use of renewable energy technologies. A range of such technologies already exist. Wind, solar, hydroelectric, tidal and geothermal power generation have all been commercialized. However, to date they provide a small fraction of our total energy production. All current technologies will need to be developed further in order to move away from fossil fuel generation. It is hoped that the development of photovoltaic solar power technology will contribute significantly to this shift.

Photovoltaics have several advantages over competing forms of renewable energy technology. Firstly they have a comparatively high energy production density[1], and are also relatively easy to integrate into urban environments, which is helped by the fact that their operation is silent and they are less obtrusive than wind turbines. Photovoltaics also require less maintenance than other technologies due to the lack of mechanical motion.

Photovoltaic technology does have limitations, with two main problems impairing their wide spread adoption.

(i) The efficiency of mass produced photovoltaic cells leaves considerable room for improvement.

(ii) The high cost of the cells, both in energy and economic terms.

For photovoltaics to contribute significantly towards energy production, new designs and materials for photovoltaics need to be developed. These photovoltaics will need good efficiency ($\geq$10%)[2] but primarily they will need to be relatively inexpensive and easy to mass produce.

Further progress in these technologies requires the development of new materials which are able to confer performance and economic advantages. Therefore fundamental materials research is key, as only with a detailed understanding of the current materials and the processes which lead to their functionality will further improvement be possible.

1.2 Historical Development of Photovoltaic Devices

Photovoltaic devices or solar cells are photo-electrochemical devices which directly convert the energy of photons incident upon them into useful electrical power. It is important to distinguish them from solar thermal panels which use the thermal energy provided by the sun to heat water for domestic use, and from concentrating solar thermal power which extends this concept to commercial energy generation by using mirrors to focus light in order to vaporize water and spin a turbine yielding electricity.

The development of photovoltaics began in 1839 with the discovery of the photovoltaic effect by Bequerel[3], who observed that light incident upon a silver coated platinum electrode placed in electrolyte caused an electric current to flow. It was then 37 years until this effect was demonstrated in the solid state by Adams and Day[4]. In 1876 they found that when selenium was contacted with metal electrodes, a rectifying junction was formed which spontaneously generated a current when exposed to light. In the years that followed the photovoltaic effect was demonstrated in a range of solid state systems including the sulphides of lead and thallium. However the action of these early photovoltaics was not understood until the work of Goldman and Brodsky identified that the rectifying action was due to the presence of a barrier which restricted the flow of charge carriers[5].

The development of solid state photovoltaics did not progress significantly until the 1950's when developments in semiconductor technology as a result of the microelectronics industry led to the production of the first solar cells based upon crystalline silicon wafers. These first generation photovoltaics exploit the specialized electronic effects which are exhibited when a junction between p-type and n-type materials is created.

1.2.1 Operation of p-n Junction Solar Cells

Control over materials' properties is sometimes achieved by the deliberate introduction of impurities whose presence significantly alters the physical, chemical or electronic behaviour of the material. This process is known as doping and is a common tool used to control the properties of semiconductors such as silicon. The addition of dopants replaces atoms/ions from the host lattice with dopant atoms/ions. In semiconductors aliovalent dopants (dopant ions which possess a charge different to that of the host which they replace) are used to change electronic properties.

Taking the example of doping Si; donor dopants such as P can be introduced to dramatically increase the conductivity of the silicon. When undoped, the conductivity is relatively low as the charge carriers are thermally excited electrons. Adding small amounts of donor dopants increases the conductivity dramatically as the extra electron(s) partially fill(s) the conduction band. Materials doped in this way are referred to as n-type as the majority charge carriers are negative (electrons), but it is important to note that the material remains charge neutral. If acceptor dopants are introduced (in the case of Si, B or Al are often used) then not only is the conductivity increased but the nature of the charge carriers changes. Acceptor doping introduces electron-holes into semiconductors, which have an effective positive charge and consequently materials doped in this way are known as p-type.

When an n-type and a p-type material are placed in contact with one another, charge carrying species of both types diffuse across the junction in an attempt to level the concentration gradient of electrons, Figure 1.1. There is an excess of electrons in a n-type material relative to the p-type so when the two are connected electrons flow from the n-type material, across the junction into the p-type material. Simultaneously the holes are diffusing in the opposite direction. As the electrons and holes diffuse across the junction they come into contact with each other and recombine. This means that near the junction there is a section of the material in which the concentration of charge carriers is greatly reduced. This region has a variety of names. In the context of this explanation it makes sense to refer to it as the depletion layer/region but it is also commonly referred to as the space-charge layer/region. Due to the loss of charge carriers as a result of recombination the crystal in the depletion layer is left with a charge. The n-type half of the depletion layer has lost a portion of its electrons so now bears a positive charge, and the p-type half has gained extra electrons which have filled the holes and now bears a negative charge. The presence of these two charged regions sets up an electric field which acts across the junction. The strength of this electric field is key to the operation of a solar cell as its strength determines the maximum voltage for the cell, the open circuit voltage (V_{oc}), typically in the range 0.5-1.0 V.

When layers of p-type and n-type material are combined together along with a set

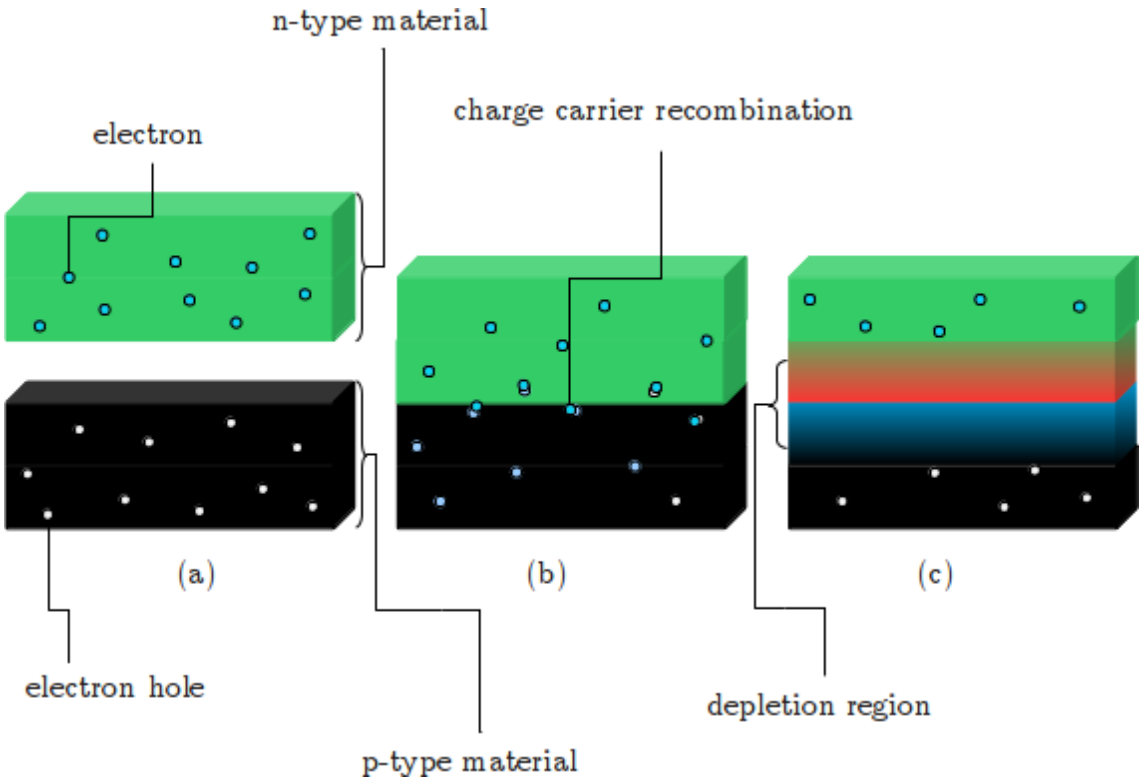

Figure 1.1: Schematic showing the creation of the depletion region in three stages. Stage (a) shows isolated p-type (black) and n-type (green) materials which contain mobile charge carriers; electron-holes (white) and electrons (blue) respectively. In stage (b) the p-type and n-type materials are contacted and a proportion of the charge carriers recombine. This recombination creates the positive (red) and negative (blue) sections of the depletion region shown in stage (c).

of electrical contacts and a substrate to provide mechanical support, we have the makings of a solar cell. Figure 1.2 shows the structure of a typical thin-film solar cell. When the solar cell is irradiated, the incident photons pass through the transparent n-type window and buffer layers, and then enter the p-type absorber layer. Photons whose energy is in excess of the material's band gap generate photo-excited electrons and an associated electron-hole when they are absorbed. The electric field which exists across the junction separates the electron and hole by inducing the excited electron to diffuse across the junction into the n-type material. Once this separation has occurred the only way in which the excited electron can recombine with a hole is if it travels around an external circuit, and in doing so it provides useful current.

1.2.2 Shockley-Queisser Limit

There are a range of unavoidable losses which limit the efficiency of solar cells dramatically. The magnitude of these losses was first calculated for a limiting the-

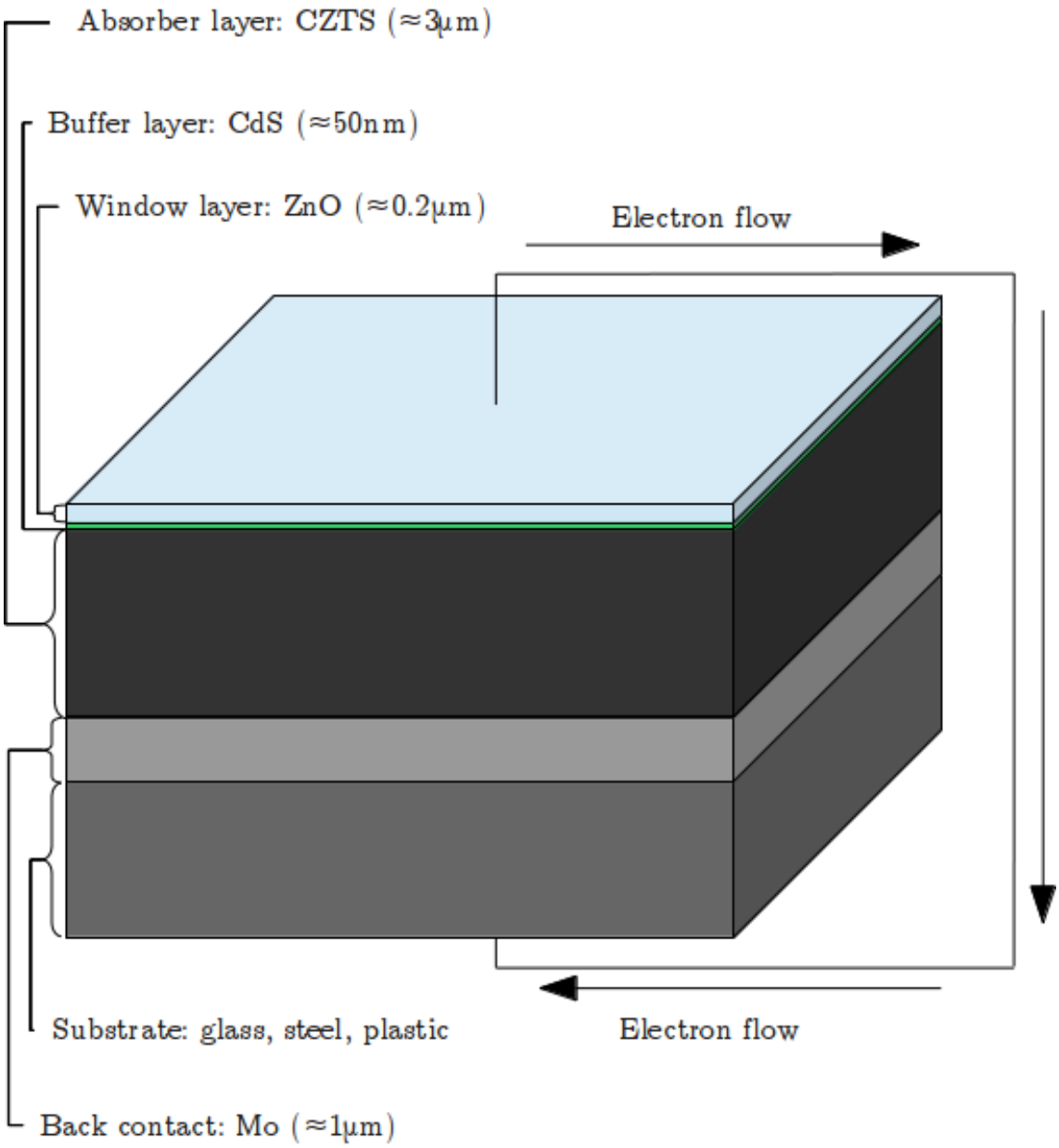

Figure 1.2: A cross-sectional schematic of a thin-film solar cell, showing the layers of which it is comprised. A Cu_2ZnSnS_4 (CZTS) absorber layer is shown. However, devices based around CIS/CIGS absorbers retain the structure shown.

oretical case by Shockley and Queisser in 1961[6]. They referred to the limit as the "detailed balance limit of efficiency", but subsequently it is commonly referred to as the "Shockley-Queisser" limit. Shockley and Queisser calculated the efficiency limit for a single junction cell to be ≈30%. This value is subject to small changes as it is dependent on the magnitude of the material's band gap, but this limit is the result of three main loss processes, as follows:

(i) **Recombination losses**

For photo-excited electrons to provide useful work they must be separated from the concurrently created electron-hole and forced to pass around an external circuit. This is not always the case. In most solar cell absorber materials the rate of hole transport is significantly slower than that of electron transport. Therefore it is possible for an excited electron diffusing towards the junction under the influence of the electric field to encounter a hole, from a separate excitation, travelling in the opposing direction. When this occurs the excited electron and hole recombine, and the potential for useful power resulting from that electron is lost. This effectively de-couples irradiance intensity from a cell's power yield because as the irradiance intensity is increased the probability that excited electrons will encounter holes whilst diffusing to the junction increases.

Materials which have faster hole transport are less susceptible to this limit. Therefore GaAs based cells are compatible with solar concentrators. These use mirrors to focus light onto the device increasing the irradiance intensity. This approach is not cost effective for silicon or thin-film cells as with increased irradiance this recombination effect dominates.

(ii) **Black-body radiation**

All matter not at absolute zero emits black-body radiation. A portion of the energy incident upon a photovoltaic device will be re-emitted as black-body radiation which cannot be utilized by the cell. As the intensity of black-body radiation is related to the temperature of the material, the temperature of the cell is inversely proportional to its performance. As the cell is warmed by the radiation source, the losses due to the cell's black-body radiation increase.

(iii) **Spectral losses**

The sun emits photons with a range of energies. However when photovoltaics absorb solar radiation they can only absorb a certain portion of this spectrum. Photons whose energy is insufficient to promote an electron from the valence to conduction band are not absorbed. While other photons have energies in excess of the band gap this excess energy is not useful for electrical power production as it is lost to thermalisation, heating the cells and exacerbating the losses due to black-body radiation, which are described above. Clearly a material's band gap is a key parameter determining the potential efficiency of a solar cell. If the band gap is wide, less energy will be lost to thermalisation. However, a greater proportion of the spectrum will not be absorbed at all. If the band

gap is narrow, then the majority of incident photons will be absorbed, but each photon will only deliver a small amount of energy. A compromise must be sought and for single-junction solar cells the optimum band gap is 1.5-1.2 eV[2, 7].

(iv) **Other losses**

The losses described above are not the only ways in which real photovoltaics lose efficiency. Electrical losses in cables and due to the sheet resistance of window layers as well as current leakage to module supports represent some of the other major areas of concern.

1.2.3 Strategies to Raise the Shockley-Queisser Limit

While it is not the focus of this work, it should be noted that there are several interesting and ingenious strategies which aim to raise the maximum efficiency of photovoltaic devices.

The first is multi-junction photovoltaics which are effectively a stacked array of solar cells with varying band gaps. The cells with the widest band gap are closest to the irradiation source so that the high energy photons are "creamed off" and those which do not have sufficient energy continue on to the next cell which has a narrower band gap. Multi-junction cells are able to achieve higher efficiencies than single-junction devices with a theoretical maximum of $\approx$76% and a current record of $43.5 \pm 2.6\%$[8]. However they are complex and expensive to produce and consequently are only used in space operations e.g. for powering satellites where the need for efficiency outweighs the extra cost.

Another interesting approach is the use of up/down-shifting films which are added as an extra layer on top of a single-junction cell. In up-shifting films the energy of two low energy photons (which individually do not possess energy in excess of the band gap) is combined together and a photon of higher energy is emitted. This higher energy photon has sufficient energy to be absorbed by the cell. In down-shifting films high energy photons are split into two photons of lower energy. Provided these can still be utilized, it allows the generation of two photo-excited electrons from one incident high energy photon. Unfortunately both these approaches are still being developed, and stringent encapsulation will be needed to avoid the quenching effect of O_2 ruining the effectiveness of up-shifting films[9].

1.2.4 Non-silicon Solar Cells

It has already been noted that the major advances in solar cell technology came with the introduction of crystalline silicon solar cells. The growth of the micro-electronics industry impacted greatly on the development of these cells. However,

there are some significant problems with silicon-based solar cells. Arguably, the most important are the limited opportunities for cost reduction. As silicon has an indirect band gap its absorption coefficient is relatively weak and so comparatively large amounts of material are needed in order to absorb the majority of incident photons. Also the purity of silicon required is extremely high as the key electronic effects for photovoltaic action result from doping. Hence even small quantities of undesired impurities can dramatically degrade material performance. The necessity for premium silicon purity increases cost as the processes needed to remove impurities present in feedstocks require high temperatures and high vacuum pressures. The result of these issues is that ≈50% of the photovoltaic module cost is attributed to the silicon wafers[2].

The limitations in cost reduction potential described above have led to the development of several alternative types of solar cell. The most closely related class, and the one which will be the focus of this work, is that of thin-film photovoltaics.

Although not the focus of this thesis, two other technologies of current interest include:

Dye-sensitised solar cells. These split the roles of light absorption and charge transport. Energy conversion is achieved through light-induced electron transfer from dye molecules (typically Ru-based) to their semiconducting substrate (typically anatase-TiO_2), with subsequent collection of the injected charge carriers. Dye-sensitised solar cells promise to be inexpensive to mass produce. However currently they suffer from low efficiency and stability problems relating to the need for encapsulation. Examples of relevant literature include references [10–14].

Organic photovoltaics (OPV). This emerging class of photovoltaics is based on polymer/fullerene blends or halogen-doped organic crystals. It is facile to form interpenetrating polymer networks which greatly reduces the carrier path length needed to access the junction. The ability to functionalise the polymers gives great control over the electronic and material properties. Such cells could become easy to mass produce and cheap, as well as being mountable on flexible substrates. However like dye cells OPV currently suffer from low efficiency and problems with stability. Examples of relevant literature include references [15–23].

1.3 Thin-film Photovoltaics

The term thin-film photovoltaics covers a range of photovoltaic device structures. The majority of these are silicon-free, with the exception of amorphous-silicon devices. As our focus is on the development of materials which enable a move away from silicon, we only consider the established thin-film technologies based on CdTe and $Cu(InGa)(SSe)_2$ alongside the emerging technologies stemming from the use of the materials Cu_2ZnSnS_4 (CZTS), $CuSbS_2$ and $CuBiS_2$.

Silicon-free thin-film photovoltaic devices are based on the use of semiconducting p-type absorber materials which have a direct band gap and associated strong absorption coefficient. The operation of a thin-film cell is analogous to that of a silicon-based device and is shown in Figure 1.2. The principal advantage that thin-film cells have over silicon is that the higher absorption coefficient reduces the thickness of the absorber layer which helps to reduce materials' costs. Also, thin films are much more resilient to the presence of defects than silicon. This reduces the need for energy intensive and costly purification processes, again helping to reduce costs.

Currently there are two non-silicon-based thin-film technologies which are dominant: Chalcogenide-based cells, where the absorber is a doped variant of $CuInSe_2$ (CIS), and cells which use CdTe as the absorber layer.

1.3.1 CdTe Based Cells

CdTe cells initially utilized n-type CdTe in conjunction with either In or Cu_2Te, as it is difficult to form p-type CdTe with doping[24]. However, this arrangement was eventually replaced with a p-type CdTe combined with n-type CdS. Steady improvements in CdTe cells have led to efficiencies >17%, which are achieved with polycrystalline samples. It is thought that grain boundaries can actually facilitate the collection of photo-excited charge carriers rather than acting as centres for recombination[25].

Industrially, CdTe-based solar cells benefit from inexpensive constituents and from the fact that modern fabrication techniques make production of moderately efficient cells comparatively facile. Large scale investment by First Solar has driven the cost of electricity produced by CdTe cells down to \$1/W. However, heavy investment in the scale up of silicon technologies in Asia has significantly impacted on the competitiveness of CdTe[26].

1.3.2 $Cu(In, Ga)(S, Se)_2$ (CIGS) Based Cells

The structure of the I-III-VI semiconductor $CuInSe_2$ is similar to that of the cubic zinc-blende form of the II-VI binary sulphide ZnS. In Zinc Blende ZnS, the group II and group VI ions form two inter-penetrating fcc networks, which leads to both the cations and anions being in a tetrahedral coordination. In the I-III-VI materials such as $CuInSe_2$ the replacement of two group II ions with a pair of group I and III ions means that there are a variety of possible structures which result from different cation ordering schemes. There are two configurations which are favoured, as they maintain local charge neutrality by ensuring that each anion bonds to two group I and two group III cations. The chalcopyrite structure, which is adopted by $CuInSe_2$ (shown in Figure 1.3), in which the group I and III ions are arranged in alternating

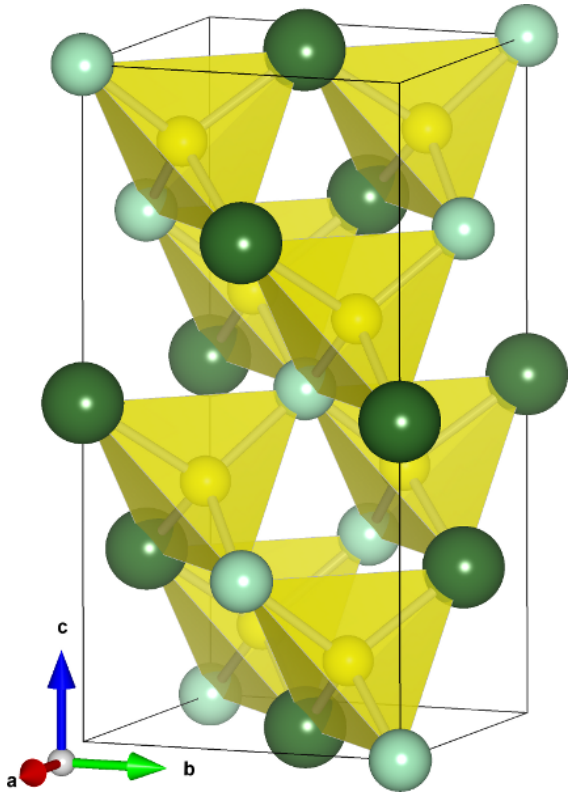

Figure 1.3: The structure of $CuInSe_2$, showing Cu (light green), In (dark green) and S (yellow).

planes parallel to the (201) direction, and the structure of $CuAuSe_2$, in this case the group I and III planes are aligned with the (001) direction.

The use of chalcogenide-based materials in solar cells was first studied by Wagner *et al.*[27], quickly followed by the work of Kazmerski *et al.*[28–30]. It was initially thought that the system's complexity would hinder its development. However, chalcogenide-based cells have proved to be very successful, and efficiencies >20% have been achieved. This is in part due to the doping of pure $CuInSe_2$ with Ga^x_{In} / Al^x_{In} and S^x_{Se} to form $Cu(In_{1-x}Ga_x)(Se_{2-y}S_y)$ (CIGS). The introduction of these dopants allows tuning and gradation of the material's band gap. Addition of Ga narrows the band gap, whereas inclusion of S to replace Se widens the gap. It is difficult to achieve a homogeneous addition of Ga into CIS films. It is therefore common for CIS films to be Ga poor at the "top" of the layer, near the junction and for the concentration to increase towards the "bottom" of the cell. It is also common for the distribution of S to be non-uniform. However, in this case the films are S rich near the junction.

As we have noted, these dopants affect the band gap and this non-uniformity in their distribution leads to a gradation of the band gap from top to bottom of the material. This helps the performance of the cell as higher energy photons at the top of the cell do not lose as much of their energy to thermalisation as would otherwise

be the case, and some lower energy photons that would normally not be absorbed are collected in the Ga rich region[2].

1.3.3 The Need for New Thin-film Materials

The CdTe and CIGS based technologies have developed the field of thin-film photovoltaics. However, there are significant materials' cost and availability constraints with both technologies, and it is thought that these will hamper the widespread deployment of these thin-films in the long term.

Figure 1.4 shows the price and abundance in the earth's crust of a range of elements which are relevant for photovoltaics. One of the most notable features is the scarcity of Te. The limited supply of this element, which is essential to CdTe based cells means that while these cells are currently inexpensive it will be impossible to deliver them in sufficient quantity to provide a step-change in photovoltaic energy production.

Turning now to the case of $Cu(InGa)Se_2$ based cells, Figure 1.4 shows that the prices of In and Ga are comparatively high. This is due not only to their scarcity but to their utility in a range of electronics and microelectronics applications. The price of these elements contributes considerably to the cost of CIGS based solar cells and limits the potential for cost reduction, which will be needed to enable photovoltaics to be deployed ubiquitously.

In order to meet the demand for increased photovoltaic solar power, new materials are needed which are both inexpensive and sustainable/scalable. This work aims to investigate the fundamental properties of some candidate compounds, specifically the band gap of $CuBiS_2$ and $CuSbS_2$ as well as the favourability of ion migration and the extent of polymorphism in Cu_2ZnSnS_4.

1.3.4 Ternary Cu−Bi−S and Cu−Sb−S Based Materials

There are a range of ternary copper sulphide based semiconductor materials[31–40] which are under investigation as possible replacements for $CuInSe_2$ in thin-film solar cells. This is due to their appropriate band gaps and high absorption coefficients, in conjunction with the fact that they are comprised of inexpensive and non-toxic materials. There are a number of stoichiometries of the Sb and Bi containing copper sulphides which are of interest:

$CuSbS_2$ (chalcostibite) and its Bismuth analogue $CuBiS_2$ (emplectite), which are isostructural (orthorhombic space group *Pnma*). The structures (shown in Figure

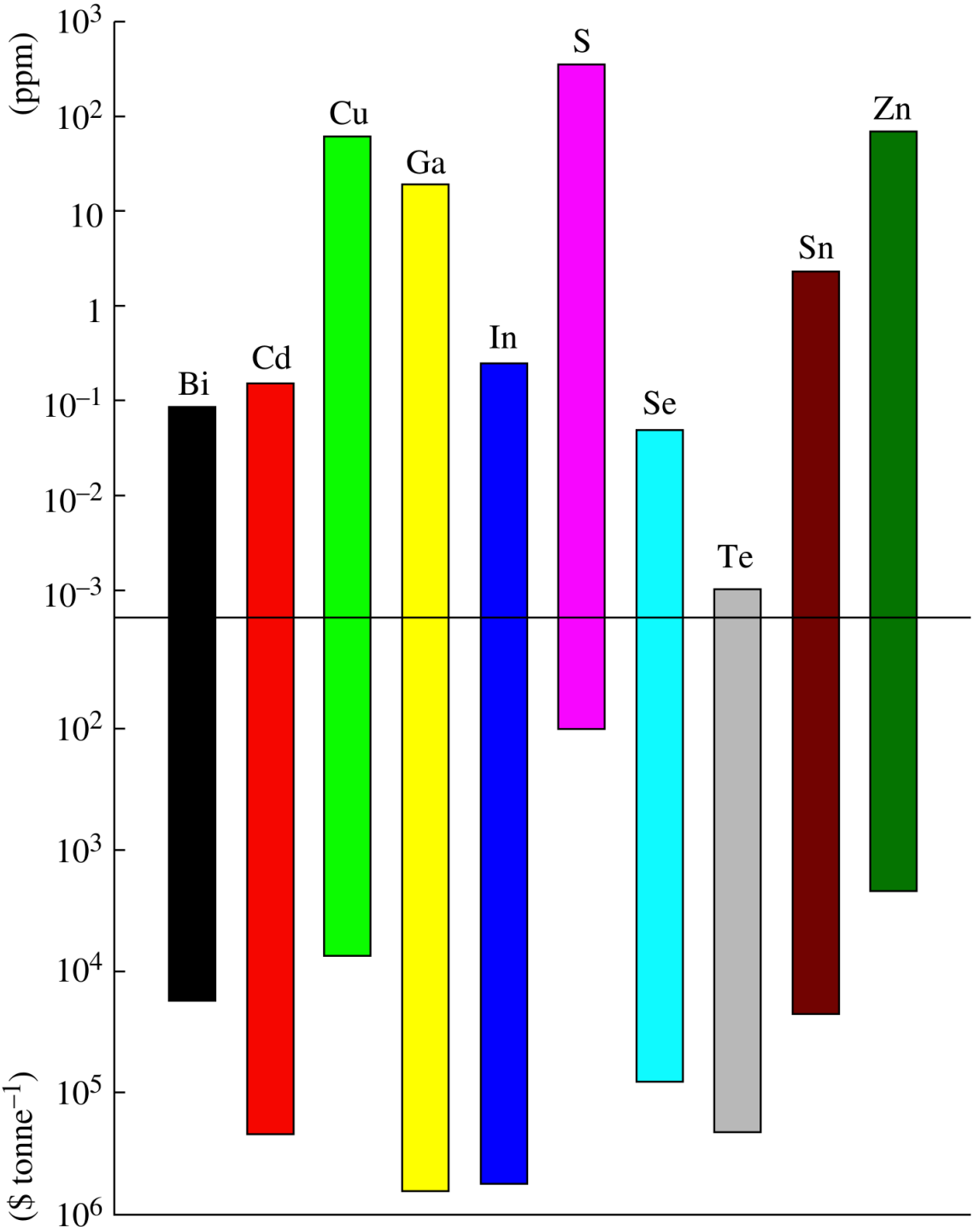

Figure 1.4: Abundance in earth's crust (upwards) and cost (downwards) of a range of elements relevant to photovoltaics. Note the use of logarithmic scales. (Reproduced from the work of Peter[7]).

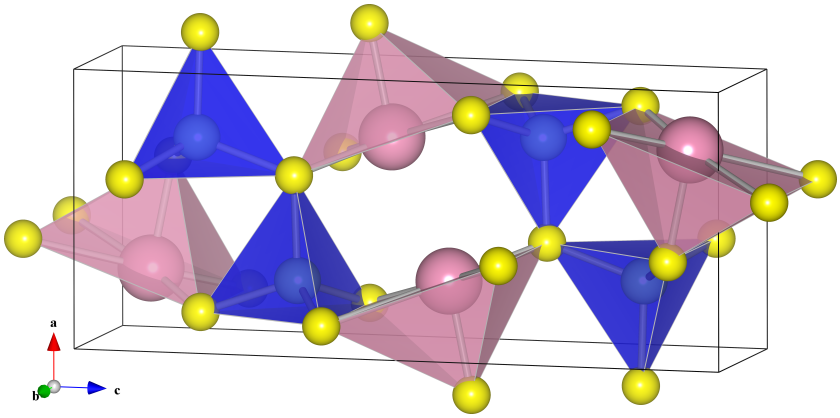

(a) $CuBiS_2$

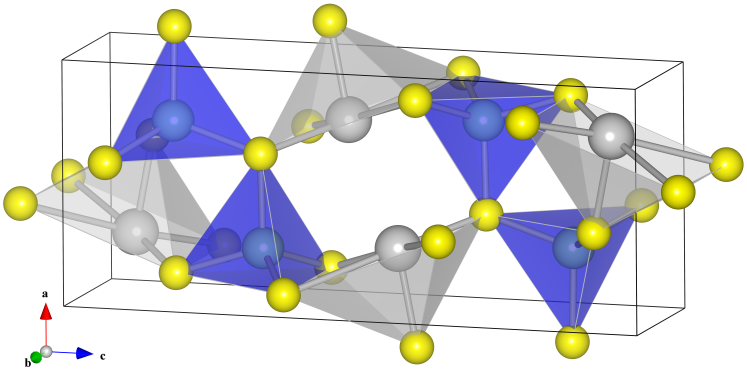

(b) $CuSbS_2$

Figure 1.5: Structure of the ternary copper sulphide based PV materials $CuBiS_2$ and $CuSbS_2$ showing; Bi (pink), Sb (grey), Cu (blue) and S (yellow).

1.5) are composed of square pyramidal MS_5 units (M = Sb/Bi) which edge-share to form continuous MS_2 units aligned with the b axis. These continuous units are separated by CuS_4 tetrahedra so that the base of the square pyramidal units are aligned to face one another, thus directing the Sb/Bi lone pair electron density into the void separating the MS_5 units.

In chapter 3, hybrid density functional theory calculations are used to investigate the structural and electronic properties of both $CuSbS_2$ and $CuBiS_2$. Cu_3SbS_3 (Skinnerite)[41–43] and Cu_3BiS_3 (Wittichenite)[44] both possess highly distorted crystal structures (shown in Figure 1.6). The structures belong to the $P\ 2_1/c$ and $P\ 2_1\ 2_1\ 2_1$ space groups respectively. Like the $CuMS_2$ compounds their structure is based around MS_5 units. However, in both Cu_3SbS_3 and Cu_3BiS_3 these units are highly distorted, as can be seen in Figure 1.7 where they shown in isolation. Strictly they are trigonal-bi-pyramidal, although it is more intuitive to describe them as highly distorted square pyramids, in which the cation is recessed from the basal plane of the pyramid. These MS_5 units are connected by CuS_3 units which are in

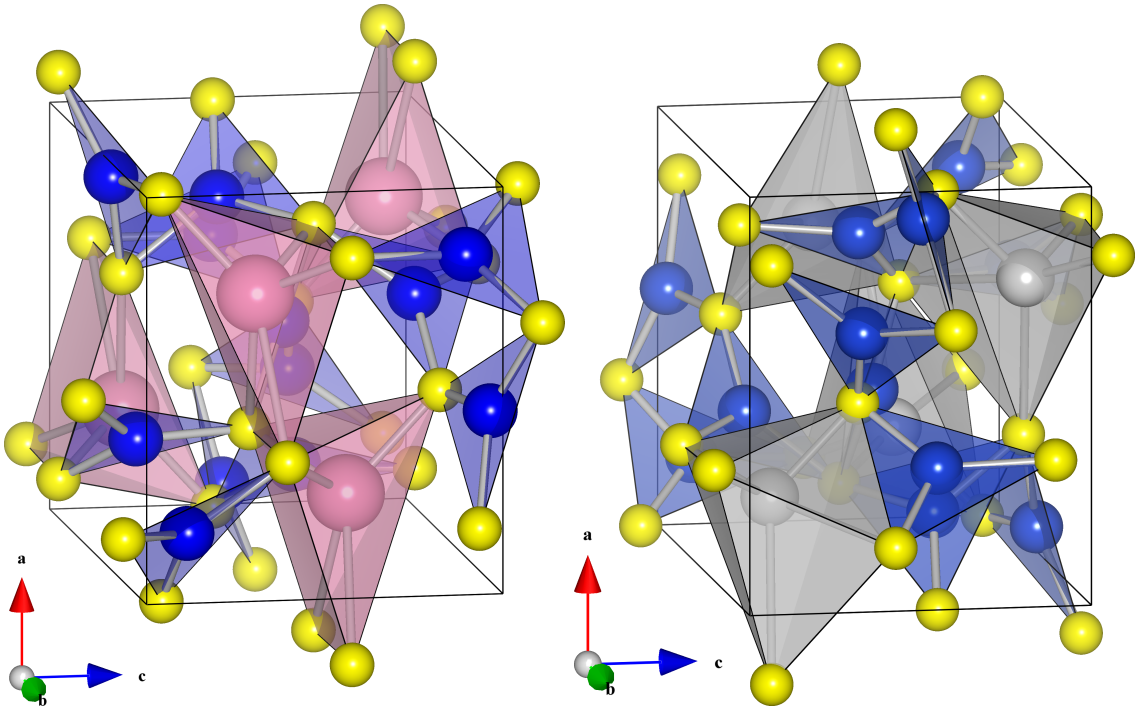

(a) Cu_3BiS_3 (b) Cu_3SbS_3

Figure 1.6: The ternary copper sulphide based PV materials Cu_3BiS_3 and Cu_3SbS_3 showing; Bi (pink), Sb (grey), Cu (blue) and S (yellow).

an unusual near trigonal planar configuration.

Early work on this class of materials was performed by Rodriguez-Lazcano *et al.* [40] who reported a method to produce $CuSbS_2$ thin-films through a solid state reaction involving thin-films of Sb_2S_3 and CuS. Work by Rabhi *et al.*[39] investigated the structural, optical and electrical properties of $CuSbS_2$ thin-films grown by thermal evaporation and related the effects of substrate heating conditions to these properties. Manolache *et al.*[34] examined the influence of precursor concentration on the morphology and the structure of $CuSbS_2$ thin-films obtained from aqueous solutions. However, in the case of $CuBiS_2$ and $CuSbS_2$, the fundamental properties and performance have not been fully characterized. It is clear that the underlying bulk and electronic structure of ternary copper sulphide materials are complex, but are crucial to the greater understanding of their structure-property relationships and PV behaviour. In chapter 3 the results of a series of calculations aiming to address these fundamental issues are discussed.

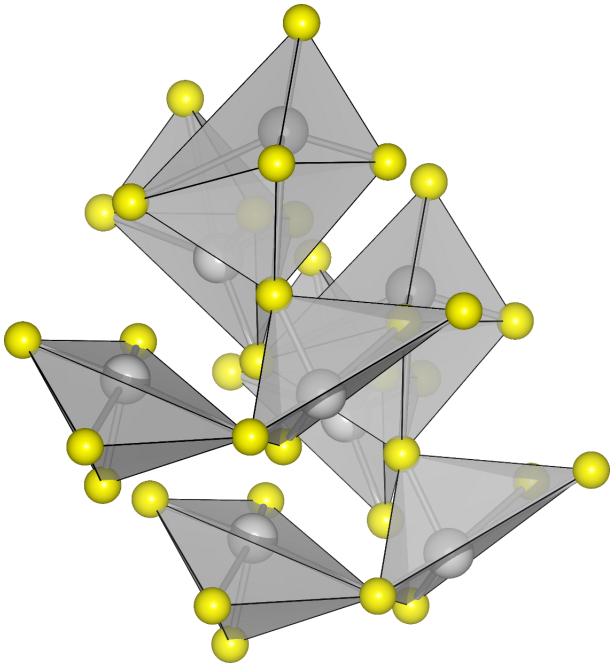

Figure 1.7: The highly distorted SbS_5 units of Cu_3SbS_3. Strictly they are trigonal bi-pyramidal, but it can be seen that two of the faces are nearly in-plane, leading to a near square based pyramid.

1.3.5 Cu_2ZnSnS_4 (CZTS) Based Materials

Compounds based on Cu_2ZnSnS_4 (CZTS) and its Se analogue $Cu_2ZnSnSe_4$ (CZTSe) have been the most successful of the range of materials investigated as replacements for CIGS. Unlike the ternary materials described in section 1.3.4 where the In^{3+}/Ge^{3+} are replaced by either Sb^{3+} or Bi^{3+}, in CZTS two 3+ ions are replaced by Zn^{2+} and Sn^{4+}.

CZTS has been shown to have a high optical absorption coefficient ($\approx 1\times10^4 cm^{-1}$) as well as a direct band gap of near optimum energy (1.44-1.51 eV) and also exhibits p-type conductivity[45–48]. Devices utilising alloys of CZTS and CZTSe have achieved record efficiencies in excess of 10%[49, 50].

The structure of Cu_2ZnSnS_4 (shown in Figure 1.8) is similar to that of ZnS being based around inter-penetrating tetrahedral networks corresponding to both the cations and anions. Due to the number of constituent species in Cu_2ZnSnS_4, polymorphism is a significant issue and there are a wide range of polymorphs resulting from the arrangement of the cations. Of these, the lowest energy structure is that of the kesterite polymorph (space group $I\bar{4}2m$) and this is often discussed in relation to the stannite polymorph (space group $I\bar{4}$) (which takes its name from the related material Cu_2FeSnS_4). Figure 1.8 shows the unit cells for both the kesterite and stannite structures, which are shown with anion-centred polyhedra to emphasise the tetrahedral coordination.

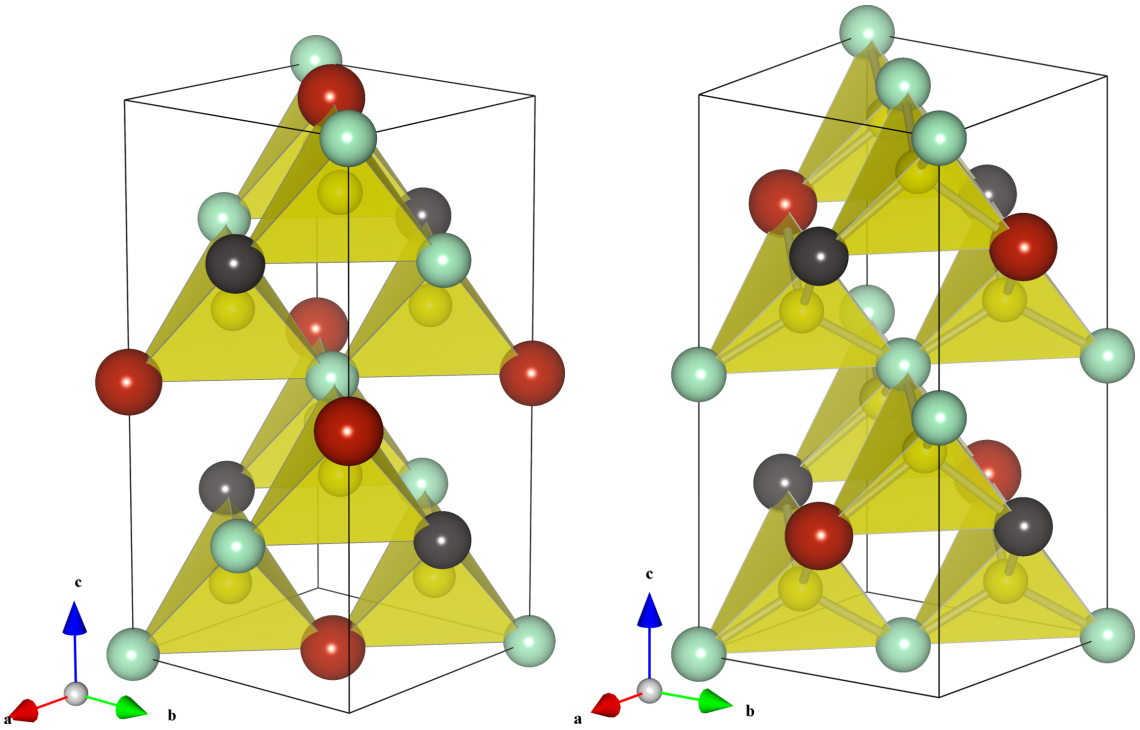

(a) Kesterite (b) Stannite

Figure 1.8: The kesterite and stannite polymorphs of Cu_2ZnSnS_4 showing; Cu (green), S (yellow), Zn (black) and Sn (red).

In all polymorphs we see that the cations are arranged in layers parallel with the *ab* plane. The arrangement of the cations within these layers differentiates the polymorphs from one another. In kesterite, layers containing Cu-Zn alternate with layers containing Cu-Sn. Whereas in stannite, layers comprised of Cu-Cu alternate with layers containing Zn-Sn. Kesterite and stannite are not the only polymorphs of Cu_2ZnSnS_4. There is a wide range of symmetry-inequivalent cation ordering schemes, and the effects of this cation disorder on the observed polymorphs of Cu_2ZnSnS_4 is investigated in chapter 5. As well as the effects of cation disorder, the defect chemistry and ion transport properties of Cu_2ZnSnS_4 have been studied and this is detailed in chapter 4.

(a)

(b)

(c)

Examples of photovoltaics integration into the urban environment.

Chapter 2

Computational Methodology

2.1 Introduction

Computational simulation techniques have proven to be an extremely useful and accurate tool in many fields not least in the solid state chemistry of energy materials [51]. The ability of modelling methods to complement experimental investigations is now well recognised. In this chapter the fundamentals of computer simulation methods based on energy minimisation and applied to bulk crystal structures and defect chemistry are outlined. Further reviews on computational methodologies are available elsewhere[52–57], these underpin this chapter.

2.2 Energy Minimization

In chemical systems the potential energy of a system can be defined as a function of the positions of all the component entities. In solid state systems this means that the system's potential energy is dependent on the positions of all its constituent particles. This function is referred to as the potential energy (hyper) surface. Given its multi-dimensional nature it is difficult to evaluate and/or visualise the complete surface. However it is possible to visualise subsets/sections of this function which are relevant to chemical processes and this can greatly enhance the understanding of a system.

Some of the most important features of the potential energy surface correspond to the stationary points of the function. There are two stationary points of principal interest:

Minima: These points represent stable chemical structures. In some systems multiple minima exist each corresponding to separate chemical structures (polymorphs). The lowest energy minimum is the "global minimum", this corre-

sponds to the thermodynamically favoured structure. All other minima are referred to as "local minima".

Saddle-points: These are the points of highest energy which lie along a path connecting two minima, where the path is chosen to minimise the energy difference between the minima and the saddle-point. These points correspond to transition states between two stable configurations.

Both minima and saddle-points have first derivatives of the potential energy function with respect to distance which are zero. However, it is possible to distinguish between these stationary points on the basis of the properties of their second derivatives with respect to distance. The eigenvalues of the Hessian matrix of second derivatives are all positive at a minimum whereas at a saddle point one (and only one) of the eigenvalues is negative.

Finding the stationary points on the potential energy surface is extremely important in computational chemistry, and there are a range of energy minimisation algorithms which allow this to be done. However the complex nature of the potential energy function can cause problems and inefficiency when using these algorithms. This is rectified by assuming that the potential energy function is harmonic (quadratic) close to the minima.

The energy minimisation algorithms fall into two categories, those that rely solely on the first order derivative vector, and those which utilise second derivative information which requires calculation of the Hessian. While calculating the Hessian introduces extra computational expense, this is often off-set by the fact that second order techniques converge on the minimum value in a reduced number of iterations.

2.2.1 Steepest Descent Minimisation

In this method the minimum is found iteratively. From a point on the potential energy surface the direction which affords the largest decrease in energy is selected and the point for the next iteration is placed upon a line defined by this direction according to;

$$\mathbf{x}_{i+1} = \mathbf{x}_i + \alpha_i \mathbf{r}_i \tag{2.1}$$

Where $\mathbf{x}_i$ is the starting configuration, $\mathbf{r}_i$ is a vector defining the direction with the largest negative gradient about the point $\mathbf{x}_i$ and α_i defines the distance along the vector $\mathbf{r}_i$ to move.

The magnitude of α_i must be found by performing a line search. Unfortunately as the potential energy function has been assumed to be quadratic the point returned by this first iteration will not be the minimum of the true potential energy function. Hence the iterative process continues until this point is found.

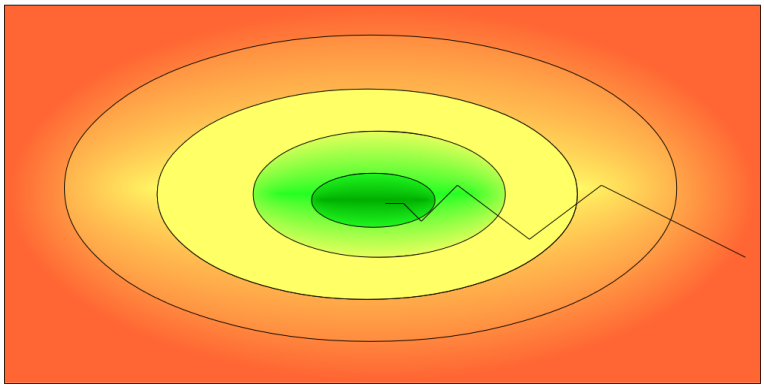

Figure 2.1: Schematic representation of the potential energy well surrounding a minimum and the path taken by a steepest descent minimisation

As the point $\mathbf{x}_{i+1}$ is a minimum on the line between $\mathbf{x}_{i+1}$ and $\mathbf{x}_i$ the gradient at this point has no contribution from the vector. Consequently the direction of the next iteration will be orthogonal to the current iteration. This causes the steepest descent to take a zig-zag path to the minimum as shown in Figure 2.1. Clearly this is inefficient and hence higher order search techniques are often employed.

2.2.2 Conjugate Gradient

The conjugate gradient algorithm is closely related to that of steepest descent. However unlike the steepest descent, which minimises the energy along a series of lines orthogonal to one another, the conjugate gradient method takes a set of orthogonal search directions $\mathbf{d}_n$ and minimise the energy once.

$$\mathbf{x}_{i+1} = \mathbf{x}_i + \alpha_i \mathbf{d}_i \tag{2.2}$$

Minimising with respect to all of the search directions locates the minimum. Convergence is unaffected by the shape of the potential well and the zig-zag path of steepest descent is not replicated. However the problem with the conjugate gradient method is defining a set of suitable search directions. If the Cartesian directions are used, to find α_i the energy of the minimum would be needed clearly this is not known. This problem can be addressed if a set of directions which are orthogonal in the space defined by the Hessian are used.

2.2.3 Newton-Raphson

This is a widely used technique for finding minima. Unlike the steepest descent and conjugate gradient methods, it uses first and second order derivative information

when searching. The algorithm generates the updated iteration according to;

$$\mathbf{x}_{i+1} = \mathbf{x}_i - \left(\frac{\mathbf{g}_i}{\mathbf{H}_i} \right) \tag{2.3}$$

Here $\mathbf{g}_i$ is the gradient of the potential energy function at the point $\mathbf{x}_i$ and $\mathbf{H}_i$ is the Hessian for the same point. For functions which are perfectly harmonic the Newton-Raphson approach only requires one step to locate the minimum. As previously noted, real systems are not perfectly harmonic, and so the Newton-Raphson method must also be applied iteratively in order to locate the minimum. When the configuration being evaluated is close to a minimum assuming that the potential well is harmonic is valid and the Newton-Raphson method converges quickly. However if the configuration being evaluated is some way from a minimum then the potential energy surface will not be harmonic and so Newton-Raphson may struggle to find the minimum. It can be more efficient to begin an energy minimisation using either steepest descent or conjugate gradient techniques and then switch to a Newton-Raphson optimisation scheme once the trial configuration is close to the minimum.

While the use of the Hessian in Newton-Raphson techniques allows faster convergence when near to a minimum calculating and then inverting the Hessian is relatively computationally expensive. Fortunately it is not necessary to recalculate the Hessian from scratch at every iteration of the optimisation process, as the inverted Hessian generally changes little between consecutive iterations. It is therefore common to use the update scheme of Broyden-Fletcher-Goldfarb-Shanno[58], which amends that Hessian in order to mimic the changes caused by re-calculation with every iteration. It is then only necessary to recalculate the Hessian according to specific criteria:

- If a set number of iterations has been performed without re-calculation of the Hessian.
- When the energy difference between two consecutive iterations is larger than a cut-off value.
- When no minimum can be found in the current search direction.
- If there is a large difference between the search vector and the gradient vector.

2.3 Transition States

As well as finding energy minima it is also useful to be able to locate saddle-points in the potential energy surface, as the energy barrier (difference between lowest energy minimum and saddle-point) determines the frequency of certain chemical events. In the case of this work, the magnitude of the energy barrier can determine the

energetic cost and therefore the frequency of ion migration through a material of interest. In order to gain insight into these chemical events we must be able to locate the saddle-point of the potential energy surface. There are two principal ways in which this has been done.

2.3.1 Constrained Minimisation

This is a very simple technique in which an event such as ion migration is broken up into a set of independent points which represent the event. In this case the migration of an ion from point A to point B is broken up into steps in which the migrating ion is placed along the path connecting points A and B. Each of these "images" is then subject to an independent energy minimisation with the constraint that the migrating ion is fixed in the plane perpendicular to the direction of migration. The energy of each image is then found and plotted to give a schematic representation of the energy barrier for this particular ion migration. The size of the energy barrier is simply the difference in energy between the start point and the image of highest energy. However there are several problems with this method. First, fixing the migrating ion in a plane perpendicular to the direction of migration is only simple in very high symmetry scenarios where the direction of ion migration is parallel to a lattice vector. In lower symmetry systems where the lattice vectors are not parallel with the Cartesian directions it can be difficult to fix the ion in an appropriate plane. Secondly, all the images along the migration path are independent from one another. This means that in some cases the ions relax away from the preceding and following images and the path can become discontinuous. If this happens then the images have certainly missed the saddle-point and the energy barrier predicted will be inaccurate. These problems are addressed via the use of the Nudged Elastic Band (NEB) method.

2.3.2 Nudged Elastic Band (NEB)

The Nudged Elastic Band method [59–61] considers a series of images along a migration path in a similar fashion to the constrained minimisation approach. However unlike the constrained minimisation these images are not independent of one another. The migrating ion in each image is coupled to the position of the migrating ion in the preceding and following images by harmonic springs. It can help to think of the series of connected springs forming a continuous elastic band which connects the initial and final points of the migration path. Along this elastic band there is a series of evenly spaced beads which are the images of the migrating ion. When the NEB minimisation takes place, the energies of all the images are relaxed simultaneously. The effect of this is that our hypothetical elastic band will lie along the minimum energy path which connects the initial and final points. The fact that the springs connect the images means that the problem of images relaxing away

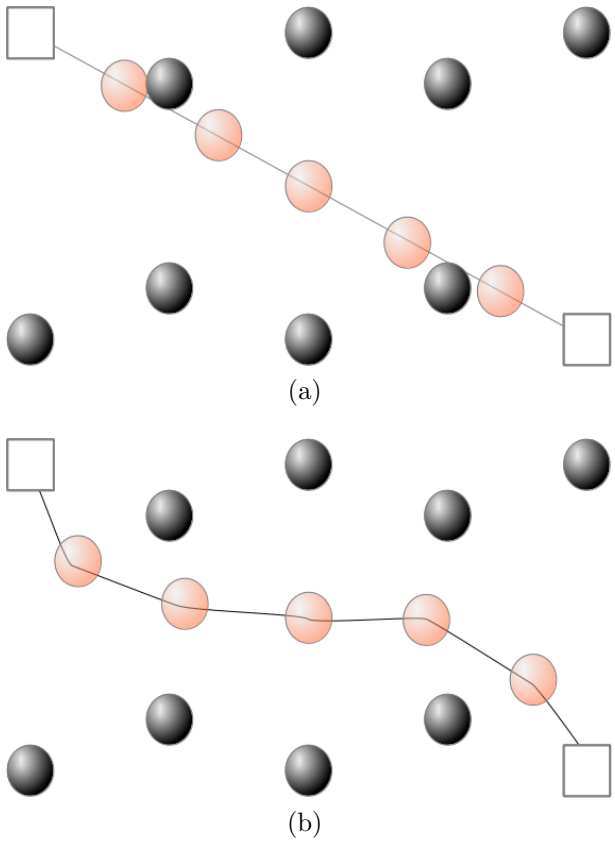

Figure 2.2: Schematic of the Nudged Elastic Band approach before (a) and after (b) minimisation. Lattice ions (black spheres), vacant lattice sites (hollow black squares) and images of the migrating ion (pink spheres) connected by the "elastic band" are shown.

from one another to form a discontinuous path is avoided. Also, the fact that other than the connecting spring no constraints are specified means that the NEB method easily finds relatively complex migration paths which are curved or "S" shaped for example. These are difficult to investigate with constrained minimisation methods.

2.4 Site Occupancy Disorder

Site Occupancy Disorder, defined as "the non-periodic occupation of lattice sites in a crystal structure" [62], is a feature of many solid state systems, such as solid-solutions and non-stoichiometric materials. Study of these materials using commonly used experimental techniques, such as XRD, is challenging as most methods applicable to

periodic systems are restricted to studying a material's average properties. Consequently, computational studies are a valuable tool for investigation of these systems, as they are not affected by this limitation. However, when investigating site occupancy disorder, considering the entire configurational space is intractable for all but the simplest of examples, as the vast number of ordering combinations/permutations means that the computational cost becomes unmanageable.

One approach to overcome this is to use Monte Carlo methodology to study a representative subset of configurations, however due to the incomplete sampling of the configurational space there is a possibility that important configurations will be missed. An alternative approach, which has been employed in this work, is to reduce the number of configurations using the symmetry of the system. Configurations which are related by symmetry are duplicates of one another and so it is possible to evaluate the entire configurational space through evaluation of the symmetry-inequivalent configurations only.

To do this we have employed the Site Occupancy Disorder code of Grau-Crespo *et al.*[62]. In this approach the complete configurational space for a given supercell of sample material is generated. The symmetry operators of the parent lattice are then used to select all symmetry-inequivalent configurations. These symmetry-inequivalent configurations are then evaluated with either atomistic or *ab initio* energy minimisation techniques in order to determine the configurational energy spectrum.

The extent to which any given configuration is expressed, referred to as the configurational probability, is considered to be determined by a Boltzmann-like probability. This is calculated neglecting the effects of external pressure and vibrational contributions utilising the calculated lattice energy of each configuration E_m in conjunction with the configuration's degeneracy Ω_m according to:

$$P_m = \frac{\Omega_m}{Z} e^{-\left(\frac{E_m}{k_B T}\right)} \tag{2.4}$$

Where $m = 1, 2, ..., M$ (M = number of symmetry-inequivalent configurations), k_B is the Boltzmann constant and Z is the configurational partition function[63] defined by:

$$Z = \sum_{m=1}^{M} \Omega_m e^{-\left(\frac{E_m}{k_B T}\right)} \tag{2.5}$$

As previously noted, the effects of external pressure, and vibrational contributions to the enthalpy, have been omitted. Therefore, the enthalpy associated with a configuration is simply the configuration's lattice energy. The enthalpy per formula

unit of a configuration (H) is calculated as an average in the configurational space according to:

$$H = \frac{1}{N}\sum_{m=1}^{M} P_m H_m = \frac{1}{N}\sum_{m=1}^{M} P_m E_m \tag{2.6}$$

Here N is the number of formula units of material present in the super-cell. We can use the partition function Z described above to access the configurational energy G and entropy S:

$$G = -\frac{1}{N} k_B T \ln Z \tag{2.7}$$

$$S = \frac{H - G}{T} = -\frac{1}{N} k_B \sum_{m=1}^{M} P_m \ln \frac{P_m}{\Omega_m} \tag{2.8}$$

It is possible to calculate average properties for a system which is comprised of a mixture of symmetry-inequivalent configurations using:

$$A = \sum_{m=1}^{M} P_m A_m \tag{2.9}$$

Where A is the average property, P_m is the configurational-probability of configuration m and A_m the property of configuration m.

Further detail on the implementation of the SOD code is available in reference[62].

2.5 Atomistic Simulation Techniques

2.5.1 Interatomic Potentials

In "atomistic" or "potential based" simulations we require a set of equations which describe the energetics of interatomic interactions. For simulations of solids the most important of these relate to the calculation of a solid's lattice energy. The most general expression defining the lattice energy U_{lat} is a series expansion of terms representing the interaction of increasingly large sets of atoms;

$$U_{lat} = \sum_{i=1}^{N}\sum_{j>i}^{N} V_{ij}(r_{ij}) + \sum_{i=1}^{N}\sum_{j>i}^{N}\sum_{k>j}^{N} V_{ijk}(r_{ijk}) + \sum_{i=1}^{N}\sum_{j>i}^{N}\sum_{k>j}^{N}\sum_{l>k}^{N} V_{ijkl}(r_{ijkl}) + ... \tag{2.10}$$

Here N is the total number of atoms in the system. Higher order terms have decreasingly significant contributions to the total energy, therefore it is common to truncate the series.

This expression was modified by Born[64] who took the two body term and segregated it into two component terms, one describing the long-range Coulombic interactions and the second describing the short range effects resulting from the interaction of electron clouds.

$$U_{lat} = \sum_{i=1}^{N}\sum_{j>i}^{N} \frac{q_i q_j}{4\pi\epsilon_0 r_{ij}} + \sum_{i=1}^{N}\sum_{j>i}^{N} \phi_{ij}(r_{ij}) \tag{2.11}$$

The first component of this equation is simply an expression of Coulomb's law. The second component, the short range interaction ϕ_{ij} has been parametrised in several ways. The Morse[65] and Lennard-Jones[66] potentials are often used to describe the short range interactions of covalent bonds and neutral atoms respectively. However in this work the ϕ_{ij} term is represented by the following Buckingham potential[67], which has been used successfully for a variety of modelling studies of oxides and sulphides[68–72].

$$\phi_{ij}(r_{ij}) = Ae^{-\left(\frac{r_{ij}}{\rho}\right)} - \frac{C}{r_{ij}^6} \tag{2.12}$$

As noted above, the two-body interactions give the most significant contribution to the lattice energy and hence equation 2.10 is often truncated after this term. However while the contributions to the lattice energy are small the use of higher order terms (three and four body) can be necessary to properly describe the bond angles and vibrational modes of some materials. As the two body terms do not have angular dependence they can fail to suitably describe these quantities. Like the two body terms, there are many parameterisations of the three body terms all of which introduce some energy penalty for distorting a bond angle away from some prespecified equilibrium value. The most common form of these three-body potentials when considering ionic solids is:

$$\phi_{ijk} = \frac{1}{2}k(\theta - \theta_0)^2 \tag{2.13}$$

where θ and θ_0 are the angle between i, j & k and the equilibrium angle between i, j & k respectively. k is a force constant which determines the magnitude of the energy penalty associated with angular distortion. However in the potential-based simulations of Cu_2ZnSnS_4, one of our potential models is based on the work of Wright *et al.*[72] on ZnS. We have followed the description of the ZnS_4 tetrahedra with an exponentially decaying three-body potential of the following form:

$$\phi_{ijk} = \frac{1}{2}k(\theta - \theta_0)^2 e^{-\left(\frac{r_{ij}}{\rho_{ij}}\right)} e^{-\left(\frac{r_{ik}}{\rho_{ik}}\right)} \tag{2.14}$$

Here θ, θ_0 and k are as for equation 2.13, and the constants ρ_{ij} and ρ_{ik} determine the rate at which the potential decays with distance.

2.5.2 Ewald Summation

It is difficult to evaluate the Coulombic term for solids as their periodic nature means that the Coulomb energy is given by a conditionally convergent series. This is due to the fact that, while the interaction between ions i and j decays with $1/r_{ij}$ the number of interacting ions increases with $4\pi r^2$ (surface area of sphere). Thus the energy density of a crystal increases with distance.

The most common approach for dealing with this problem in solid materials was devised by Ewald[53]. In this method the problem is tackled by converting the conditionally convergent Coulomb series into the sum of two convergent series, via the temporary addition of a set of screening charges. These screening charges have spherical symmetry and surround each particle i. They effectively neutralise the long range interactions as they have a charge which is the inverse of the particle which they surround. The most common form of the screening charge is a Gaussian given by;

$$\rho_i(r) = \frac{q_i \alpha^3}{\pi^{\frac{3}{2}}} e^{-(\alpha^2 r^2)} \tag{2.15}$$

where q_i is the charge on a particle to be screened, r gives position with reference to the centre of the screening charge and α is an arbitrary parameter which controls the width of the Gaussian distribution. The electrostatic interactions exerted by these screened charges decays rapidly with distance. Consequently the Coulombic interactions between screened charges can be easily evaluated in real space.

The effects of the screening charges must be considered. Fortunately they can be evaluated easily in reciprocal space where they form a smooth periodic function.

2.5.3 Parry Summation

While the Ewald method is used in systems exhibiting three-dimensional periodicity, for systems where the periodicity is only in two dimensions (e.g. surfaces) the Parry summation method must be used to calculate the Coulombic interactions. In this method the crystal is considered to consist of a series of charged planes, each extending to infinity. The loss of periodicity in one direction means that interactions must be split into in-plane and out-of-plane vectors. Unlike a 3D-periodic system the sum of these vectors need not equal 0. Hence extra terms in the reciprocal part of the Ewald function must be considered. Detailed discussion is given in Heyes *et al.*[73].

2.5.4 The Shell Model

The accuracy and utility of interatomic potential models is helped greatly if a treatment of polarisability is included. Polarisation affects the energy minimisation of a material's bulk structure and it is key to calculating certain material properties including phonon frequencies, refractive indices and dielectric constants. A description of polarisation is also important for defect simulations as the introduction of point defects gives rise to polarisation of the ions surrounding the defect.

The simplest description of polarisability is given by the point polarisable ion model. This model represents the dipole μ which is induced by an electric field E in terms of the polarisability α;

$$\mu = E\alpha \tag{2.16}$$

However this model is not applicable to interatomic potential simulations as the polarisability is not coupled to the short-range interactions described above. Consequently the most common description of polarisability utilised in interatomic potential simulations is the shell model devised by Dick and Overhauser[74], described diagrammatically in Figure 2.3. In this model each ion is represented by a pair of point charges which are described as the core and shell. The magnitude of these charges is defined by;

$$q_{ion} = X + Y \tag{2.17}$$

Where q_{ion} is the ion's charge and X & Y are the charges of the core and shell respectively. The core and shell can be thought of as representing the nucleus and valence electrons of the ion respectively (Although in some cases an ion's shell carries a positive charge.). All of the mass of an ion is assigned to the ion's core leaving the shell with no mass. The core and shell are coupled together by a harmonic spring of

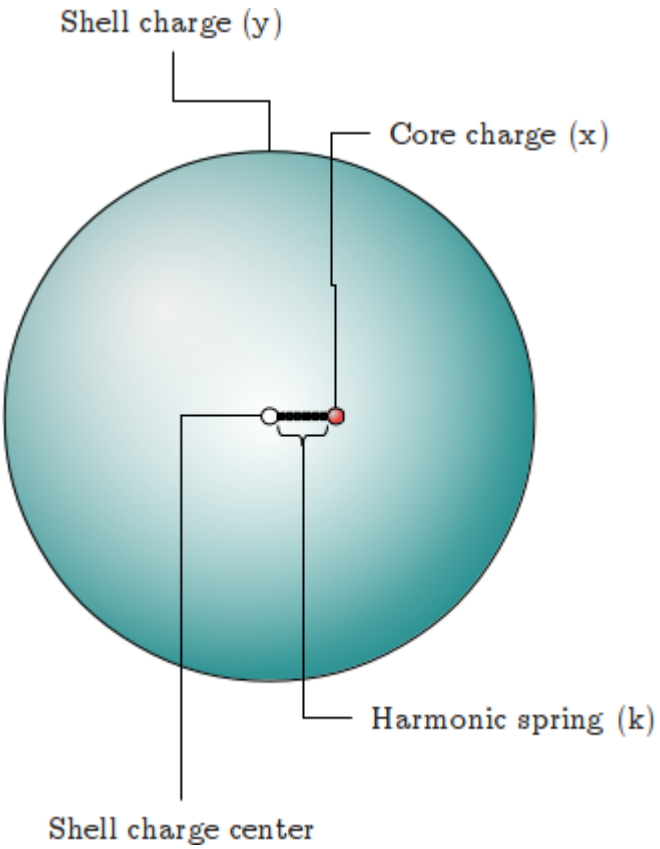

Figure 2.3: Schematic of the shell model

force constant k. The short-range interactions between an ion and its surrounding species are only applied to the ion's shell, and the Coulombic interactions between an ion's core and shell are neglected. This allows the core and shell to become spatially displaced from one another. As both are charged this leads to the expression of a dipole for the ion and hence a representation of polarisation in the system, the magnitude of which can be evaluated using:

$$\alpha = \frac{1}{4\pi\epsilon_0}\left(\frac{Y}{k}\right) \tag{2.18}$$

Where ϵ_0 is the permittivity of free space, Y is the charge of the shell and k is the force constant associated with the spring connecting core and shell. There are no values of Y, X and k which are able to adequately describe the polarisation of every ion and so these quantities are treated as parameters and must be defined for each distinct interatomic potential model.

2.5.5 Defect Modelling

Real crystals are not perfect, as entropic considerations mean that a small level of intrinsic defects will always be present. Moreover some chemical processes of great interest are directly related to the presence and behaviour of defects in real systems, with Ag interstitial migration in AgCl given as a good example.

When the defects under study exist in relatively large quantities it is possible to model them using a super-cell approach. We consider the defect(s) to be part of the bulk crystal structure. We create a super-cell which contains a fraction of defects which approaches that seen in experiment, then utilise energy minimisation techniques as normal. Depending on the concentration of defects, each defect will be able to feel the effects of the defects in periodic images. While this approach is very useful for systems with large degrees of defect disorder, in systems with low defect concentrations or when energies for single defects are needed in order to calculate defect formation energies, this approach is not ideal. This is because the size of super-cell needed is inversely proportional to the defect concentration, so when the defect concentration approaches the dilute limit the size of super-cell required rapidly becomes extremely large and unmanageable. The most common approach to model defects at infinite (or near-infinite) dilution with interatomic potentials is that of Mott & Littleton[75].

In the Mott-Littleton approach the crystal is subdivided into two spherical regions which are centred on the defect (or the centre of the defect cluster). The innermost region (region 1) is allowed to relax and is subject to a full energy minimisation utilising the short-range interactions defined by the interatomic potential(s). The energy of the defect must be converged with respect to the size of this volume as determined by the sphere's radius, this means that at the very least the spherical

region's radius must be greater than the distance cut-off of the interatomic potential for the defect species.

Region 2a is a hollow sphere which concentrically extends region 1. It is a buffer between region 1 and the outermost region (region 2b). Region 2a contains a set of atoms which are relaxed but only with respect to the force acting upon them as result of the defect. An alternative approach is to relax the region 2a ions according to the force resultant from all the ions in region 1.

Region 2b extends from the surface of the sphere defining region 2a to infinity. In this region the effect of the defect is weak and so it is adequate to employ quasi-continuum methods. The ions experience a dielectric response to the charge of the defect.

2.6 Electronic Structure Techniques

Electronic structure calculations provide a range of ground-state properties of a system, some of which cannot be calculated using empirical methods. This is the principal advantage of electronic structure calculations. While both methods are able to estimate the total energy of a system, semi-empirical methods cannot predict properties such as: a system's charge distribution and bonding, band structure and orbital occupancies. For this work the use of electronic structure methods will be necessary to complement semi-empirical results in order to gain an understanding of relationships between a systems chemical structure and its electronic properties. In relation to solar cell materials the electronic property of primary interest will be a material's band gap and how this can be tuned by altering the chemical structure. In order to achieve this insight we intend to use Density Functional Theory (DFT) as the electronic structure method of choice.

2.6.1 Density Functional Theory

Density Functional Theory (DFT) is a first principles electronic structure technique which is used to investigate the properties of many-electron systems. It is particularly popular with condensed matter physicists and computational chemists due to its lack of computational expense when compared to other electronic structure techniques.

DFT's development is principally attributed to Walter Kohn, who received the 1998 Nobel Prize in Chemistry for the development of Density Functional Theory[76], although the Thomas-Fermi model [77, 78] was the first model to include some of the basic elements of DFT. The Hohenberg-Kohn theorems represent the major

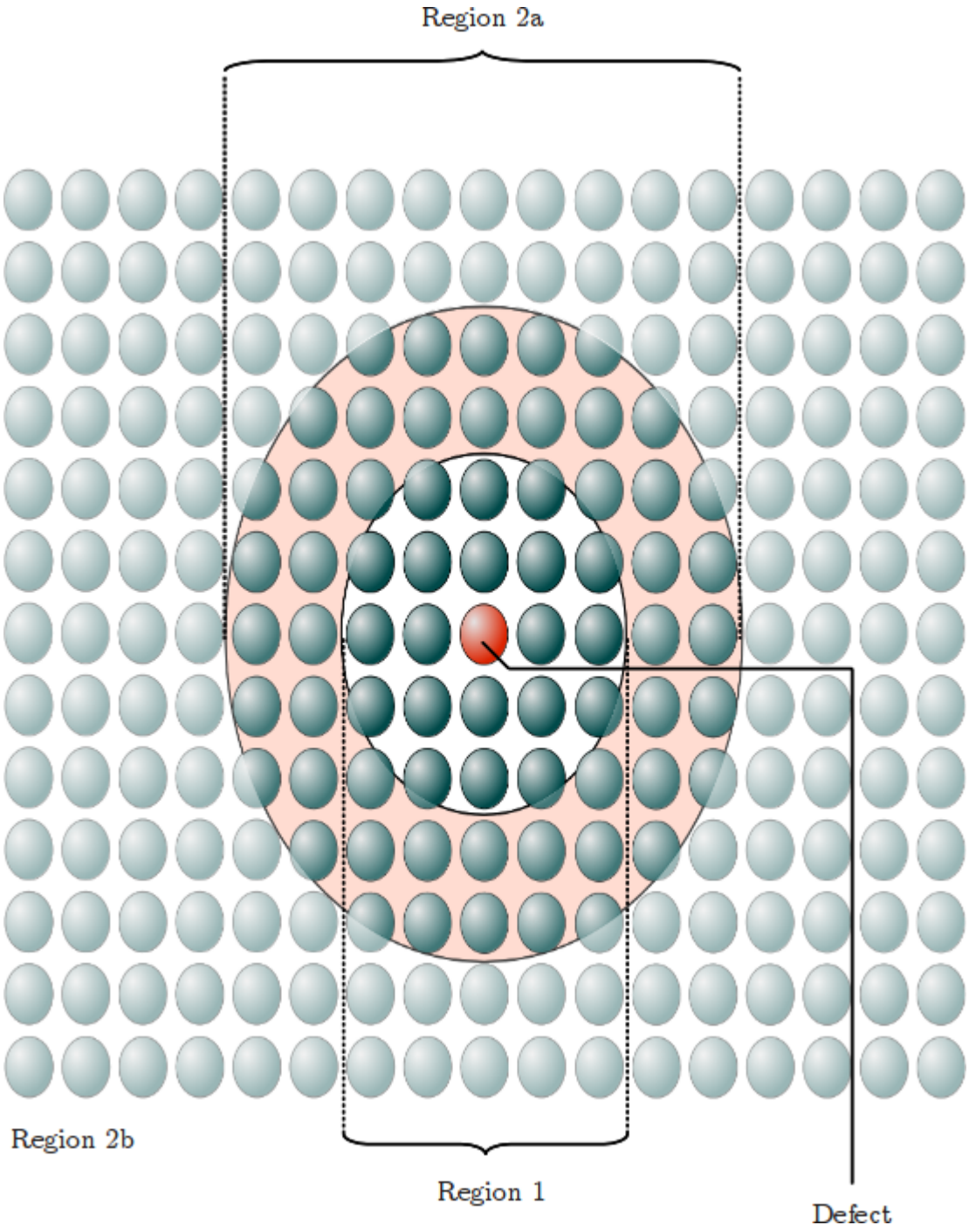

Figure 2.4: Schematic representation of the Mott-Littleton approach showing a defect ion (red) as part of a larger lattice (blue). The regions centred on the defect are subject to varying levels of approximation based on the distance from the defect

breakthrough in the development of DFT[79], with Kohn and Sham later providing a framework with which to solve DFT problems practically [80].

The Schroedinger equation [81], developed by Erwin Schroedinger in 1926, is vitally important in quantum mechanics and electronic structure techniques. In principle it allows all properties of a physical system to be calculated, given the wavefunction of the system. The wavefunction contains all the information about the positions and spins of the bodies that comprise the system. The time-independent Schroedinger equation (Equation 2.19) appears simple, however generating a solution is extremely complex.

$$\mathscr{H}\Psi = E_{Total}\Psi \tag{2.19}$$

Here $\mathscr{H}$ is the full Hamiltonian operator, a set of mathematical operations which when performed on the wavefunction returns a value describing a property of the system, in this case the total energy. Ψ represents the many-body wave function, which as already stated contains all the information (position, spin etc.) about the bodies it describes. Finally E_{Total} is the total energy of the system in question. $\mathscr{H}$, the full Hamiltonian can be described by;

$$\mathscr{H} = T + T_n + V_{int} + V_{nn} + V_{ext} \tag{2.20}$$

$$\begin{aligned}\mathscr{H} = -\frac{h^2}{2m_e}\sum_i \nabla_i^2 - \sum_I \frac{h^2}{2M_I}\nabla_I^2 + \frac{1}{2}\sum_{i\neq j}\frac{e^2}{|\mathbf{r}_i - \mathbf{r}_j|} \\ + \frac{1}{2}\sum_{I\neq J}\frac{Z_I Z_J \cdot e^2}{|\mathbf{R}_I - \mathbf{R}_J|} - \sum_{i,I}\frac{Z_I \cdot e}{|\mathbf{r}_i - \mathbf{R}_I|}\end{aligned} \tag{2.21}$$

Here m_e and $\mathbf{r}_i$ represent the mass and position of electron i and M_I and $\mathbf{R}_I$ the mass and position of nucleus I, with a charge of Z_I. The first two terms of Equation 2.20, T and T_n are the kinetic energy of the electrons and nuclei respectively. The final three terms, V_{int}, V_{nn} and V_{ext} correspond to the potential energy, with V_{int} representing the electron-electron repulsions, V_{nn} the nuclear-nuclear repulsions and V_{ext}, the external potential, as seen by the electrons, equivalent to the electron-nuclear attraction. Note that the factor of $\frac{1}{4\pi\epsilon_0}$ has been omitted for simplicity and that the summations extend over all the system's electrons and nuclei.

We can see that evaluation of the full Hamiltonian will be complex and onerous for many-body systems due to the large number of interdependencies which must be considered. To perform electronic structure calculations in practice many approximations will need to be employed to simplify the problem so that it is manageable. The first of these is the Born-Oppenheimer approximation, which decouples the

nuclear and electron motions so that the electrons move about a fixed nuclear configuration. This is justified by the fact that the nuclear masses are far in excess of the mass of an electron. Therefore the speed at which a nucleus moves will be negligible compared to the speed of an electron. Having applied the Born-Oppenheimer approximation we are able to rewrite equations 2.20 and 2.21 in terms of $\mathscr{H}_{elec}$, the electronic Hamiltonian.

$$\mathscr{H}_{elec} = T + V_{int} + V_{ext} \tag{2.22}$$

$$\mathscr{H}_{elec} = -\frac{h^2}{2m_e}\sum_i \nabla_i^2 + \frac{1}{2}\sum_{i\neq j}\frac{e^2}{|\mathbf{r}_i - \mathbf{r}_j|} - \sum_{i,I}\frac{Z_I \cdot e}{|\mathbf{r}_i - \mathbf{R}_I|} \tag{2.23}$$

$$\mathscr{H}_{elec} = -\frac{h^2}{2m_e}\sum_i \nabla_i^2 + \frac{1}{2}\sum_{i\neq j}\frac{e^2}{|\mathbf{r}_i - \mathbf{r}_j|} + \sum_i V_{ext}(\mathbf{r}_i) \tag{2.24}$$

By simplifying $\mathscr{H}$ to $\mathscr{H}_{elec}$ with the Born-Oppenheimer approximation we have reduced the complexity of the problem as the many-body wave function, Ψ is now only dependent on the spins and positions of the systems electrons, with the nuclear positions only entering as a component of the external potential V_{ext}.

Hartree-Fock based techniques attempt to solve the Schroedinger equation by calculating Ψ, the many-body wavefunction. This is done by combining the individual wavefunctions within the system.

Density functional theory treats the problem differently to Hartree-Fock as it does not calculate the many-electron wavefunction. Instead it calculates the ground-state electron density of the system. This can then be used to find the ground-state energy and other properties. The validity of this approach was proved by Hohenberg and Kohn's seminal paper [79] that proved two theorems:

> **Theorem 1:** The ground-state properties of many electron systems are determined uniquely by the three dimensional electron density of the system.
>
> **Theorem 2:** A system's energy can be defined as a functional of the electron density and that the correct ground-state electron density corresponds to the minimum of the energy functional.

So rather than calculating the many-body wavefunction, if the energy functional for the system can be defined and the minimum found, the ground-state electron density of the system is accessible, from which the ground-state properties of the system can be derived.

In their landmark paper Hohenberg and Kohn [79] described the form of the energy functional as

$$E[\rho(\mathbf{r})] = \int V_{ext}(\mathbf{r})\rho(\mathbf{r})d(\mathbf{r}) + F[\rho(\mathbf{r})] \tag{2.25}$$

The first term, V_{ext}, describes the interaction of electrons with the external potential. As the Born-Oppenheimer approximation has been utilised, the interactions between a system's electrons and nuclei are also described within V_{ext}. $\rho(\mathbf{r})$ represents the three dimensional electron density and finally the $F[\rho(\mathbf{r})]$ term describes the summation of the inter-electron interactions and the electron's kinetic energy. While it appears we have everything we need to calculate the ground-state energy of our system this is not the case as the nature of $F[\rho(\mathbf{r})]$ is unknown and so exact solutions are unavailable.

The Kohn and Sham Approach

In the second pivotal paper in the development of DFT[80], Kohn and Sham introduced a method of practically solving DFT problems. Their approach was to assume that for any given system comprised of a set of interacting electrons with an electron density $\rho(\mathbf{r})$, an equivalent theoretical system of non-interacting electrons could be created with the same $\rho(\mathbf{r})$. This assumption allowed them to separate the unknown term of the Hohenberg-Kohn energy functional into components;

$$F[\rho(\mathbf{r})] = E_{ke}[\rho(\mathbf{r})] + E_H[\rho(r)] + E_{xc}[\rho(\mathbf{r})] \tag{2.26}$$

Within the Kohn-Sham approximation the $E_{ke}[\rho(\mathbf{r})]$ represents kinetic energy of the electrons. $E_H[\rho(\mathbf{r})]$ is the Hartree term which represents the electron-electron Coulombic energy. The final $E_{xc}[\rho(\mathbf{r})]$ term is the exchange-correlation term, which is key and approximations to represent it are discussed later. It contains contributions from the exchange and correlation of electrons in the interacting system as expected but it is also used to describe the difference in energy between the real interacting system and the hypothetical non-interacting system. The exchange-correlation term effectively collects all the unknowns of the problem into a single term which needs to be approximated.

When referring to Equation 2.26 it is important to recall that $E_{ke}[\rho(\mathbf{r})]$ actually represents the energy of a set of non-interacting electrons which have the same density $\rho(\mathbf{r})$ as the electrons of the modelled system. Also remember that the Hartree term (Equation 2.27) fails to recognise that electron motions are correlated and defines the electron interactions as the summation of classical pairwise interactions between charge densities.

$$E_H(\rho(\mathbf{r})] = \frac{1}{2}\int\int \frac{\rho(\mathbf{r}_1)\rho(\mathbf{r}_2)}{[r_1 - r_2]} d\mathbf{r}_1 d\mathbf{r}_2 \tag{2.27}$$

Combining Equations 2.25 and 2.26 and then minimising with respect to $\rho(\mathbf{r})$, in order to give a stationary solution results in the Schroedinger-like Kohn-Sham equation:

$$\left[-\frac{h^2}{2m_e}\nabla^2 + V_{eff}(\mathbf{r})\right]\psi_i(\mathbf{r}) = \epsilon_i\psi_i(r) \tag{2.28}$$

Here ϵ_i are the orbital energies, and $\psi_i(\mathbf{r})$ represents the Kohn-Sham orbitals containing the non-interacting electrons. Finally V_{eff} is the effective potential for the system, which is given by:

$$V_{eff}(\mathbf{r}) = V_{ext}(\mathbf{r}) + \int \frac{\rho(\mathbf{r}')}{|\mathbf{r} - \mathbf{r}'|}d\mathbf{r}' + V_{xc}(\mathbf{r}) \tag{2.29}$$

$V_{xc}(\mathbf{r})$, the exchange-correlation potential, is related to $E_{xc}[\rho(\mathbf{r})]$ the exchange-correlation energy functional by;

$$V_{xc}(\mathbf{r}) = \left(\frac{\delta E_{xc}[\rho(\mathbf{r})]}{\delta\rho(\mathbf{r})}\right) \tag{2.30}$$

In a hypothetical DFT calculation an initial guess of the electron density, $\rho(\mathbf{r})$, is made. This is used to generate an effective potential in conjunction with Equation 2.29. This effective potential is then used in Equation 2.28 to generate a set of Kohn-Sham orbitals for the system. These orbitals are then used to calculate an improved estimate of the electron density using.

$$\rho(\mathbf{r}) = \sum_{i}^{N} |\psi_i(\mathbf{r}_i)|^2 \tag{2.31}$$

This cycle is then repeated using the improved estimate of $\rho(\mathbf{r})$ until convergence is reached. This procedure is referred to as the self-consistent field method. This converged electron density corresponds to the correct ground-state electron density for the system according to the second Hohenberg-Kohn theorem[79] (refer to Section 2.6.1).

Approximations for the Exchange-Correlation Functional

One of DFT's major failings is that the exact nature of the exchange-correlation energy term, $E_{xc}[\rho(\mathbf{r})]$, is unknown for the vast majority of systems. It has been calculated for a homogeneous electron gas. In this case the exchange energy is known exactly and the correlation energy has been calculated using Monte Carlo methods to a high precision. However for almost all other systems the nature of $E_{xc}[\rho(\mathbf{r})]$ is not known, and therefore it is necessary to approximate it. This approximation is generally considered to be a significant source of error in DFT calculations. That said it is possible to gain good results using simple approximations for $E_{xc}[\rho(\mathbf{r})]$, despite the fact that the true nature of $E_{xc}[\rho(\mathbf{r})]$ is assumed to be extremely complex.

The simplest approximation for the exchange-correlation term is the Local Density Approximation (LDA). First suggested by Kohn and Sham the LDA has proved popular. The exchange-correlation functional for the LDA takes the form;

$$E_{xc}^{LDA}[\rho] = \int \rho(\mathbf{r})\varepsilon_{xc}^{hom}(\rho(\mathbf{r}))d\mathbf{r} \tag{2.32}$$

The LDA assumes that the exchange-correlation energy per electron, which is located at point $\mathbf{r}$, can be equated to that of the homogeneous electron gas with density $\rho(\mathbf{r})$. In general the LDA predicts certain material properties accurately. For example; crystal structures, phonon frequencies and bond lengths are usually reproduced well. This is true even for systems where the electron density does not resemble the homogeneous electron gas, for such inhomogeneous systems one might expect the LDA to be invalid. The LDA's success is partially due to the fact that some of its errors are systematically cancelled; the LDA consistently over estimates the exchange energy and under estimates the correlation energy. Despite the serendipitous error cancellation several problems with the LDA remain. A crucial failure with respect to this work is that LDA consistently under estimates a material's band gap, however other notable problems include the fact that systems modelled with the LDA over-bind, as the LDA over estimates the cohesive energy of systems.

Real systems always contain some variations in electron density with respect to position, and so the idea of a homogeneous electron gas is somewhat flawed. There are approximations for the exchange-correlation that attempt to acknowledge this phenomenon. These semi-local functionals consider the local electron density at point $\mathbf{r}$, however unlike the LDA these functionals also consider the variations of $\rho(\mathbf{r})$, consequently these functionals are referred to as gradient-correlated. The simplest gradient-correlated functional is the "Generalised Gradient Approximation" (GGA) functional, which takes the form;

$$E_{xc}^{GGA}[\rho] = \int \rho(\mathbf{r})\varepsilon_{xc}^{GGA}\left(\rho(\mathbf{r}), \nabla\rho(\mathbf{r})\right) d\mathbf{r} \tag{2.33}$$

Unlike LDA, which only exists in one form as there is only one principally correct form of ε_{xc}, for GGA there are multiple valid parametrisations of ε_{xc}. As a consequence several forms of the GGA exist, and in this work the Perdew, Burke and Ernzerhof (PBE) [82] functional has been used. However there are alternatives available such as those of Perdew and Wang (PW91)[83] and Wang and Cohen (WC)[84].

Generally for non-metallic systems such as inorganic oxides and sulphides, calculations that utilise a GGA functional yield more accurate descriptions of the real system's key properties, such as lattice parameters, than equivalent calculations using an LDA approach. The over-binding in LDA is corrected for and band gaps are reproduced more accurately, though the error is still significant and a problem as is discussed in section 2.6.3.

2.6.2 Applying DFT to Solids

Solving the Schroedinger equation in order to calculate material properties is confounded by several problems when dealing with solid state systems. As we generally think of a given solid as having an infinite number of ions and electrons we would need to determine the wavefunction of this infinite number of electrons. Furthermore as the wavefunction of each electron extends over the entire lattice, to describe it would require an infinite number of basis functions. Fortunately the periodic nature of solids means that symmetry obviates the need to consider these infinite quantities and therefore the problem becomes tractable.

K-space - The Reciprocal Lattice

We are accustomed to thinking of a crystal lattice defined in real space, however the implementation of computational techniques can require the crystal lattice to be defined in reciprocal space or **k**-space. A reciprocal lattice is therefore simply a representation of the crystal lattice defined in **k**-space, where the real space lattice vectors **a**, **b** and **c** are related to the **k**-space lattice vectors $\mathbf{a}^*$, $\mathbf{b}^*$ and $\mathbf{c}^*$ by the following relationship:

$$\mathbf{a}^* = 2\pi\frac{\mathbf{b}\times\mathbf{c}}{\mathbf{a}\cdot\mathbf{b}\times\mathbf{c}}\ ;\ \mathbf{b}^* = 2\pi\frac{\mathbf{a}\times\mathbf{c}}{\mathbf{b}\cdot\mathbf{c}\times\mathbf{a}}\ ;\ \mathbf{c}^* = 2\pi\frac{\mathbf{a}\times\mathbf{b}}{\mathbf{c}\cdot\mathbf{a}\times\mathbf{b}} \tag{2.34}$$

In the same way that it is possible to build up an infinite real space crystal lattice by defining a unit cell, we can define a primitive cell in **k**-space which reproduces the infinite reciprocal lattice. This **k**-space primitive cell is known as the Brillouin Zone. It is critical as the system's wavefunction can be completely described within this small section of the system's volume.

Bloch's Theorem

Bloch's theorem[85] states that for an electron i in a periodic field the wavefunction can be broken down into two components, one giving the periodic nature of the primitive cell and the other being wave-like. The wave-like component is described by;

$$\Psi_i(\mathbf{r}) = e^{i\mathbf{k}\cdot\mathbf{r}} f_i(\mathbf{r}) \tag{2.35}$$

Where **k** is the wavevector in the Brillouin Zone and this determines the directionality and frequency of this wave-like component.

The periodic component of the wavefunction can be generated by combining a set of discrete planewaves $e^{i\mathbf{G}\cdot\mathbf{r}}$. The wavevectors $\mathbf{G}$ represent all possible translations to symmetrically identical lattice points.

$$f_i(\mathbf{r}) = \sum_{\mathbf{G}} c_{i,\mathbf{G}} e^{i\mathbf{G}\cdot\mathbf{r}} \tag{2.36}$$

The electron i's wavefunction can be evaluated as the summation of planewaves;

$$\Psi_i(\mathbf{r}) = \sum_{\mathbf{G}} c_{i,\mathbf{k}+\mathbf{G}} e^{i(\mathbf{k}+\mathbf{G})\cdot\mathbf{r}} \tag{2.37}$$

Planewaves

When using a planewave basis set there are two approximations which can be made that help to reduce the complexity of a proposed simulation. Firstly, as planewaves with a larger $|\mathbf{G}|$ contribute less to the wavefunction, as their kinetic energy is larger. We can define an energy cut-off, above which the planewaves are not evaluated as their contribution to the wavefunction is deemed to be insignificant. The second approximation relates to the sampling of $\mathbf{k}$-space. As Ψ is a continuous function of $\mathbf{k}$ small changes in $\mathbf{k}$ will have only a limited effect on Ψ. Therefore rather than sampling an infinite number of points which completely describe $\mathbf{k}$-space we can define a finite set of $\mathbf{k}$-points which give an adequate description of $\mathbf{k}$-space.

The choice of an appropriate set of $\mathbf{k}$-points is vital to correctly describing the density of states and band structure of a material. The Monkhorst-Pack approach[86] defines an equally spaced mesh of $\mathbf{k}$-points to sample the Brillouin Zone. This method has the advantage that some of the $\mathbf{k}$-points in the mesh are related to one another by symmetry. Therefore we need only calculate the wavefunction at the symmetry-inequivalent $\mathbf{k}$-points and hence avoid excess computational expense.

In practical terms, both of the above approximations require convergence testing. While we cannot converge the wavefunction it is possible to converge the material properties which are of interest. A range of calculations with varying values for the energy cut-off and densities of the $\mathbf{k}$-mesh must be performed and the convergence of the property of interest must be evaluated. Not all properties require the same level of accuracy, some properties such as a system's total energy converge reasonably quickly and so it can be acceptable to use lower cut-offs and coarser $\mathbf{k}$-meshes, provided this is the sole property of interest. However other properties such as the position of a given energy level require higher accuracy calculations to achieve convergence.

Pseudopotentials

In the space immediately surrounding an atom/ion's nucleus the potential and consequently the wavefunction of an associated electron varies dramatically. Were we to attempt to describe the wavefunction at such small distances from the nucleus a very large number of planewaves would be required, and obviously this would introduce an associated computational cost. As the nature of the core electrons in a system varies little in different chemical environments a common approximation is to remove the core electrons from a system and to represent the potential around the nucleus with a smooth function which can be reproduced with a reduced set of planewaves. For this to be appropriate the function representing the potential around the nucleus, known as the pseudopotential, must have the same form as the original potential outside a certain cut-off radius from the nuclei. We are now only representing the valence region of our system adequately and so any consideration of the core electrons is no longer possible.

Pseudopotentials have a property known as "softness", this describes how smooth the pseudopotential function is and how large a cut-off radius has been used. Pseudopotentials which are very smooth necessitate fewer basis functions to describe them but a pseudopotential should not be too soft as larger cut-off radii reduce the accuracy and make a pseudopotential less transferable. Good pseudopotentials are those which best reproduce the valence properties of the ion in question. Generally pseudopotentials which do this most effectively are those calculated with *ab initio* methods rather than those generated empirically.

The Projector Augmented Wave (PAW) method[85] uses an extremely smooth pseudopotential in conjunction with additional local functions to describe the all-electron wavefunction.

2.6.3 Hybrid Functionals

It has already been noted that both approximations to the exchange-correlation term discussed so far LDA and GGA significantly underestimate the band gap of semiconducting materials. This work is primarily concerned with the emerging sulphide based semiconductors that have potential photovoltaic applications. Clearly in this work an accurate description of the band gap will be key.

Why Semi-local Functionals Fail to Describe Semiconductor Band Gaps

The failure of the LDA and GGA is rationalised with reference to the Self Interaction Energy (SIE)[87, 88]. A given electron in the simulated system feels an electrostatic potential resulting from the presence of all the other electrons. However in the semi-local LDA and GGA approximations this electrostatic potential contains contributions from all the electrons in the system, including the electron we are considering.

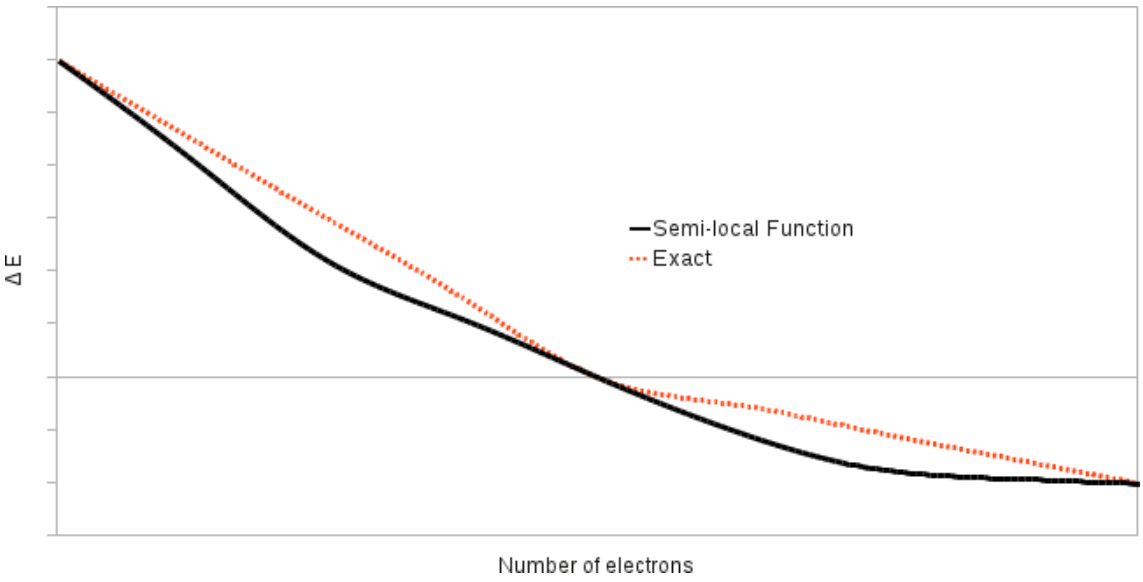

Figure 2.5: Schematic illustrating the de-localisation error's effect on the description of the energy of systems with partial charges when utilising semi-local functionals. Created based on reference[88].

Therefore the electron feels the effect of its own electrostatic potential, in effect interacting with itself. The self interaction in semi-local approaches causes electronic de-localisation to be exacerbated, this is referred to as the de-localisation error. It is important as when electrons are added to or removed from a system the semi-local methods predict an overly disperse distribution for the resultant electron/hole[88].

This is demonstrated if we consider a system with a varying number of electrons. We can plot a fractional-electron-energy-function, the energy of the system as a function of the number of electrons. In real systems this function is linear between the points defined by integer numbers of electrons as electrons are discrete entities. However when we plot the fractional-electron-energy-function predicted by semi-local functionals against a real reference function (shown schematically in Figure 2.5) we can see that while the semi-local methods accurately describe the systems energy at integer number of electrons the description of systems with partial charges is inaccurate. The predicted energy for these partially charged systems is too low.

This is important as the system's ionisation energy and electron affinity are derivatives of this fractional-electron-energy-function and consequently the error is passed on to these quantities. In turn this affects the semi-local functionals ability to predict a system's band gap which is formally defined in terms of these quantities. $\Delta E_g = E_{(N+1)} + E_{(N-1)} - 2E_N$, where E_N is the energy of the N electron system.

While semi-local functions underestimate the energy of partially charged systems Hartree-Fock based methods do not suffer from the self interaction error. How-

ever Hartree-Fock based techniques tend towards overestimation of the energy. The Hartree-Fock term can be seen as a Coulombic term, which localises the electron density as opposed to the density-functional theory that delocalises the electron distribution. The combination of density-functional theory and Hartree-Fock based methods leads to a better description of the band-gaps of medium gap semiconductors.

Forms of Hybrid Functional

There are several ways in which the semi-local and Hartree-Fock based methods can be combined and this leads to a number of distinct hybrid functionals.

The development of hybrid functionals began with empirical mixing of the LDA and Hartree-Fock[89], this progressed to a scheme in which the LDA, GGA and Hartree-Fock were combined to give the hybrid functional known as B3LYP[90–92]. Subsequently Perdew, Burke and Ernzerhof have developed an alternative hybrid functional called PBE0. Which takes the form:

$$E_{xc}^{PBE0} = aE_x^{HF} + (1-a)E_x^{PBE} + E_c^{PBE} \tag{2.38}$$

Where the mixing coefficient $a = \frac{1}{4}$ is derived from perturbation theory[92]. This approach is useful for molecular simulations; however, in condensed matter, charge screening effects are significant which limits the applicability of PBE0.

An alternative implementation of the hybrid functional concept, based on that of PBE0, has been devised by Heyd, Scuseria, and Ernzerhof (HSE)[93]. Here the PBE0 exchange energy defined by:

$$E_x^{PBE0} = aE_x^{HF} + (1-a)E_x^{PBE} \tag{2.39}$$

is separated into two components, one long range and one short range component:

$$\begin{aligned} E_x^{PBE0} = aE_x^{HR,SR}(\omega) + E_x^{HF,LR}(\omega) + (1-a)E_x^{PBE,SR}(\omega) \\ + E_x^{PBE,LR}(\omega) - aE_x^{PBE,LR}(\omega) \end{aligned} \tag{2.40}$$

Here ω is the distance cut-off that defines the extent of the short range interactions. The long range terms given from the Hartree-Fock and PBE components, $+aE_x^{HF,LR}(\omega)$ and $-aE_x^{PBE,LR}(\omega)$ have very similar magnitudes and as their signs are opposed they are omitted from the full functional for simplicity. The full functional is then described by;

$$E_{xc}^{\omega PBEh} = aE_x^{HF,SR}(\omega) + (1-a)E_x^{PBE,SR}(\omega) + E_x^{PBE,LR}(\omega) + E_c^{PBE} \qquad (2.41)$$

For the limiting cases of ω the ωPBE hybrid functional returns the results of PBE0 ($\omega = 0$) and asymptotically approaches that of PBE as $\omega \to \infty$[93]. The approach is justified in condensed matter systems as the screening of the Coulomb potential limits the range of the exchange potential. In this work a screening parameter of $\omega = 0.207\text{Å}^{-1}$ has been used. When this screening parameter is used it is common to refer to the functional as HSE06[94]. This functional is considered superior to the original implementation (HSE03) where errors in implementation lead to a smaller value of ω being utilised. The band gaps predicted by the two functionals have been shown to be similar but HSE06 describes ionisation energies and electron affinities more accurately[94].

Photovoltaics integrated into skyscraper

Chapter 3

Structural and electronic properties of $CuSbS_2$ and $CuBiS_2$

3.1 Introduction

New thin-film solar cell materials and a greater understanding of their properties are needed to meet the urgent demand for sustainable, lower-cost and scalable photovoltaics (PV). The CdTe and $CuIn_{1-x}Ga_xSe_yS_{2-y}$ (CIGS) absorber systems have been developed for thin-film PV devices, but may be limited in the long-term by the scarcity of Te, Ga, and In[7, 13, 95–97]. There is therefore an increasing need to expand the range of absorber materials that are available as viable alternatives to the toxic Cd in CdTe and the relatively expensive CIGS based systems. One of the main advantages of these inorganic thin-film materials over silicon is that they absorb light more strongly because the optical transition is spatially direct rather than requiring simultaneous absorption or emission of photons[7].

Recently, Cu_2ZnSnS_4 (CZTS) has attracted considerable interest as a promising absorber material with suitable optical properties (near-optimum direct band-gap energy of 1.5 eV; large absorption coefficient of 10^4 cm^{-1}), as well as containing earth-abundant elements [45, 46, 98]. However, there are challenges with the CZTS system related to structural polymorphism and control of the precise cation stoichiometry.

Alternative ternary copper sulfides based on Cu-Bi-S or Cu-Sb-S type materials [31–40] such as $CuBiS_2$ and $CuSbS_2$ show promising properties as absorber materials for thin-film solar cells, as well as containing abundant and non-toxic elements. An early study of Rodriguez-Lazcano *et al.*[40] reported a method to produce $CuSbS_2$ thin films through a solid state reaction involving thin films of Sb_2S_3 and CuS. Rabhi *et al.*[39] have studied the structural, optical and electrical properties of $CuSbS_2$ thin films grown by thermal evaporation and have related the effects of substrate heating conditions on these properties. Manolache *et al.*[34] have examined the influence of

precursor concentration on the morphology and the structure of $CuSbS_2$ thin films obtained from aqueous solutions. However, in the case of ce CuBiS2 and $CuSbS_2$, their fundamental properties and performance have not been fully characterized. Indeed, it is clear that the underlying bulk and electronic structure of ternary copper sulfide materials are complex, but are crucial to the greater understanding of their structure-property relationships and PV behavior.

The present study uses first-principles Density Functional Theory (DFT) techniques to investigate key issues related to bulk structure, band gaps and local electronic structure of lone pairs in the $CuBiS_2$ and $CuSbS_2$ materials, with reference to experimental results where possible. This work extends analogous computational studies of other thin film PV materials[99–102] including CZTS [103, 104], and provides a solid platform for further experimental characterisation.

3.2 Chapter Methodology

Density Functional Theory (DFT) calculations were performed utilizing the plane-wave Projector Augmented-Wave (PAW) method [85, 105] using the Vienna *Ab initio* Simulation Package (VASP)[106, 107]. For the exchange-correlation functional, the Generalized Gradient Approximation (GGA) of Perdew-Burke-Ernzerhof (PBE)[82] was used along with the Heyd-Scuseria-Ernzerhof (HSE06)[93] hybrid-functional where exact Hartree-Fock exchange replaces 25% of the exchange potential of the PBE functional. For studies of photoactive materials where the band gap is a critical material property, it is important that there is an accurate description of the band gap and the states at the band edges. The use of hybrid functionals is found to be important as standard GGA functionals significantly underestimate the band gap of a wide range of semiconducting materials[99, 104]. It should be noted that calculations were also performed with the PBE0[92] hybrid functional. However we found that the screened exchange provided by the HSE06 functional gave the most accurate reproduction of experimental band gap values, whereas PBE0 tended towards overestimation. We should also note that recent GGA-PBE calculations[108] reported a small band gap of 0.5 eV for $CuBiS_2$, although the focus of this study was the thermoelectric performance at ambient temperature of the hole-doped system. However other properties such as the nature of the DOS, charge density distributions, etc., are largely unchanged between the two hybrid functionals.

Structural and electronic properties have been determined by modelling the 16-atom crystallographic unit cell. For total energy calculations, a plane-wave energy cut-off of 300 eV has been used throughout. The infinite solid is modelled using standard periodic boundary conditions in three dimensions. For sampling of the Brillouin zone, a $4 \times 6 \times 2$ Monkhorst-Pack[86] k-point mesh has been used, which offered good convergence in the calculated structural and thermodynamic properties. All lattice parameters and ionic positions were fully relaxed by minimising the forces and total energy of the system. A residual atomic force tolerance of $< 1 \times 10^{-4}$

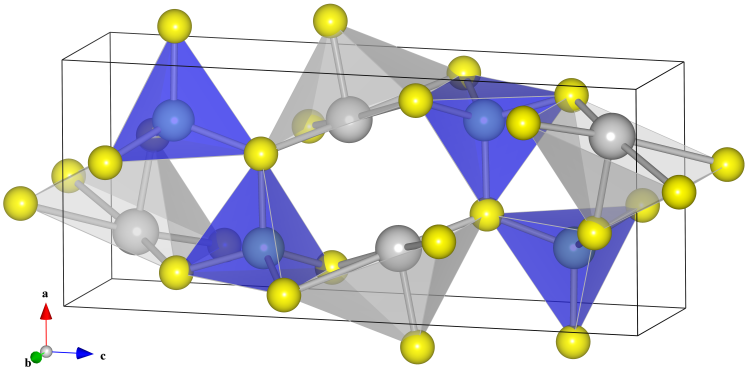

(a) $CuSbS_2$

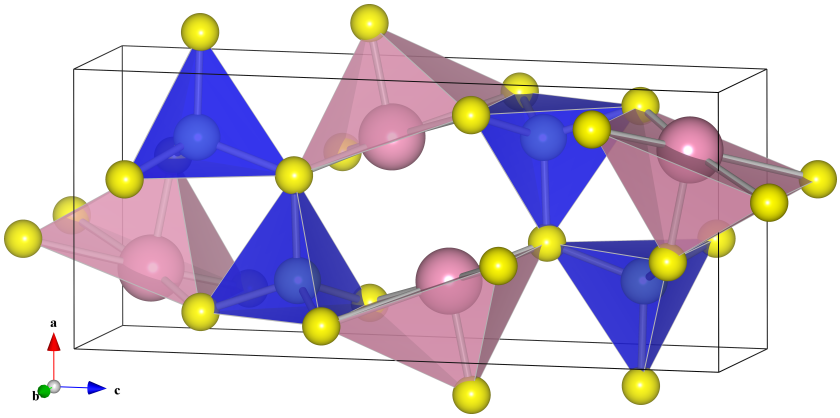

(b) $CuBiS_2$

Figure 3.1: Structure of $CuSbS_2$ and $CuBiS_2$ showing CuS_4 tetrahedra (blue), SbS_5/BiS_5 square pyramidal units (grey)/(pink) respectively and S atoms (yellow).

eV $Å^{-1}$ was used, a stringent convergence criterion. Similar DFT methods have been successfully applied to copper-sulphide type compounds[103, 104], and other energy-related materials[68, 109, 110].

3.3 Crystal Structures and Band Gaps

$CuSbS_2$ (chalcostibite) and $CuBiS_2$ (emplectite) are isostructural (orthorhombic space group *Pnma*). The structures (shown in Figure 1.5 and 3.1) are composed of square pyramidal MS_5 units (M = Sb/Bi) which edge share to form continuous MS_2 units aligned with the *b* axis. These continuous units are separated by CuS_4 tetrahedra so that the base of the square pyramidal units are aligned to face one another, thus directing the Sb/Bi lone pair electron density into the void separating the MS_5 units.

Table 3.1: Comparison of calculated $CuSbS_2$ lattice parameters and band gaps with experiment

		PBE		HSE06	
Parameter	Expt	Calc	Δ (Calc-Expt)	Calc	Δ (Calc-Expt)
a (Å)	6.016 *	6.137	0.121	6.055	-0.039
b (Å)	3.797 *	3.834	0.038	3.807	-0.010
c (Å)	14.499*	14.480	-0.019	14.523	0.024
$\alpha = \beta = \gamma$ (deg)	90.0*	90.0	0	90.0	0
E_g (eV)	1.38 * ; 1.52 †	0.90	-	1.69	-

* Zhou *et al.*[37], † Rodriguez *et al.*[40]

Table 3.2: Comparison of calculated $CuBiS_2$ lattice parameters and band gaps with experiment

		PBE		HSE06	
Parameter	Expt	Calc	Δ (Calc-Expt)	Calc	Δ (Calc-Expt)
a (Å)	6.134 ‡	6.263	0.129	6.178	0.044
b (Å)	3.911 ‡	3.949	0.038	3.924	0.012
c (Å)	14.549 ‡	14.498	-0.051	14.568	-0.019
$\alpha = \beta = \gamma$ (deg)	90.0‡	90.0	0.0	90.0	0.0
E_g (eV)	1.65 § ; 1.8 ¶	0.36	-	1.55	-

‡ Kyono *et al.*[111], § Pawar *et al.*[112], ¶ Sonawane *et al.*[113]

In order to assess the accuracy of our computational approach, structural optimisations of $CuSbS_2$ and $CuBiS_2$ were performed based on the experimental bulk crystal structures and using both PBE and the HSE06 hybrid functional. In Tables 3.1 and 3.2 we compare our calculated lattice parameters and band gaps to experimental studies. We find that standard DFT utilizing the PBE functional describes the lattice parameters adequately for both $CuSbS_2$ and $CuBiS_2$. There is a slight overestimation of the a lattice parameter ($\approx 2\%$) in both systems, which is likely to be due to an under-estimation of the lone pair - lone pair interactions (i.e. the lack of dynamic correlation). However more importantly we find that, as is the case for other chalcogenide systems, the band gap is severely underestimated using a GGA functional[99, 103].

The use of the HSE06 hybrid functional improves the reproduction of lattice parameters and we no longer observe a slight over estimation of the a lattice parameter for either system. But crucially the use of this hybrid functional improves the reproduction of the band gaps dramatically, as found in DFT studies of CZTS[104]. As noted, an accurate description of the band gap is crucial in designing new PV materials with improved absorption properties. Several experimental band gaps for $CuSbS_2$ have been published; and we have included the values published by Zhou *et al.*[37] and Rodriguez-Lazcano *et al.*[40] in Table 3.1. Of the published experimental values our results support the value of 1.52 eV of Rodriguez-Lazcano *et al.*. This also accords with an approximate band gap energy of 1.5 eV from recent studies of $CuSbS_2$ thin films formed via chalcogenisation of Sb-Cu metal precursors[114].

For $CuBiS_2$, the calculated band gap of 1.55 eV (using HSE06) is in good accord with the experimental value of 1.65 eV [112], and falls in the range for a viable absorber material. The differences between experimental values could be due to variations in sample quality or incorrect linear interpolation in deriving the band gap energy. Clearly synthetic conditions and the presence/absence of secondary phases must affect the band gap measured by experimental groups significantly. For both $CuSbS_2$ and $CuBiS_2$ the fundamental band gaps are predicted to be indirect in nature; however, the difference between the lowest energy direct and indirect gaps is only of the order of 0.1 eV, so that a strong onset of optical absorption is still expected. This is distinct from the case of Si, where the difference is larger than 2 eV, which limits the absorption of visible light in thin films.

3.4 Thermodynamic Stability

Evaluation of the phase stability of new PV compounds is of great importance for the design of effective synthetic routes. Issues such as elemental losses during thermal treatments [114, 115], as well as compatibility of components at the interfaces [116], are currently faced in various fields of materials science and technology. A recent study[117] has stressed the significance of thermochemistry in the understanding and prediction of the chemical equilibria of PV materials. Hence, knowledge of the ther-

modynamic functions of new materials for device application is crucial. Currently no sound experimental measurement is available for either $CuSbS_2$ or $CuBiS_2$. In these circumstances, computation is a viable option for the provision of such data. We have therefore calculated the enthalpy of formation for each compound with respect to its elemental standard. The total energy change for the reactions

$$Cu(s) + Sb(s) + 2S(s) \rightarrow CuSbS_2 \tag{3.1}$$

and

$$Cu(s) + Bi(s) + 2S(s) \rightarrow CuBiS_2 \tag{3.2}$$

is -1.08 eV and -1.16 eV, respectively at the level of HSE06. This suggests that the materials are thermodynamically stable, and the values are comparable to other metal sulphide materials[118]. Further studies are required to estimate the complete chemical potentials and their temperature dependence, for direct applications in thermochemical studies.

3.5 Density of States (DOS)

Figure 3.2 shows the orbital-projected density of states (DOS) for $CuSbS_2$ and $CuBiS_2$. It is clear that the electronic structure of the two materials is very similar. We see prominent peaks corresponding to the S-*3s* states from -18 to -14 eV. Peaks comprised mainly of Sb-*5s*/Bi-*6s* states, with this peak in $CuSbS_2$ from -11.5 to -9.5 eV and in $CuBiS_2$ from -13 to -10 eV, this peak off-set being the most notable difference between the density of states of the two materials. We then observe a series of intense peaks which make up the valence band; as is the case for many other chalcogenide PV materials e.g. CZTS, $CuInS_2$, $CuGaS_2$, $CuInSe_2$, the top of the valence band is dominated by Cu-*3d* states[103, 104, 119]. This is clearly illustrated in Figure 3.3 which shows the calculated charge density for the valence and conduction bands of $CuSbS_2$ and $CuBiS_2$. We also find that the conduction bands are comprised of hybridized (Sb-*5s*/S-*3p*) / (Bi-*6s*/S-*3p*) states, analogous to the (Sn-*5s*/S-*3p*) states seen in CZTS.

As Cu in $CuSbS_2$ and $CuBiS_2$ exists as Cu^+ (d^{10}) the Cu-*3d* states of the valence band are fully occupied and we do not find Cu states in the conduction band. Figure 3.2 shows that the top of the valence band is comprised mostly of Cu-*3d* states. Therefore upon photoexcitation the promotion of a Cu based electron will result in the oxidation of Cu^+ (d^{10}) to Cu^{2+} (d^9). This may have implications for hole transport in $CuSbS_2$, as films from parallel experimental work have been shown to be slightly Cu poor[39, 114]. We note that intrinsic ionic defects (such as Cu vacancies) are not the focus of this study, but is an area that is of current investigation.

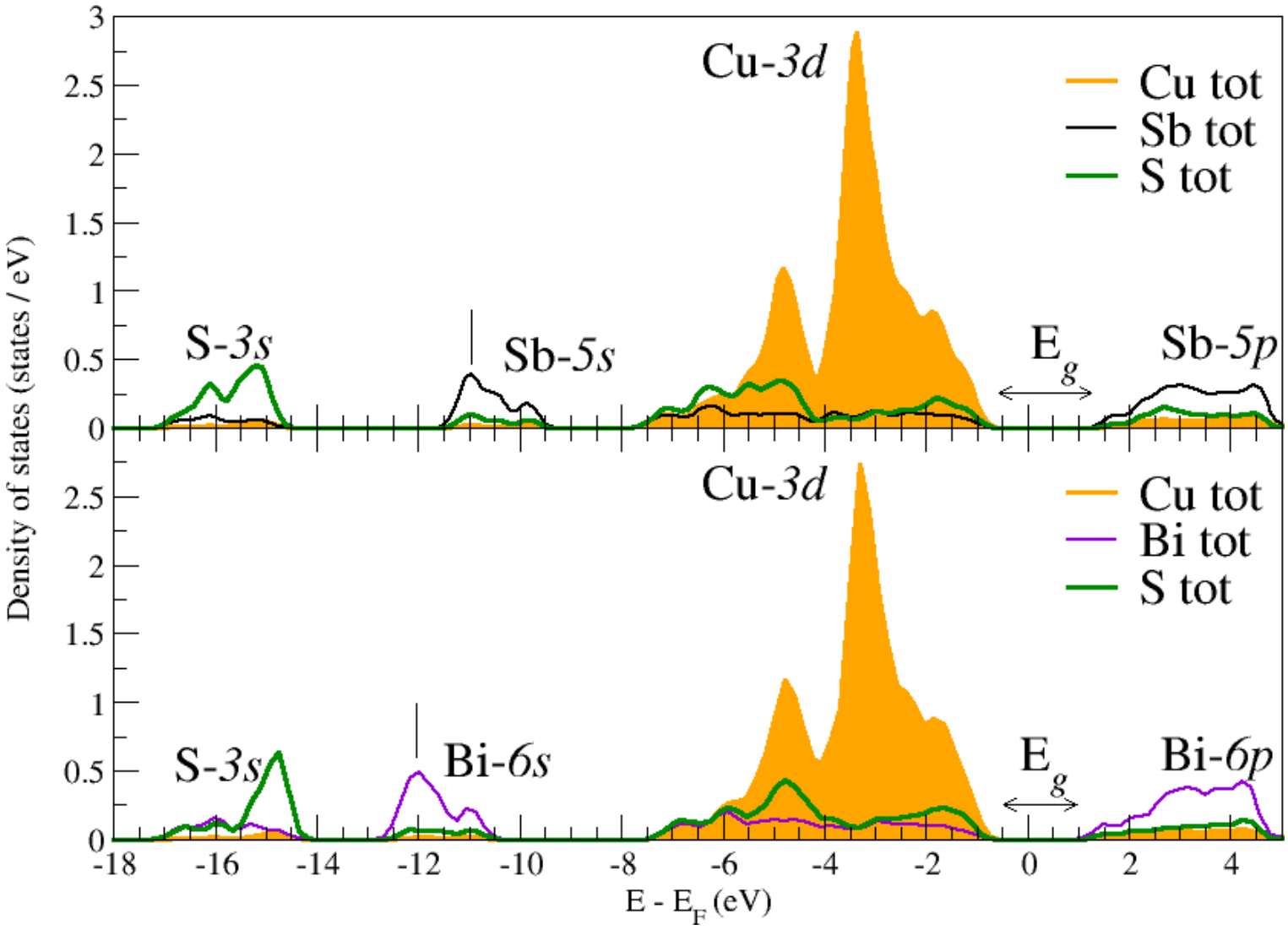

Figure 3.2: (Colour online) Orbital-projected density of states for $CuSbS_2$ (top) and $CuBiS_2$ (bottom) indicating the Cu, Sb, Bi and S states.

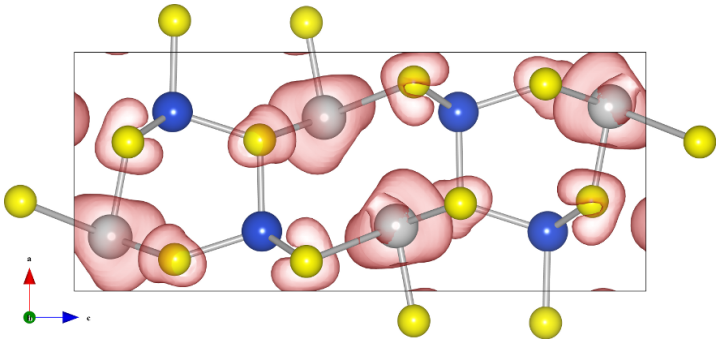

(a) $CuSbS_2$ conduction band

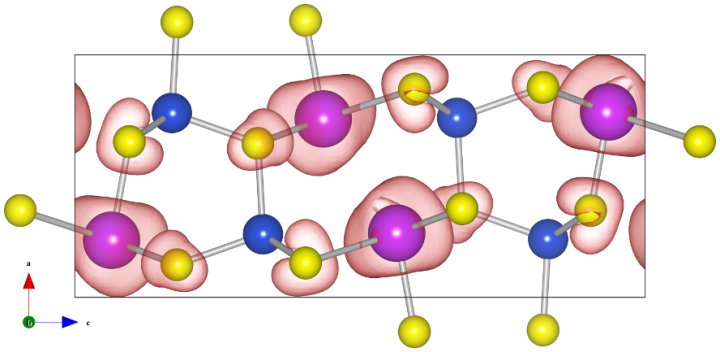

(b) $CuBiS_2$ conduction band

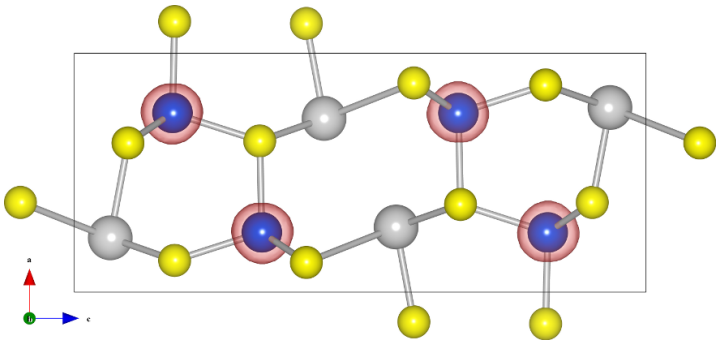

(c) $CuSbS_2$ valence band

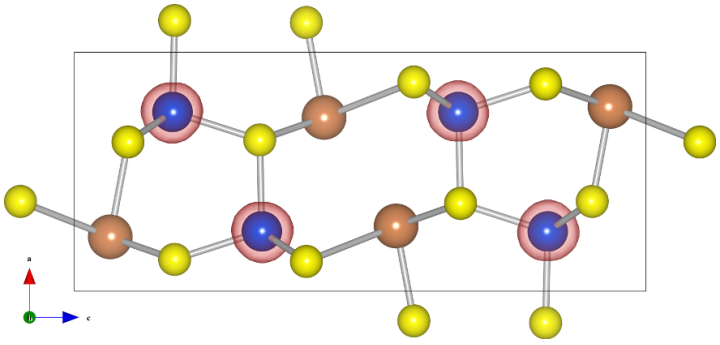

(d) $CuBiS_2$ valence band

Figure 3.3: Charge density calculated for the top of the valence band ($E - E_F = -3.5 \rightarrow 0eV$) and the bottom of the conduction band ($E - E_F = 1 \rightarrow 5eV$) in $CuSbS_2$ and $CuBiS_2$. Colours are similar to Figure 3.1; Cu (blue), Sb (grey), Bi (pink), S (yellow), charge density (red)

3.6 Local Structural Environment

The majority of PV materials are based around regular tetrahedral networks at the atomic level (zinc-blende or wurtzite crystal structures). A comprehensive understanding of the structure and bonding in $CuSbS_2$ and $CuBiS_2$, due to their low symmetry structures, will be necessary in order to describe the surface and interfacial properties that will be key in the design and optimisation of improved photovoltaic devices.

When we compare the local environment of the MS_5 (M = Sb/Bi) square pyramids we find considerable local distortion. The Sb/Bi ions are not centrally located within the basal plane of the MS_5 square pyramids as one might expect based on Valence Shell Electron Pair Repulsion (VSEPR) theory[120]. The structural distortions arise as a result of electronic effects relating to the Sb/Bi lone pairs.

Considering the structural deformations, we find that in $CuSbS_2$ the distorting effect of the stereoactive lone pair causes more structural distortion than in $CuBiS_2$, as measured by inspection of the largest difference (Δ_{max}) between the M-S bond lengths and S-M-S angles listed in Table 3.3, where we also find good agreement with the experimental values. As with the experimental work of Kyono *et al.*[111] we observe that the Sb 5s lone pair seems to be more stereochemically active in terms of repelling the neighbouring Cu than the Bi 6s lone pair; the M-Cu distance is very similar in the two materials, 3.414 Å and 3.422 Å for $CuSbS_2$ and $CuBiS_2$ respectively. This result is despite the discrepancy between the ionic radii of Sb and Bi. Interestingly this does not lead to the CuS_4 tetrahedra being more distorted in $CuSbS_2$ (Table 3.4). In fact the CuS_4 tetrahedra in $CuBiS_2$ are more irregular, but the deviations are much less significant than those in the MS_5 square pyramids.

Turning to the cause of the distortion of the MS_5 square pyramids, we have already noted that VSEPR theory is unable to provide an explanation. Essentially this is because VSEPR assumes a classical model of the lone pair(s) in the system, in which the s^2 electrons occupy a non-bonding orbital, and electrostatics control the coordination. Instead we can adopt the revised lone pair model of Walsh *et al.*[121], which has been used to rationalise the presence of lone pair induced structural distortions in other systems e.g. PbO and SnO.

In this revised model the s^2 lone pair electrons are no longer assumed to reside within a non-bonding orbital. They interact with valence band anion (S) p states and the resulting hybrids can be seen at the bottom (bonding) and top (antibonding) of the valence band. In certain systems where this antibonding orbital has considerable s character it is possible for the antibonding orbital to hybridize with the cation (Sb/Bi) p states. However this interaction cannot take place in undistorted structures as it is symmetry forbidden, consequently where this cation p - antibonding

Table 3.3: The average, and the largest difference (Δ_{max}) between, the bond lengths and the bond angles in the MS_5 square pyramids where M = Sb / Bi

	$CuSbS_2$	$CuBiS_2$
Bond lengths (Å)		
Mean M-S (calc)	2.759	2.821
Mean M-S (expt)	2.752	2.827
Δ_{max} (calc)	0.675	0.591
Δ_{max} (expt)	0.682	0.626
Bond angles (deg)		
Mean S-M-S (calc)	89.47	90.39
Mean S-M-S (expt)	88.68	90.22
Δ_{max} (calc)	20.85	19.68
Δ_{max} (expt)	14.69	12.62

Table 3.4: The average, and the largest difference (Δ_{max} between, the bond lengths and the bond angles in the CuS_4 tetrahedra

	$CuSbS_2$	$CuBiS_2$
Bond lengths (Å)		
Mean Cu-S (calc)	2.330	2.342
Mean Cu-S (expt)	2.317	2.329
Δ_{max} (calc)	0.021	0.049
Δ_{max} (expt)	0.019	0.042
Bond angles (deg)		
Δ_{max} (calc)	4.93	6.37
Δ_{max} (expt)	4.73	5.70

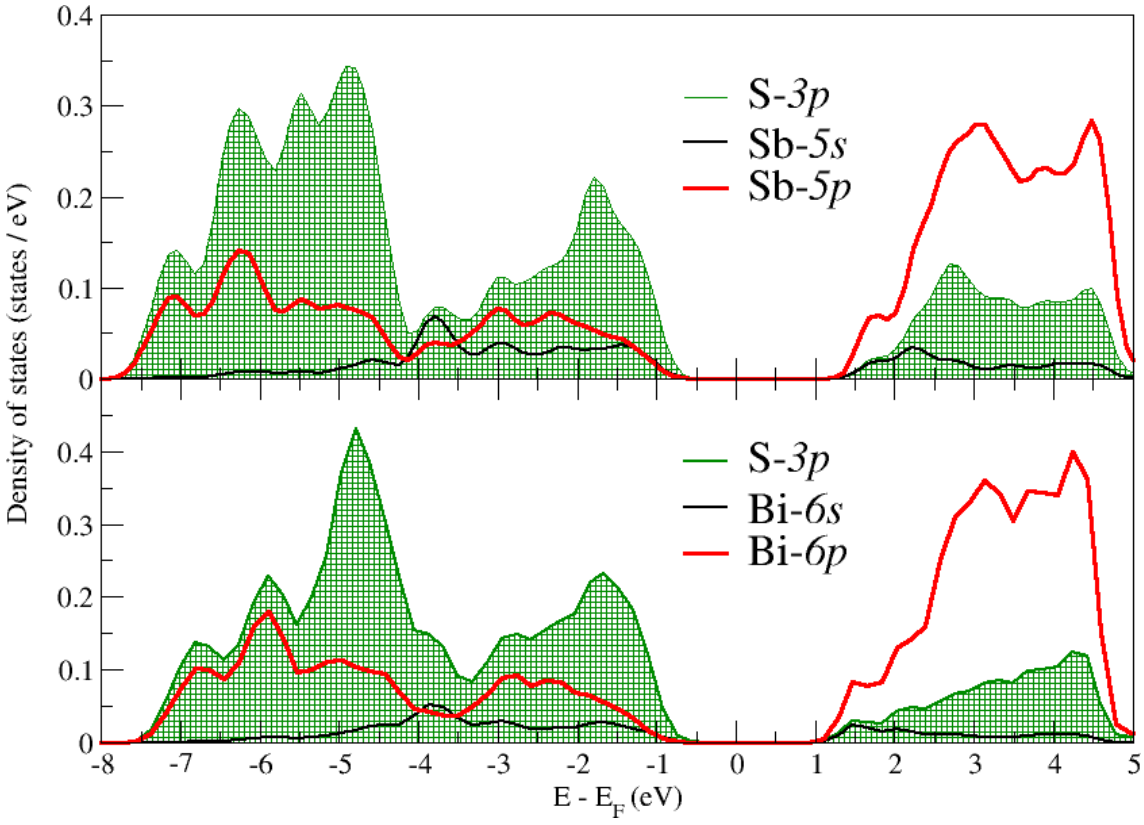

Figure 3.4: (Colour online) Partial orbital-projected density of states for $CuSbS_2$ (top) and $CuBiS_2$ (bottom)

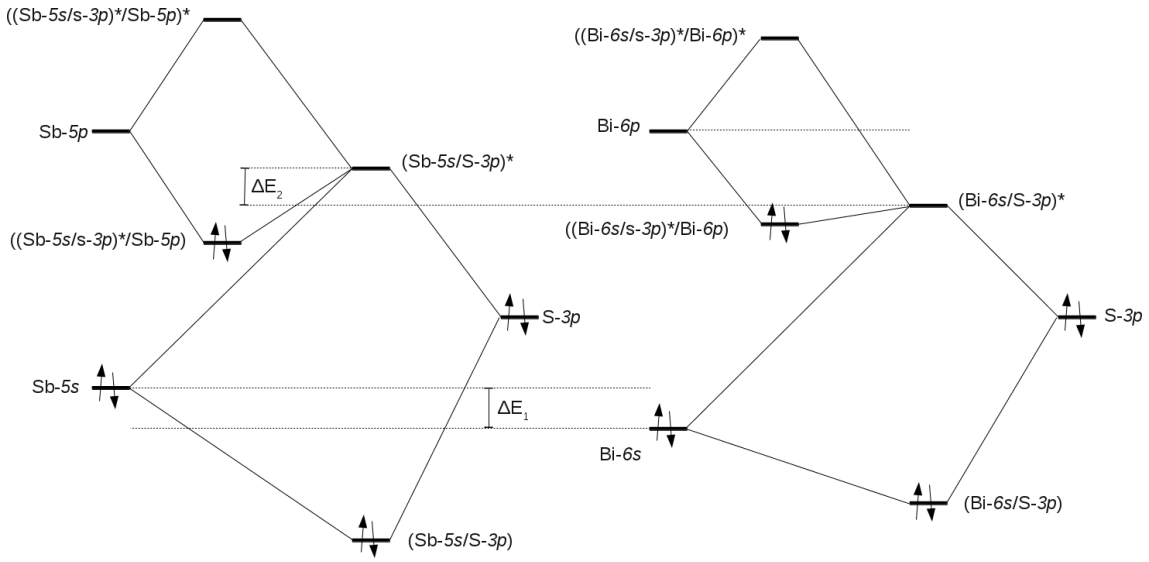

Figure 3.5: Energy level diagram of the orbitals relevant to the stereochemically active lone pair in $CuSbS_2$ and $CuBiS_2$, showing the difference in energy between the Sb-*5s* and Bi-*6s* orbitals - ΔE_1, and the consequent discrepancy in antibonding orbital energy - ΔE_2, leading to the varying stabilisation of the lone pair in the two materials.

hybridization offers significant stabilization the structure distorts removing the symmetry constraint. The electron density of the stabilized antibonding orbital forms a distorted lobe which is projected into the structural void like a classic lone pair.

When considering how this revised lone pair model can be applied to $CuSbS_2$ and $CuBiS_2$ it is helpful to consult Figures 3.4 and 3.5, which show the partial density of states in the valence and conduction bands for both materials, and an energy level diagram of the relevant orbitals respectively. Looking first at the partial density of states in Figure 3.4 for $CuSbS_2$ we can see a set of small peaks with an energy of -3 eV. These show the interaction of the (Sb-*5s*/S-*3p*)* orbital with the Sb-*5p* which as discussed above gives the stabilisation requiring structural distortion. When we visualise the orbitals present at this particular energy we clearly see the distorted lobe of electron density present as a result of this stabilised antibonding orbital, shown in Figure 3.6.

If we now consider $CuBiS_2$ we find that the peaks in Figure 3.4 are less pronounced. This can be rationalised as the binding energy of the Bi-*6s* orbital is lower than that of the Sb-*5s* (note ΔE_1 - Figure 3.5). Consequently the energies of the Bi-*6s* and S-*3p* are not as well matched as the Sb-*5s* and S-*3p* are. Therefore the resulting (Bi-*6s*/S-*3p*)* hybrid does not possess as much *s* orbital character as the (Sb-*5s*/S-*3p*)* hybrid. Thus the stabilisation available from interaction with the Bi-*6p* states is lower than that in $CuSbS_2$ (note ΔE_2 - Figure 3.5). These results help to rationalize the increased degree of structural distortion in $CuSbS_2$ in which the stabilization afforded by such distortion is greater than in $CuBiS_2$.

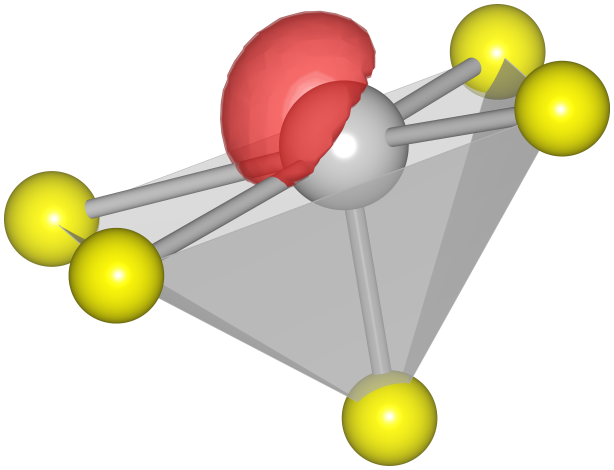

Figure 3.6: (Colour online) SbS_5 square pyramid showing: lone pair electron density (red), Sb (grey) and S (yellow).

3.7 Chapter Summary

The present study of $CuSbS_2$ and $CuBiS_2$ has used quantum chemical techniques to provide deeper fundamental insight into the electronic and local structural properties, which are of direct relevance to their use as absorber materials for thin-film solar cells.

The following main findings emerge from our investigations, which provide a strong basis for further characterization and optimization of these materials.

1. The calculations show excellent reproduction of the observed crystal structures of $CuSbS_2$ and $CuBiS_2$ including the unusual SbS_5 and BiS_5 coordination geometry.
2. A calculated band gap energy of 1.69 eV for $CuSbS_2$ is predicted, which agrees with the available experimental data, although this accord only occurs with the use of the HSE06 hybrid functional. For $CuBiS_2$ we predict a band gap of 1.55 eV that falls in the optimum range for a viable absorber material.
3. The results highlight the stereochemical activity of the Sb and Bi lone pair electrons rationalizing the asymmetric environment around Sb and Bi.
4. The density of states of both $CuSbS_2$ and $CuBiS_2$ indicate that the formation of hole carriers will occur in the Cu d^{10} band and hence will involve oxidation of Cu(I).

Further simulation work should include detailed studies of the defect and dopant properties of these materials.

The Toyota Auris HSD (Concept). The photovoltaic cells which are integrated into the vehicle's roof provide power to the on-board electronics and can also re-charge the battery of the hybrid engine.

Chapter 4

Structural, Defect and Ion-Transport Properties of Cu_2ZnSnS_4

4.1 Introduction

The need to develop lower cost and scalable photovoltaic technologies is clearly established[1]. In recent years there has been a concerted drive to develop new photovoltaic devices which can deliver on both of these fronts. As introduced in chapter 1, research into thin-film photovoltaics as a replacement technology for silicon-based devices has led to the development of photovoltaics which use CdTe or $CuInSe_2$ (CIS) as the basis of their absorber layer. CIS-based cells have achieved high efficiencies and CdTe-based cells have seen incremental price reductions, but there are concerns with these technologies. The scarcity of Te means that CdTe cells may not be a suitable choice for mass adoption. Also the high toxicity of Cd means that despite its inert nature when combined with Te, concerns about safety and the environmental impact of its use persist. While CIS based devices do not suffer from these limitations the price of In and Ga are high due to their relative scarcity and utility in other electronics applications, notably in Transparent Conducting Oxides (TCOs). This high cost will only be exacerbated by wide-spread use to manufacture photovoltaic devices. Therefore the limited cost reduction potential of CIS precludes it from offering the step-change in photovoltaic availability which is of critical importance to our energy supply. Hence the pressing need for new photovoltaic materials remains.

As mentioned in section 1.3.5, Cu_2ZnSnS_4 (CZTS) based compounds have generated the most interest of the range of materials investigated as replacements for CIGS. CZTS exhibits many properties which are desirable in thin-film absorber layers: it has a high optical absorption coefficient ($\approx 1 \times 10^4 \mathrm{cm}^{-1}$) and a direct band gap of near optimum energy (1.44-1.51 eV), as well as exhibiting p-type conductivity[45–

48]. Devices utilising alloys of CZTS and CZTSe have achieved efficiencies in excess of 10%[49, 50]. However some key aspects of the materials chemistry of CZTS are yet to be fully characterised. This chapter details calculations which have been performed using both interatomic potential methods and density functional theory and were focused on investigating the fundamental defect chemistry and ion migration of CZTS. Some background on experimental and structural studies of CZTS is first outlined, before presenting results of the computational studies.

4.2 Fabrication of Cu_2ZnSnS_4 Thin-films

In recent years there has been a considerable drive to develop synthetic routes which will enable facile large-scale production of Cu_2ZnSnS_4 thin-films for photovoltaic and other technological applications. Early work on Cu_2ZnSnS_4 used a range of vacuum-based deposition techniques such as atomic beam, sputtering/hybrid sputtering and evaporation deposition techniques [46, 47, 122–126]. The methods generally involve creation of a mixed-metal stack or off-stoichiometry mixed-metal sulphide which is annealed in a sulphur-rich atmosphere to yield Cu_2ZnSnS_4. Although the control over stoichiometry is good, the presence of secondary phases persists.

To complement the vacuum based methods a range of non-vacuum processes have been investigated for the synthesis of Cu_2ZnSnS_4. Principally this is because the vacuum-based methods offer limited throughput, low material utilisation and have high energy consumption; hence it is thought that the use of vacuum-based methods will preclude the stark cost limitation needed to allow CZTS-based PV to expand dramatically. Experimental groups have used a range of non-vacuum processes to produce Cu_2ZnSnS_4; these include: spray pyrolysis, electrochemical deposition and chemical vapour deposition [45, 127–131]. To date it is the work of Todorov *et al.*[49, 50] which has produced Cu_2ZnSnS_4 films yielding the highest efficiency photovoltaic devices. They use a hydrazine-based particle-solution slurry process to create films which are then partially selenised to give the mixed-metal sulphur-selenium alloy $Cu_2ZnSn(S,Se)_4$[49, 50, 98].

A key issue in the majority of synthetic routes to produce Cu_2ZnSnS_4 is the control over stoichiometry and secondary phases. The ratios of the multiple cation species are difficult to control during synthesis, and losses due to formation of unwanted co-products, e.g. ZnS are common. Even if the stoichiometry is controlled precisely, secondary phases, principally the binary sulphides and Cu_3SnS_4, are produced and are difficult to detect with standard characterisation methods. Calculations by Chen *et al.* have shown that stoichiometric Cu_2ZnSnS_4 is stable only in a very narrow chemical potential window[132, 133].

It has been found that Cu-poor Cu_2ZnSnS_4 samples often provide superior PV performance[129, 134], in which the main competing phase is ZnS[135]. It is clear that more detailed knowledge of the defect chemistry of Cu_2ZnSnS_4 can help to

rationalise these observations.

4.3 Structure of Cu_2ZnSnS_4

The structure of CZTS is closely related to that of the ternary chalcogenides (e.g. $CuInS_2$) described in section 1.3.4. The quaternary Cu_2ZnSnS_4 is derived by cation mutation from these $CuM^{3+}S_2$ materials. As Zn^{2+} and Sn^{4+} replace $2M^{3+}$ cations. Cu_2ZnSnS_4 remains isoelectronic with the $CuMS_2$ materials as the total valence of the cations is conserved throughout the substitutions.

Cu_2ZnSnS_4 has a large number of polymorphs which arise as a result of the many cation ordering schemes which are possible with 3 distinct cation species. The issue of polymorphism in Cu_2ZnSnS_4 is addressed in chapter 5. For now we will consider the two polymorphs which are most commonly discussed, namely kesterite and stannite. The unit cell and a $2 \times 1 \times 1$ supercell for these polymorphs are shown in Figures 1.8 and 4.1 respectively. It can be seen that the structure is based on a regular tetrahedral network with the cations arranged in layers parallel to the *ab* plane. Kesterite (orthorhombic space group $I\bar{4}$) is the lowest energy polymorph, which is distinguished from the related low energy polymorph stannite (orthorhombic space group $I\bar{4}2m$) by the arrangement of the cations, as shown in Figure 4.1. In both cases the anion sub-lattice remains unchanged. In the kesterite polymorph the layers of cations perpendicular to the *c* axis alternate between layers of CuZn and layers of CuSn, whereas in stannite these layers alternate between layers of SnZn and layers of CuCu.

It should be noted that some experimental groups[136–138] often assign kesterite the higher symmetry space group $I\bar{4}2m$ rather than $I\bar{4}$, or state their inability to determine the sample's polymorph, as they are unable to discern any order in the CuZn layers. Whether this is due to the inability to resolve the isoelectronic Cu^+ and Zn^{2+} ions with XRD or is due to a lack of order in the samples is not always clear. In simulations it is often necessary to impose an explicit ordering scheme and this is done in the vast majority of this work. Throughout this thesis the term "kesterite" denotes the cation configurations shown in Figures 1.8 and 4.1

4.4 Modelling Objectives and Methods

At the inception of this work, the fabrication of Cu_2ZnSnS_4 for use in experimental photovoltaic devices was a recent development. There was limited understanding of the fundamental physical and defect properties of CZTS. The calculations described in the following sections were performed with the objective of building a greater understanding of the basic defect and ion transport properties of CZTS. Overall,

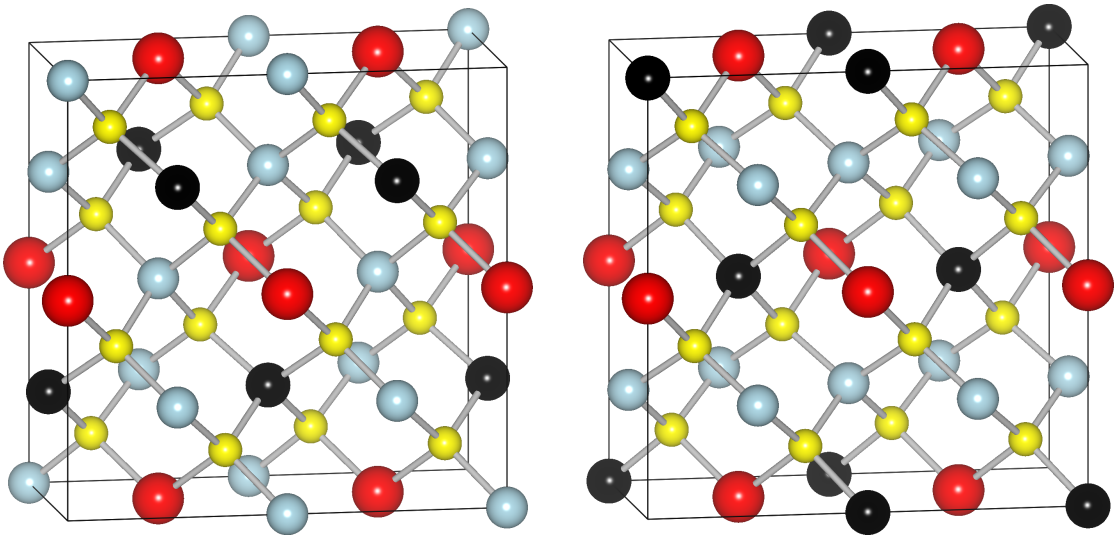

(a) (b)

Figure 4.1: The kesterite (a) and stannite (b) polymorphs of Cu_2ZnSnS_4 showing; Cu (green), S (yellow), Zn (black) and Sn (red).

the objective was to identify how these properties impacted the function of the experimental devices being produced, and if possible to identify how synthesis and device production could be modified in order to improve performance.

This chapter summarises the results of a large number of interatomic potential based calculations, with details of the computational methods used given in Chapter 2. The interatomic potentials used describe the interatomic interactions in accordance with the Born model[64], in which the potential energy includes a long-range Coulombic component and short-range terms which represent Pauli repulsion and dispersive energies. The short-range terms, which have a cut-off of 12Å, are specified in the Buckingham form.

For the treatment of defects, such as Cu'_{Zn} or V'_{Cu}, the two-region strategy of Mott and Littleton has been used. In these studies the spherical regions 1 and 2a extend 25Å and 40Å from the centre of the defect respectively. These large region sizes, in which region 1 and 2a contained approximately 4800 and 15,000 ions respectively, became necessary when calculating the formation energy of large antisite clusters. The size of region 1 must be sufficiently large to prevent the outermost defects of the cluster being less than 12Å from the region 1/2a boundary, in which case the effect of the short-range potential would extend into region 2a.

For the study of Cu migration we have employed the Nudged Elastic Band (NEB) method. A series of 20 correlated energy minimisation calculations was performed on a $2 \times 2 \times 1$ pseudo-cubic ($a \approx b \approx c \approx 10.8$Å) supercell of Cu_2ZnSnS_4 containing 63 atoms. This was done using both the interatomic potentials and Density Functional Theory (DFT) formalisms.

The DFT calculations have utilised the semi-local Generalised Gradient Approximation (GGA) functional of Perdew, Burke and Ernzerhof[82] in conjunction with the Plane Augmented Wave (PAW) method for treatment of the core electrons. For sampling of the Brillouin-zone a $4 \times 4 \times 4$ Monkhorst-Pack mesh of *k-points* was used.

4.5 Results and Discussion

4.5.1 Derivation of Potentials and Structural Modelling

The first stage in the computational simulation of Cu_2ZnSnS_4 was the derivation of a potential model able to successfully reproduce the complex experimental structure. The work of Paier *et al.*[103] had shown the largely ionic nature of CZTS, with the Cu-S and Zn-S interactions being almost exclusively ionic and the Sn-S interactions being 75% ionic in nature. Thus we investigated whether CZTS could be modelled effectively solely by interatomic potentials. Initially the work of Wright *et al.* on the inter-atomic potential modelling of metal sulphides[71, 72, 139, 140], including ZnS, was taken as the basis for our potential model of Cu_2ZnSnS_4. The Zn-S and S-S potentials from ref [139] were transferred directly and the Zn-S parameters was also used as the starting point for a refinement of the Cu-S and Sn-S potentials. These were fitted to the experimental structure of Cu_2ZnSnS_4, provided by the structural work of Bonazzi *et al.*[141], and also to the experimental structures of the binary sulphides Cu_2S[142], ZnS[143] and SnS_2[144].

The parameters for this first potential model (termed *potential 1*) are given in appendix B (Table B.1). While potential 1 successfully reproduced the crystal structures of kesterite and stannite Cu_2ZnSnS_4 with a high level of accuracy, the three-body term is expressed in an unusual form;

$$\phi_{ijk} = \frac{1}{2}k(\theta - \theta_0)^2 e^{-\left(\frac{r_{ij}}{\rho_{ij}}\right)} e^{-\left(\frac{r_{ik}}{\rho_{ik}}\right)} \tag{2.14}$$

This form of the three-body term is not supported in the METADISE code or for the implementation of the NEB method in GULP, which greatly hampers the study of ion-transport and surface properties using potential 1.

Hence, a second set of potential parameters was sought, that would be able to describe the inter-atomic interactions in Cu_2ZnSnS_4 without the use of higher order terms. This was achieved by sampling a large section of the parameter space for the Cu-S, Zn-S and Sn-S pair potentials, which retained the Buckingham form. The parameters A and ρ were systematically sampled with two scans. The first being a relatively coarse grid consisting of 250047 data points which was used to direct the second scan which had a finer sampling grid consisting of 481284 data points. The

Table 4.1: Parameters of potential A used to model Cu_2ZnSnS_4

Buckingham Term	A (eV)	ρ (Å)	c (eV/Å^6)
S - S	1200.00	0.1490	0.0
S - Cu	2434.65	0.2789	0.0
S - Zn	2433.39	0.3174	0.0
S - Sn	2468.24	0.3551	0.0
Species	**Core charge (e)**	**Shell Charge (e)**	**Spring k(eV/Å^2)**
S	1.03061	-3.03061	13.302743
Cu	1.0	-	-
Zn	2.0	-	-
Sn	4.0	-	-

Buckingham potential parameters from each data point were refined to optimise the reproduction of the crystal structure of kesterite Cu_2ZnSnS_4 using the least squares fitting regime in GULP. Candidate potentials were then filtered to exclude those yielding imaginary phonon frequencies and then sorted by their ability to reproduce the experimental structure (of both kesterite and stannite). This sampling method ensured that the vast majority of the parameter space was investigated. Thus the final potential parameters should correspond to the most appropriate of a range of possible parameter combinations. The final parameters resulting from this scan based method, and hence referred to as potential A, are given in Table 4.1.

Our discussion will focus on the results of potential A[†] in order to maintain consistency with the studies of surface properties presented in chapter 5. Tables of results from the use of potential 1 are included in Appendix B.

We have used the interatomic potentials described in Table 4.1 to perform energy minimisation calculations upon the orthorhombic unit cells of kesterite and stannite Cu_2ZnSnS_4, which each contain two formula units of CZTS. Lattice vectors and ionic positions are subject to full relaxation. Table 4.2 compares the lattice parameters and bond lengths to the experimental structural studies of Bonazzi *et al.*[141]. It can be seen that the structures of both kesterite and stannite Cu_2ZnSnS_4 are reproduced to high accuracy, with lattice parameters and bond lengths deviating from experimental results by less than 0.1Å.

[†]With the exception of the discussion of defect clusters. These calculations were not repeated with potential A as a more extensive study of cation ordering/polymorphism was performed, this is described in chapter 5.

Table 4.2: Comparison of calculated lattice parameters and bond lengths in kesterite and stannite Cu_2ZnSnS_4 with experimental data[141].

			kesterite		stannite	
Property		Experiment	Calculated	Δ	Calculated	Δ
a, b	/Å	5.434	5.484	0.050	5.454	0.020
c	/Å	10.856	10.875	0.019	10.874	0.018
Volume	/Å^3	320.560	327.039	6.479	323.480	2.920
$\alpha = \beta = \gamma$	(°)	90	90	0	90	0
Cu(1)-S	/Å	2.334	2.282	-0.052	2.272	-0.060
Cu(2)-S	/Å	2.332	2.311	-0.021	-	-
Zn-S	/Å	2.334	2.409	0.075	2.428	0.094
Sn-S	/Å	2.409	2.480	0.071	2.481	0.072

[a]It should be noted that as there is no experimental data on the structure of phase pure stannite Cu_2ZnSnS_4, ionic positions in the inputs of our calculations are inferred from those in kesterite.

4.5.2 Intrinsic Defect Chemistry of Cu_2ZnSnS_4

Due to the recent emergence of Cu_2ZnSnS_4 very little is known about its intrinsic defect chemistry. To address this we have investigated the formation of full and partial Schottky disorder, Frenkel disorder and cation anti-site defects within the Cu_2ZnSnS_4 lattice. The formation processes for these defects are described by equations 4.1-4.12.

$$\text{Full Schottky}: \quad 2Cu_{Cu}^{x} + Zn_{Zn}^{x} + Sn_{Sn}^{x} + 4S_{S}^{x} \rightarrow 2V_{Cu}^{\prime} + V_{Zn}^{\prime\prime} + V_{Sn}^{\prime\prime\prime\prime} + 4V_{S}^{\cdot\cdot} + Cu_2ZnSnS_4 \tag{4.1}$$

$$Cu_2S\,\text{Schottky}: \quad 2Cu_{Cu}^{X} + S_{S}^{x} \rightarrow 2V_{Cu}^{\prime} + V_{S}^{\cdot\cdot} + Cu_2S \tag{4.2}$$

$$ZnS\,\text{Schottky}: \quad Zn_{Zn}^{x} + S_{S}^{x} \rightarrow V_{Zn}^{\prime\prime} + V_{S}^{\cdot\cdot} + ZnS \tag{4.3}$$

$$SnS_2\,\text{Schottky}: \quad Sn_{Sn}^{x} + 2S_{S}^{x} \rightarrow V_{Sn}^{\prime\prime\prime\prime} + 2V_{S}^{\cdot\cdot} + SnS_2 \tag{4.4}$$

(4.5)

$$\text{Cu Frenkel}: \quad Cu_{Cu}^{x} \rightarrow V_{Cu}^{\prime} + Cu_{i}^{\cdot} \tag{4.6}$$

$$\text{Zn Frenkel}: \quad Zn_{Zn}^{x} \rightarrow V_{Zn}^{\prime\prime} + Zn_{i}^{\cdot\cdot} \tag{4.7}$$

$$\text{Sn Frenkel}: \quad Sn_{Sn}^{x} \rightarrow V_{Sn}^{\prime\prime\prime\prime} + Sn_{i}^{\cdot\cdot\cdot\cdot} \tag{4.8}$$

(4.9)

$$\text{Cu/Zn Antisite}: \quad Cu_{Cu}^{x} + Zn_{Zn}^{x} \rightarrow Zn_{Cu}^{\cdot} + Cu_{Zn}^{\prime} \tag{4.10}$$

$$\text{Zn/Sn Antisite}: \quad Zn_{Zn}^{x} + Sn_{Sn}^{x} \rightarrow Sn_{Zn}^{\cdot\cdot} + Zn_{Sn}^{\prime\prime} \tag{4.11}$$

$$\text{Cu/Sn Antisite}: \quad Cu_{Cu}^{x} + Sn_{Sn}^{x} \rightarrow Cu_{Sn}^{\prime\prime\prime} + Sn_{Cu}^{\cdot\cdot\cdot} \tag{4.12}$$

The energies for each of the isolated vacancy, interstitial and substitutional defects in equations 4.1-4.12 have been calculated and are given in Tables 4.3, 4.4 and 4.5 respectively. The interstitial positions of the $Cu_i^{\cdot}$ defects are shown in Figure 4.2. Although Figure 4.2 shows the Cu interstitials in kesterite Cu_2ZnSnS_4 the positions

Table 4.3: Isolated defect energies for vacancy defects in kesterite and stannite Cu_2ZnSnS_4

Type of Vacancy	Symbol	Defect energy / eV	
		Kesterite	Stannite
Cu(1)	V'_{Cu}	6.35	6.37
Cu(2)	V'_{Cu}	6.33	6.37
Zn	V''_{Zn}	21.26	21.07
Sn	V''''_{Sn}	76.33	79.27
S	$V^{\cdot\cdot}_{S}$	21.50	21.38

Table 4.4: Isolated defect energies for interstitial defects in kesterite and stannite Cu_2ZnSnS_4

Interstitial Species	Coordinates	Kesterite layer	Kesterite E_{defect} /eV	Stannite layer	Stannite E_{defect} /eV
Cu'_i	(0,$^1/_2$,0), (0,$^1/_2$,$^1/_2$), ($^1/_2$,0,0), ($^1/_2$,0,$^1/_2$)	CuSn	-3.14	CuCu	-3.81
Cu'_i	($^1/_2$,$^1/_2$,$^1/_4$), (0,0,$^1/_4$), ($^1/_2$,$^1/_2$,$^3/_4$), (0,0,$^3/_4$)	CuZn	-3.71	ZnSn	-3.56
Zn''_i	(0,$^1/_2$,0), (0,$^1/_2$,$^1/_2$), ($^1/_2$,0,0), ($^1/_2$,0,$^1/_2$)	CuZn	-14.06	CuCu	-12.91
Zn''_i	($^1/_2$,$^1/_2$,$^1/_4$), (0,0,$^1/_4$), ($^1/_2$,$^1/_2$,$^3/_4$), (0,0,$^3/_4$)	CuSn	-14.42	ZnSn	-13.23

remain unchanged in the stannite structure and consequently the corresponding diagram has been omitted.

The energies of the relevant point defects are combined to give the formation energies of the defect reactions, in both the kesterite and stannite polymorphs of Cu_2ZnSnS_4, and these energies are given in Tables 4.6 and 4.7.

Schottky and Frenkel Disorder

Table 4.6 details the energies for the Schottky, Schottky-type and Frenkel defects described by equations 4.1-4.7. The magnitudes of the energies for these defect processes suggest that all forms of Schottky type defect have a high defect formation energy. Consequently it is suggested that Schottky type defects will not be present in the Cu_2ZnSnS_4 lattice in significant quantities irrespective of polymorph. There

Table 4.5: Isolated defect energies for substitutional defects in Cu_2ZnSnS_4

Defect type	Defect energy /eV	
	Kesterite	Stannite
Cu'_{Zn}	13.25	13.18
Cu'''_{Sn}	68.20	68.12
$Zn^{\cdot}_{Cu}$	-11.79	-11.82
Zn''_{Sn}	51.74	51.69
$Sn^{\cdot\cdot}_{Zn}$	-45.66	-45.38
$Sn^{\cdot\cdot\cdot\cdot}_{Cu}$	-54.70	-55.12

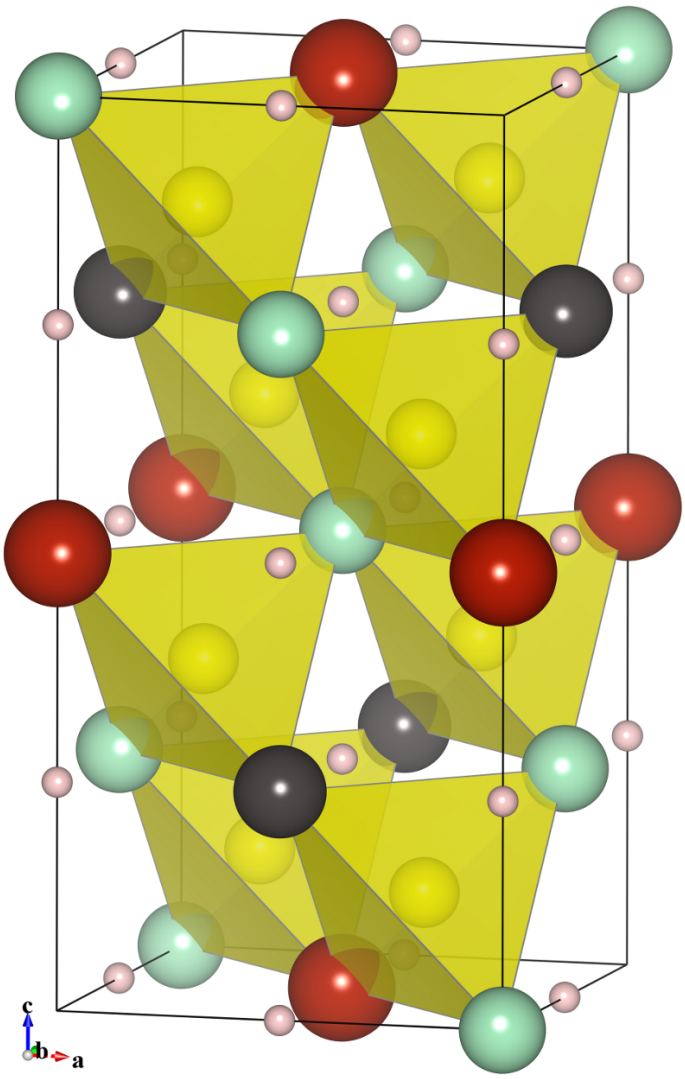

Figure 4.2: Schematic showing the favoured $Cu_i^{\cdot}$ interstitial positions (small pink spheres) in kesterite Cu_2ZnSnS_4. Colours are similar to previous figures; Cu (green), Zn (black), Sn (red), S polyhedra (yellow).

Table 4.6: Formation energies for the Schottky and Frenkel defects in Cu_2ZnSnS_4

Defect	Equation	Total Formation Energy / eV	
		kesterite	stannite
Full Schottky	4.1	35.68	38.08
Cu_2S Schottky	4.2	7.95	7.89
ZnS Schottky	4.3	8.52	8.22
SnS_2 Schottky	4.4	31.8	34.5
Cu Frenkel	4.6	2.46	2.56
Zn Frenkel	4.7	6.84	7.84
Sn Frenkel	4.8	-	≈20

are small deviations in the calculated Schottky defect formation energies between kesterite and stannite but even the formation energy of the Cu_2S Schottky in stannite, which is the lowest of all the Schottky type defects investigated, is too high to allow appreciable concentrations to form.

The Cu Frenkel has a much lower formation energy, being ≈1.25 eV defect^{-1}. At the elevated temperatures experienced in some synthetic routes, it could contribute to significant concentration of copper vacancies (V'_{Cu}) and interstitials ($Cu^{\cdot}_i$). The mobility of these may explain the increased rate of Cu diffusion in synthesis relative to the other constituents, a point we return to below.

It should be noted that it has not been possible to calculate the energy for the tin interstitial defect ($Sn^{\cdots\cdot}_i$) in kesterite Cu_2ZnSnS_4, as the introduction of the highly charged Sn^{4+} ion caused massive structural relaxation. In stannite Cu_2ZnSnS_4 the defect energy of $Sn^{\cdots\cdot}_i$ was calculated to be -51.98 eV and -52.19 eV, when the interstitial was located in the Cu-Cu layer and in the Zn-Sn layer respectively, leading to a Frenkel defect energy of ≈20 eV. Clearly this is too high to allow any considerable concentration of Sn Frenkel defects to form in stannite Cu_2ZnSnS_4. Given that the formation energies for all the other defects studied have varied little between kesterite Cu_2ZnSnS_4 and stannite Cu_2ZnSnS_4 it is fair to assume that the Sn Frenkel also has a high formation energy in kesterite Cu_2ZnSnS_4.

Antisite Disorder

By far the most significant result of the intrinsic defect calculations is the formation energies of the antisite defects, listed in Table 4.7. While the energies of the Zn/Sn and Cu/Sn antisites are high, the formation energy of the Cu/Zn antisite is considerably lower. The fact that antisite disorder is the lowest energy form of intrinsic defect sets Cu_2ZnSnS_4 apart from the $CuInSe_2$ materials where Cu vacancy disorder is dominant[145].

Table 4.7: Defect formation energies (E_F) and cluster binding energies (E_{bind}) for antisite defects in kesterite and stannite Cu_2ZnSnS_4

Defect	Equation	Isolated defects		Pair cluster		Binding energy	
		E_F / eV	E_F / eV defect^{-1}	E_F / eV	E_F / eV defect^{-1}	E_{bind} / eV	E_{bind} / eV defect^{-1}
kesterite							
Cu/Zn Antisite	4.10	1.46	0.73	0.64	0.32	-0.82	-0.41
Zn/Sn Antisite	4.11	6.08	3.04	2.76	1.38	-3.32	-1.66
Cu/Sn Antisite	4.12	13.50	6.75	6.32	3.16	-7.18	-3.59
stannite							
Cu/Zn Antisite	4.10	1.36	0.68	0.56	0.28	-0.80	-0.40
Zn/Sn Antisite	4.11	6.32	3.16	2.92	1.46	-3.40	-1.70
Cu/Sn Antisite	4.12	13.00	6.50	5.82	2.91	-7.18	-3.59

For the case of a pair of isolated defects, the Cu/Zn antisite has a formation energy of 1.46 eV and 1.36 eV in kesterite and stannite respectively. In the case of the pair cluster where the Cu'_{Zn} and $Zn^{\cdot}_{Cu}$ are found together as nearest neighbours, rather than spaced apart in the lattice, the formation energy drops to 0.64 eV and 0.56 eV in kesterite and stannite respectively.

Clearly these values suggest that there will be significant levels of Cu/Zn antisite disorder in Cu_2ZnSnS_4. This is in accord with experimental data, where the work of Bonazzi *et al.*[141] predicts no order in the Cu-Zn layers in "kesterite" and assigns the $I\bar{4}2m$ space group as a result. However, as previously noted the inability of XRD to resolve Cu^+ and Zn^{2+} could be critical here. The work of Schorr *et al.*[146, 147] has used neutron diffraction to study Cu_2ZnSnS_4 and also found a lack of ordering in the Cu-Zn layers.

Interestingly, the finding that the formation energy of the Cu/Zn antisite is lower in stannite Cu_2ZnSnS_4 than in kesterite Cu_2ZnSnS_4 can be explained, as Cu/Zn antisite disorder in stannite will lead to the partial formation of the lower energy kesterite phase.

Turning to the issue of antisite defect aggregation, Table 4.7 shows that there is a favourable binding energy between the oppositely charged substitutional defects Cu'_{Zn} and $Zn^{\cdot}_{Cu}$. Electrostatic attraction and elastic interactions between these charged species makes formation of a defect pair cluster favoured over isolated defects. This is significant as it indicates that like CIGS where neutral defect complexes such as $[In^{\cdot\cdot}_{Cu} + 2V'_{Cu}]$ are formed[145], the native defects in Cu_2ZnSnS_4 could exhibit self-passivation behaviour. Self-passivation is important as charged defects can act as charge-carrier traps, and therefore act as recombination centres which dramatically reduce a material's effectiveness in a photovoltaic device.

Following this finding we performed a series of cluster calculations[†] to investigate whether this defect aggregation is limited to pair clusters or whether larger microdomains of Cu/Zn antisite defects will be formed. Table 4.8 shows the formation energies (E_F) and binding energies (E_{bind}) for clusters of antisite defects consisting of up to 8 substitutional defects. There is an increase in binding energy from -0.31 eV defect^{-1} to -0.43 eV defect^{-1} when moving from the two-defect to four-defect cluster. For the larger clusters the precise configuration greatly affects the binding energy. While the lowest energy configurations for the six-defect and eight-defect clusters have higher binding energies, -0.44 eV defect^{-1} and -0.45 eV defect^{-1} respectively, the difference is small.

As can be seen from Table 4.8 the defect configuration has a significant effect on the binding energy of the larger antisite clusters. The asymmetric clusters are less

[†]These calculations were performed using potential 1 and have not been repeated with potential A as a more rigorous investigation of cation ordering in Cu_2ZnSnS_4 has been carried out using DFT, the results of which are discussed in chapter 5.

Table 4.8: Defect formation energies (E_F) and binding energies (E_{bind}) for a range of antisite clusters of varying sizes in kesterite Cu_2ZnSnS_4.

Configuration	E_F / eV	E_F / eV defect^{-1}	E_{bind} / eV	E_{bind} / eV defect^{-1}
2 substitutional defects (pair cluster)				
1	0.5	0.25	-0.61	-0.31
4 substitutional defects				
1	0.73	0.18	-2.59	-0.43
6 substitutional defects				
1	1.07	0.18	-2.25	-0.37
2	1.03	0.17	-2.29	-0.38
3	1.03	0.17	-2.29	-0.38
4	0.70	0.12	-2.62	-0.44
5	-	-	-	-
6	1.11	0.19	-2.21	-0.37
8 substitutional defects				
1	0.82	0.10	-3.60	-0.45
2	1.12	0.14	-3.31	-0.41
3	1.18	0.15	-3.25	-0.41
4	1.21	0.15	-3.21	-0.40
5	-	-	-	-
6	1.21	0.15	-3.21	-0.40
7	1.10	0.14	-3.33	-0.42
8	1.29	0.16	-3.14	-0.39
9	1.48	0.19	-2.94	-0.37
10	1.21	0.15	-3.21	-0.40
11	1.67	0.21	-2.75	-0.34
12	1.12	0.14	-3.31	-0.41
13	1.39	0.17	-3.03	-0.38
14	1.39	0.17	-3.04	-0.38
15	2.56	0.32	-1.87	-0.23
16	1.36	0.17	-3.07	-0.38
17	1.57	0.20	-2.86	-0.36

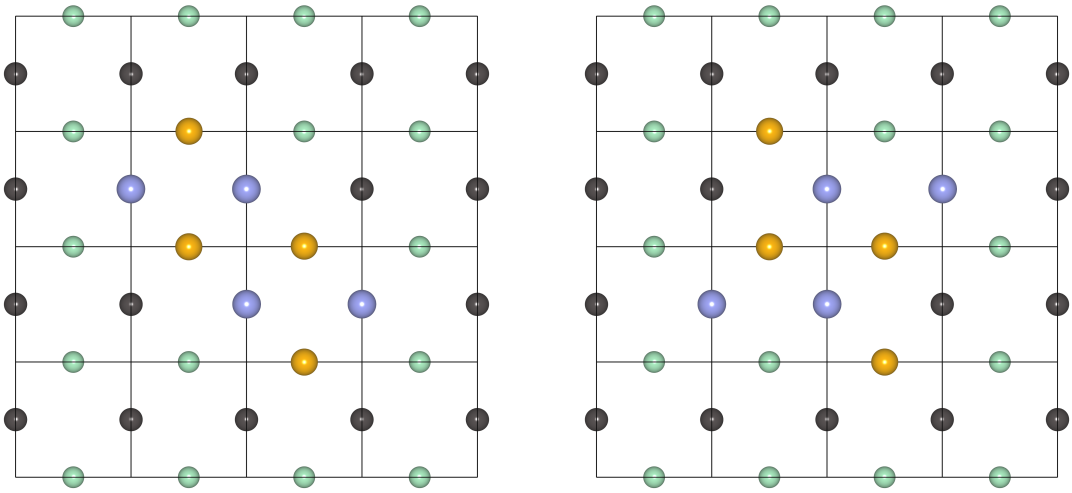

(a) (b)

Figure 4.3: The highest (a) and lowest (b) energy configurations of the 8 defect antisite cluster. The *ab* plane of kesterite Cu_2ZnSnS_4 is shown viewed along the *c* axis, colours similar to Figures 4.1 and 1.8 are used; Cu^{x}_{Cu} (light green), Zn^{x}_{Zn} (black), Cu'_{Zn} (light blue) and $Zn^{\cdot}_{Cu}$ (orange).

strongly bound. Interestingly the symmetry of the configurations with the highest and lowest binding energies are the same, both belong to the C_{2h} point group and are shown in Figure 4.3. It appears that configurations which are strongly bound minimise disruption of the cation ordering along the diagonals (1 1 0) and (-1 1 0). While considering the ordering of these cation antisite clusters it became clear that a more rigorous approach to the investigation of the cation ordering in Cu_2ZnSnS_4 was needed. To achieve this the approach embodied in the recent Site Occupancy Disorder (SOD) code has been used to study Cu-Zn site disorder, and these calculations are detailed in Chapter 5.

4.5.3 Ion Migration in Cu_2ZnSnS_4

As with the intrinsic defect chemistry, limited prior knowledge of the ion migration properties of Cu_2ZnSnS_4 is available. A greater understanding of these transport properties is needed to be able to improve synthetic processes. Also, it has been noted that completed CZTS-based PV cells can fail after a period of successful operation. It has been postulated that this could be due to Cu out-diffusion (a.k.a. Cu leakage), which allows micro-domains of metallic Cu to form in devices following prolonged operation. These metallic Cu micro-domains are thought to be dendritic in nature and lead to device failure due to creation of a short circuit. This effect is similar to the electrical potential driven migration and accumulation of Cu ob-

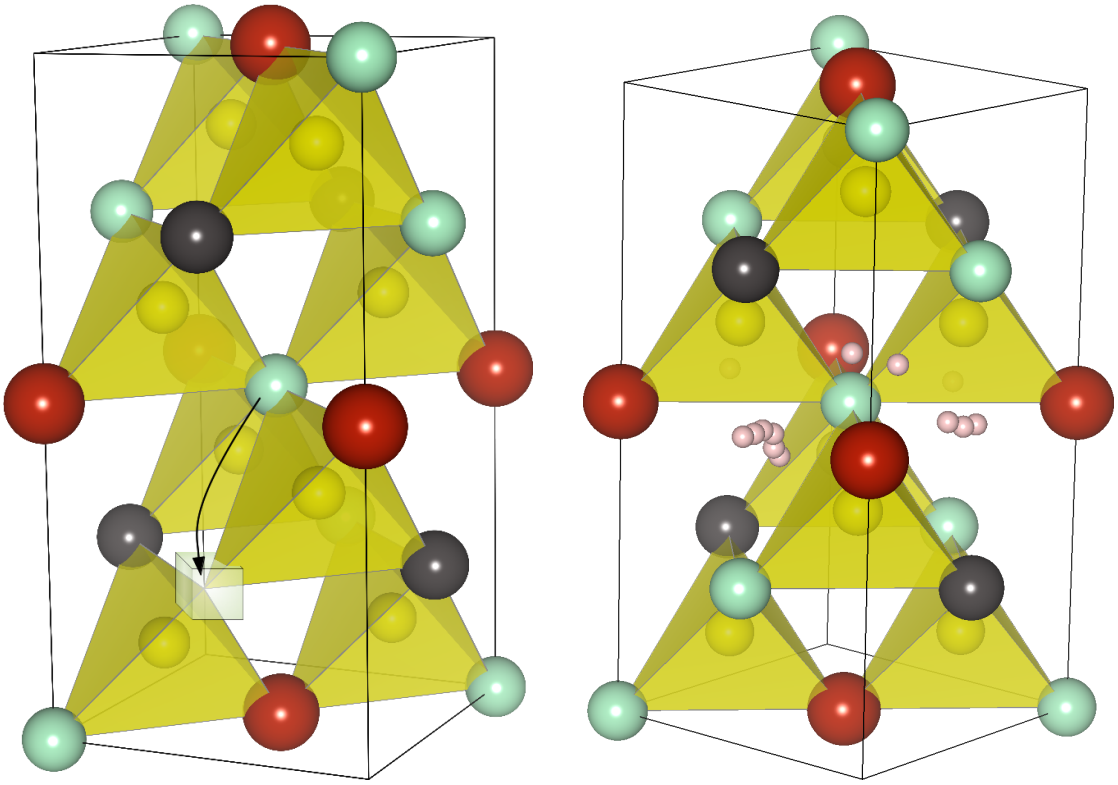

(a) (b)

Figure 4.4: Schematic representation of interlayer V'_{Cu} migration in kesterite (a) and illustration of a discontinuous migration path encountered using a constrained minimisation approach (b). Colours are similar to previous figures with small pink spheres representing the relaxed positions of a migrating $Cu^{\cdot}_{i}$

served in related $CuInSe_2$-based materials and to the Cu out-diffusion in Cu_2S/CdS heterojunctions[148–150]. It is hoped that a greater understanding of ion migration could inform the validity of this theory, and that mechanistic information gained might be useful in the design of methods to mitigate this process as well as informing the design of synthetic processes.

Initially we used a constrained minimisation approach to plot the route of a migrating Cu ion throughout the lattice. This was performed for both $Cu^{\cdot}_{i}$ and V'_{Cu} migration. Details of the calculated migration barriers to the various diffusion paths are listed in appendix B, Table B.9.

A limitation of the constrained minimisation approach is the problem of applying appropriate levels of constraint to migration paths which are not parallel with a lattice vector. This can mean that continuous migration paths become divergent on relaxation as is illustrated in Figure 4.4b.

Constrained minimisation methods are an effective technique for establishing an

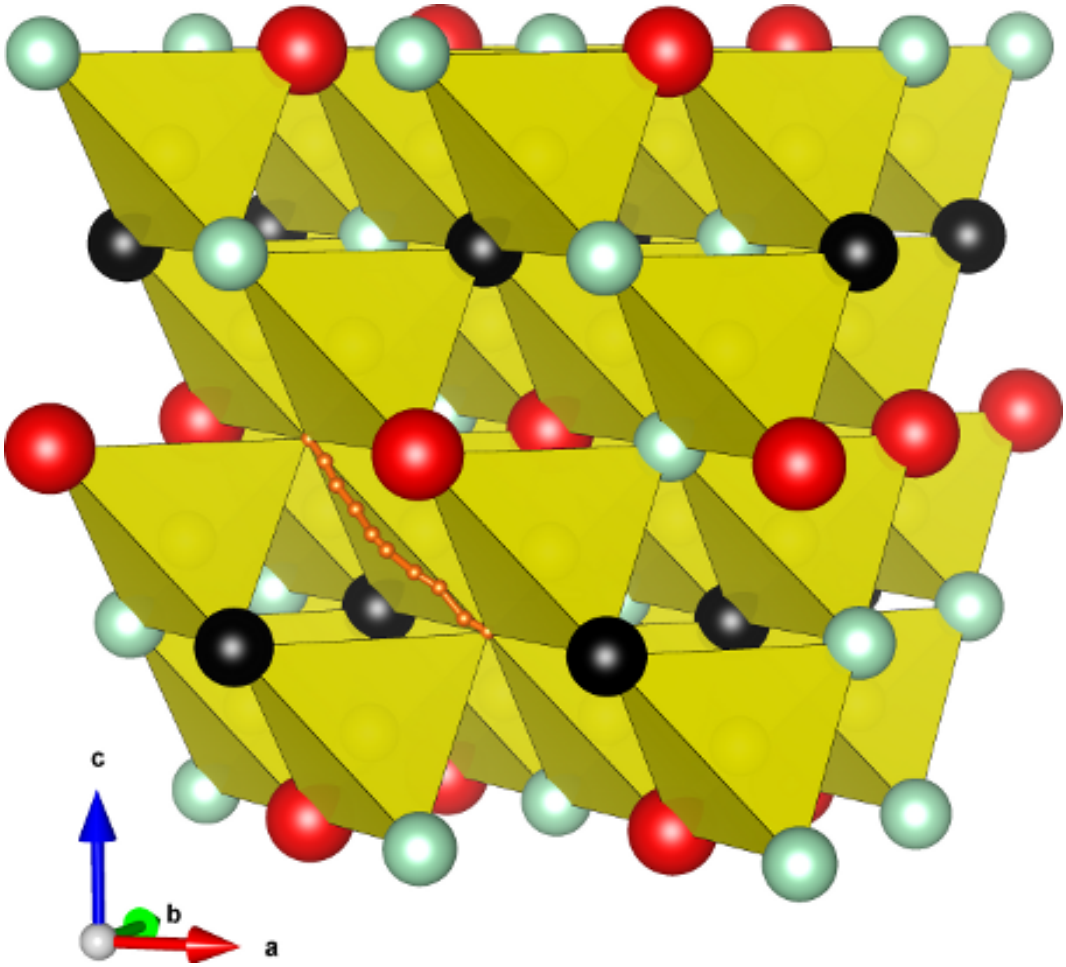

Figure 4.5: Cu diffusion path (small orange spheres) in kesterite Cu_2ZnSnS_4 via a vacancy hopping mechanism

upper-limit for the migration barrier. However, techniques such as the Nudged Elastic Band (NEB) method generally provide a more effective form of transition state search. Thus we have used the NEB method to enhance the constrained minimisation calculations.

Following the publication of work by Chen *et al.*[118, 133] showing that electronic stabilisation of the V'_{Cu} and Cu'_{Zn} defects makes these species favoured over other forms of point defect disorder, such as $Cu^{\cdot}_{i}$, we have focused our calculations on the migration of V'_{Cu} in kesterite Cu_2ZnSnS_4.

Figure 4.5 shows a representation of the path of a migrating Cu ion via a vacancy hopping mechanism. The effect of symmetry means that the path shown in Figure 4.5 is the only way to connect two nearest-neighbour V'_{Cu} sites, and consequently that it is possible to connect individual hops to enable long-range three dimensional V'_{Cu} diffusion in Cu_2ZnSnS_4.

Table 4.9: Calculated energy barriers to copper vacancy (V'_{Cu}) migration

Technique	Energy barrier / eV
Interatomic potentials	0.76
DFT	0.69

We have used the NEB methodology in both the interatomic potentials and DFT formalisms to probe the magnitude of the energy barrier associated with this transition and the results are listed in Table 4.9.

The migration barriers are relatively favourable (≈0.7 eV) and there is good accord between the two calculated values, using both the interatomic potentials and DFT-based methodologies.The magnitude is comparable to migration barriers in oxide-ion conductors.

We have used the calculated energy barriers in Table 4.9 to derive the Cu diffusion coefficient, in line with dilute diffusion theory[151], using:

$$D = g\Gamma a^2, \tag{4.13}$$

where D denotes the diffusion coefficient, g is a geometrical factor (g is assumed to be 1, as is the case in similar modelling work[152]), a the hop-distance and Γ the hopping frequency, which results from transition state theory[153, 154], and is defined as:

$$\Gamma \approx \nu \cdot e^{\left(\frac{-E_a}{k_B T}\right)} \tag{4.14}$$

where E_a is the ion migration energy barrier, k_B the Boltzmann constant, T the absolute temperature and ν is the attempt frequency, for this our calculations use the typical value of $10^{13} s^{-1}$[154].

Using equations 4.13 and 4.14 we calculate the diffusion coefficient for V'_{Cu} migration in Cu_2ZnSnS_4 to be in the $10^{-14} - 10^{-15}$ cm^2s^{-1} range.

Currently, we are unaware of any experimental studies that have investigated ion migration in Cu_2ZnSnS_4/$Cu_2ZnSnSe_4$ materials. However, our calculated diffusion coefficient is consistent with values in the related material $CuInSe_2$, which has been measured by various methods, as detailed in the work of Guillemoles *et al.*[148], and is in the $10^{-13} - 10^{-10}$ cm^2s^{-1} range[148, 155, 156]. The scatter in the measured values has been attributed to the indirect nature of some measurement techniques as well as to the varying quality of the samples.

Based upon our calculated Cu migration barriers and diffusion coefficients we suggest that appreciable Cu diffusion in Cu_2ZnSnS_4-based photovoltaic devices is possible upon sustained operation. This may have several effects upon these devices:

(i) Photo-induced electrical-bias driven Cu-ion migration may lead to a non-uniform distribution of the native defects with respect to film depth in the Cu_2ZnSnS_4 absorber layer, with increased concentrations of V'_{Cu} defects near to the CdS/Cu_2ZnSnS_4 interface and increased Cu-based defects (either Cu'_{Zn} or $Cu^{\cdot}_i$) in the Cu_2ZnSnS_4 bulk.

(ii) We cannot discount the possibility of Cu out-diffusion (a.k.a. Cu-leaching) from Cu_2ZnSnS_4 layers. This is an effect similar to that observed in Cu_2S/CdS-based devices and with the associated device failure, as discussed in section 4.5.3. However, we have not addressed whether there is a driving force for this diffusion. In Cu_2S/CdS heterojunctions the chemical potential of Cu is lower in CuS than in Cu_2S, which drives the out-diffusion. However, in $CuInSe_2$ this is not the case and Cu out-diffusion is not a significant problem.

Cu mobility in Cu_2ZnSnS_4 means that a non-uniform distribution of defects is possible. This non-uniform distribution could mitigate the effects of out-diffusion as the enhanced concentration of V'_{Cu} near the Cu_2ZnSnS_4/CdS interface could act as a "sink" for Cu ions, as is the case in $CuInSe_2$[148].

(iii) The moderate mobility of Cu may in fact act to preserve the cell, by enabling "auto-repair" processes akin to those proposed in CIGS devices[148]. The mobility of Cu means that devices exist in a buffered equilibrium and that the effects of perturbing forces such as bias-driven ion migration or structural irradiation damage are mitigated by the flexibility of the material, with structures able to equilibrate during perturbation-free conditions (most notably darkness). This is an area that warrants further investigation.

4.6 Chapter Summary

This chapter describes computational studies of the structural, defect and Cu migration properties of Cu_2ZnSnS_4 which can be summarised as follows.

1. We have successfully derived interatomic potentials for Cu_2ZnSnS_4, which describe the structure of both kesterite and stannite polymorphs accurately.

2. The development of our potential model has allowed investigation of a wide range of intrinsic defects in Cu_2ZnSnS_4 for the first time. We find that the Cu/Zn antisite defects are the lowest energy intrinsic disorder in both kesterite and stannite. We also find that the energy of the Cu Frenkel is low enough to account for the increased Cu mobility during certain synthetic processes which occur at elevated temperature. However, we note that the formation energies of all other Frenkel/Schottky defects are high and preclude the formation of these

defects in appreciable concentrations. We note that the formation energies of the defects investigated vary little between the two polymorphs.

3. For the Cu/Zn antisite defects in kesterite Cu_2ZnSnS_4 we find that there is an energetic preference for small neutral defect clusters. This suggests that a degree of self-passivation behaviour exists in Cu_2ZnSnS_4 which is important as this should limit charge-carrier trapping and consequent recombination.

4. We have also investigated the Cu transport properties of kesterite Cu_2ZnSnS_4. We find that there is only one possible symmetry inequivalent hop for a copper vacancy (V'_{Cu}), and that it is possible to connect such hops to enable long-range three-dimensional V'_{Cu} diffusion. We have used a Nudged Elastic Band method in both the interatomic potential and DFT formalisms to calculate the energy barrier associated with this Cu vacancy hop, and find it to be 0.76 eV and 0.69 eV respectively.

   The Cu diffusion coefficient that is derived is in the order of $10^{-14} - 10^{-15}$ cm^2s^{-1}. Based upon this we suggest that Cu diffusion will be slower in Cu_2ZnSnS_4 than in $CuInSe_2$, although when the effect of bias-driven migration is considered it is thought that Cu migration will still impact greatly upon the photovoltaic behaviour of Cu_2ZnSnS_4. We believe that Cu mobility may lead to bias-driven non-uniform defect distributions, and that we cannot discount the possibility of Cu out-diffusion. However, further work to establish whether a driving force for this process exists is needed.

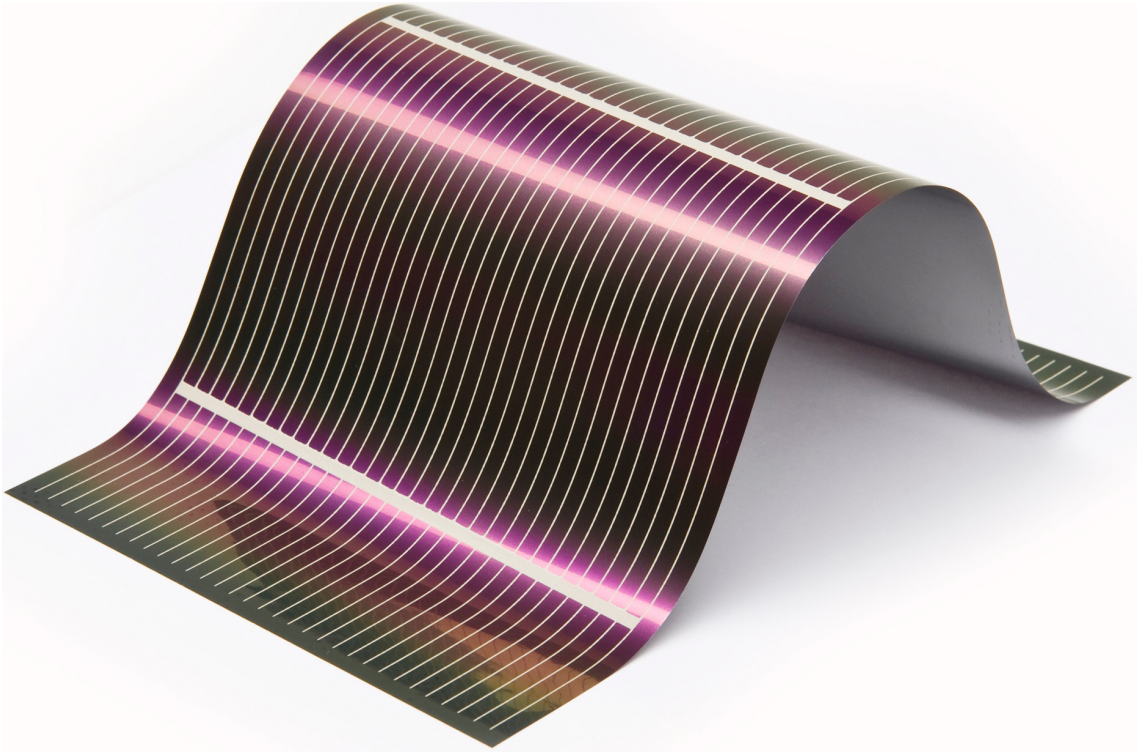

(a)

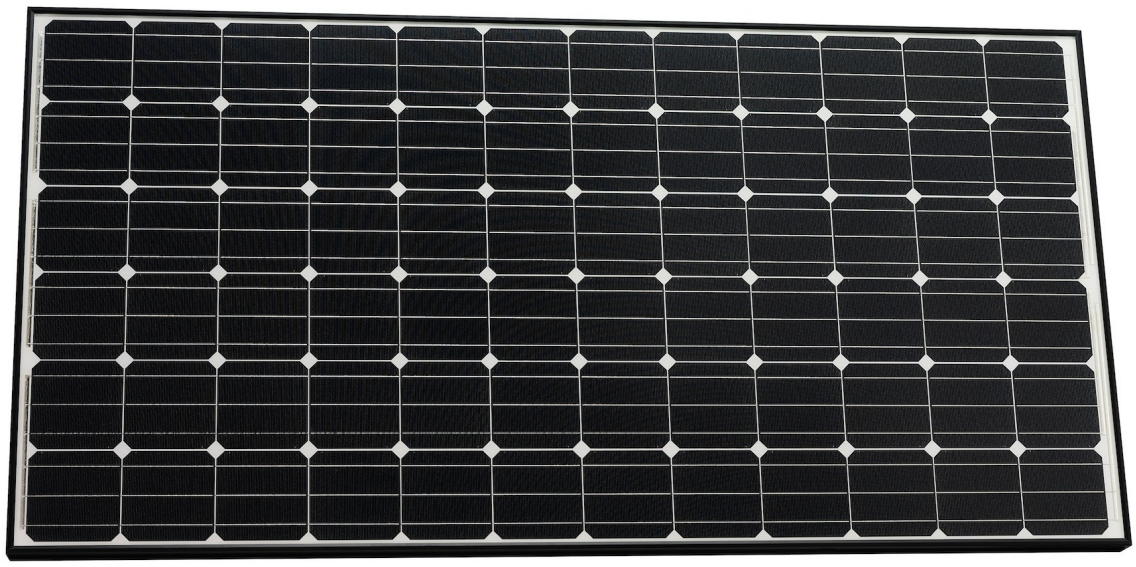

(b)

Thin-film photovoltaic modules using a non-planar substrate (a) and in the conventional flat (b) configurations.

Chapter 5

Polymorphism and Surface Properties of Cu_2ZnSnS_4

5.1 Introduction

As has been introduced in chapters 1 and 4, Cu_2ZnSnS_4 is the most promising of a range of materials which are currently under investigation for their potential utility in the absorber layers of next-generation thin-film photovoltaic cells. This is principally because Cu_2ZnSnS_4 possesses a near-optimum band gap for terrestrial energy generation, as well as a high optical absorption coefficient[45–48]. Furthermore, Cu_2ZnSnS_4 is composed solely of elements which are relatively inexpensive and abundant, thus making the material a suitable candidate for use in large scale photovoltaic device production.

In the preceding chapter, we used a potentials-based approach to investigate the structural, defect and ion-migration properties of Cu_2ZnSnS_4. In this chapter, we have used Density Functional Theory (DFT) based techniques to investigate the issue of polymorphism, and potential based methods to study, for the first time, the surface structures of Cu_2ZnSnS_4.

5.2 Simulation Methods

It should be noted that a more detailed discussion of the techniques which underpin this section has been given in chapter 2.

For the investigation of polymorphism in Cu_2ZnSnS_4, we have used the approach embodied in the Site Occupancy Disorder (SOD) code[62]. In this approach the complete configurational space describing all possible ordering configurations, for a given supercell of material, is generated. From this the symmetry-inequivalent configurations are selected, using the symmetry operators of the parent structure. Using

either DFT, as in our investigations, or interatomic potential based energy minimisation methods, to provide the relative formation energies of the configurations in this reduced set, we can assess the occurance of each configuration in the disordered solid according to a Boltzmann-like probability. This allows the prediction of certain material properties, such as lattice parameters for the disordered solid, as well as allowing the effect of temperature on the configurational composition to be considered.

The DFT calculations have been performed utilising a planewave code, the Vienna *Ab initio* Simulation Package (VASP). For the exchange-correlation potential, we have used the semi-local Generalised Gradient Approximation (GGA) functional of Perdew, Burke and Ernzerhof[82], in conjunction with the PAW method. A planewave energy cut-off of 280 eV was used. For sampling of the Brillouin-zone a $4 \times 4 \times 4$ Monkhorst-Pack mesh of *k-points* was used for the $2 \times 2 \times 1$ supercells of Cu_2ZnSnS_4, where $a \approx b \approx c \approx 10.8$Å, while for smaller supercells the *k-point* mesh was scaled accordingly. In the simulations, all lattice vectors and ionic positions were fully relaxed. An ionic force tolerance of 1×10^{-3} eVÅ^{-1} in each lattice direction was used throughout.

5.3 Results and Discussion

5.3.1 Structural Modelling: Polymorphism and Site Occupancy Disorder

Cu_2ZnSnS_4 is a complex material which is difficult to synthesise, and in recent years there has been considerable confusion as to the exact nature of numerous synthesised samples. It is known that Cu_2ZnSnS_4 has a variety of polymorphs, due to the large number of possible cation ordering schemes resulting from the multi-ionic nature of the material[104, 157, 158]. It is widely accepted that kesterite Cu_2ZnSnS_4 represents the lowest energy of these cation ordering schemes, and that stannite Cu_2ZnSnS_4 is only slightly less energetically favourable. In this work, as is the case in the published literature, these two polymorphs receive the most consideration. However, it is clear that these two configurations do not completely describe the plethora of cation ordering permutations which are possible for Cu_2ZnSnS_4. There have been previous attempts to address this, notably the work of Chen[104] and Ichimura[157]. However, in both these studies the number of polymorphs considered is rather small, 3 and 5 respectively, when compared with the number of configurations possible. Furthermore, neither work considers entropic contributions to the prevalence of a particular polymorph.

We have used the Site Occupancy Disorder code of Grau-Crespo and co-workers[62] in conjunction with VASP, to study the favourability and prevalence of a range of Cu_2ZnSnS_4 polymorphs, which result from disorder in the Cu/Zn sublattice over a

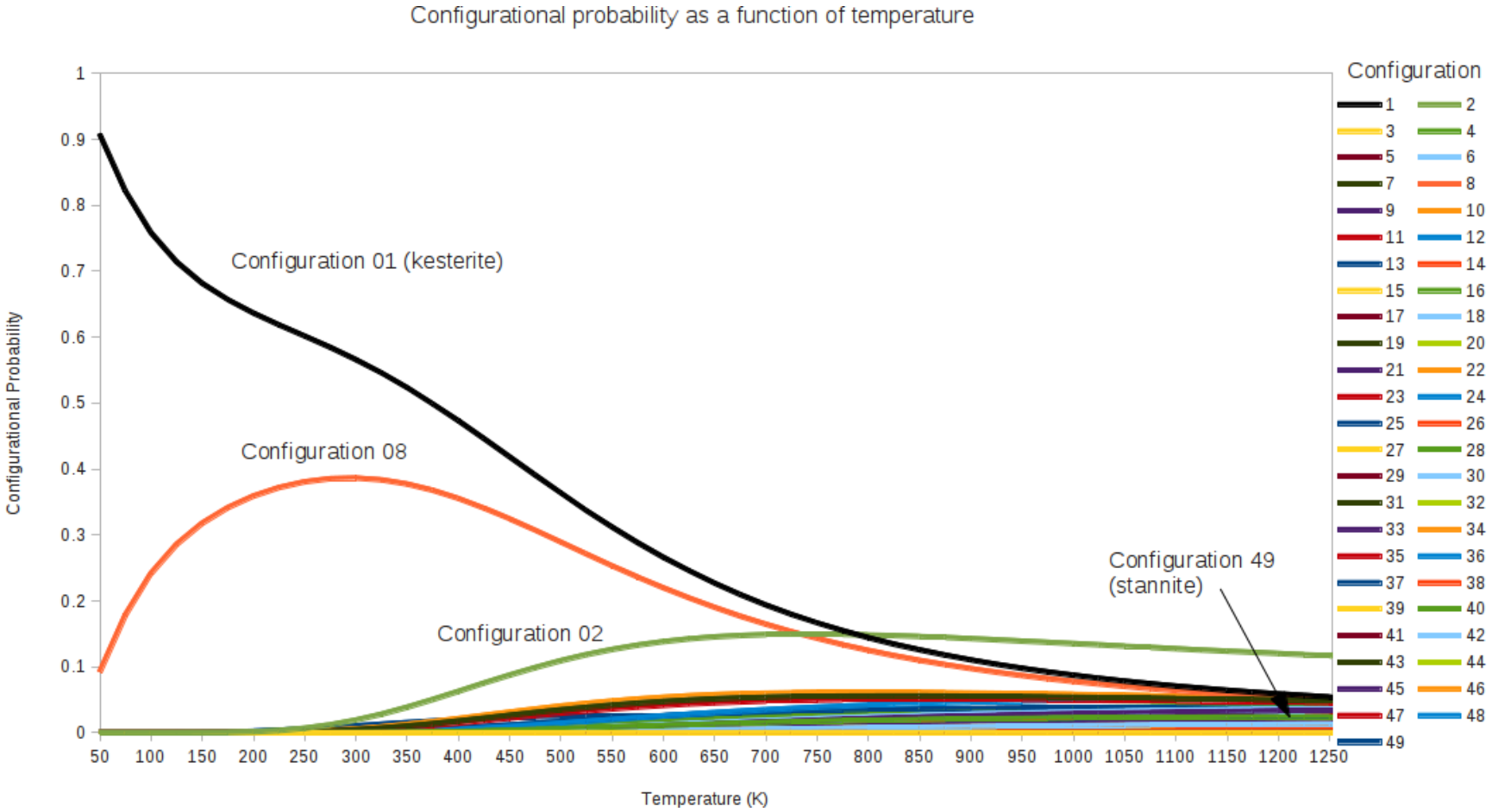

Figure 5.1: Calculated configurational probability for the 49 symmetry-inequivalent Cu/Zn ordering schemes in CZTS, as a function of temperature. The structures of the configurations are shown in Appendix C. The polymorphs kesterite and stannite correspond to configurations 01 and 49 respectively.

range of temperatures.

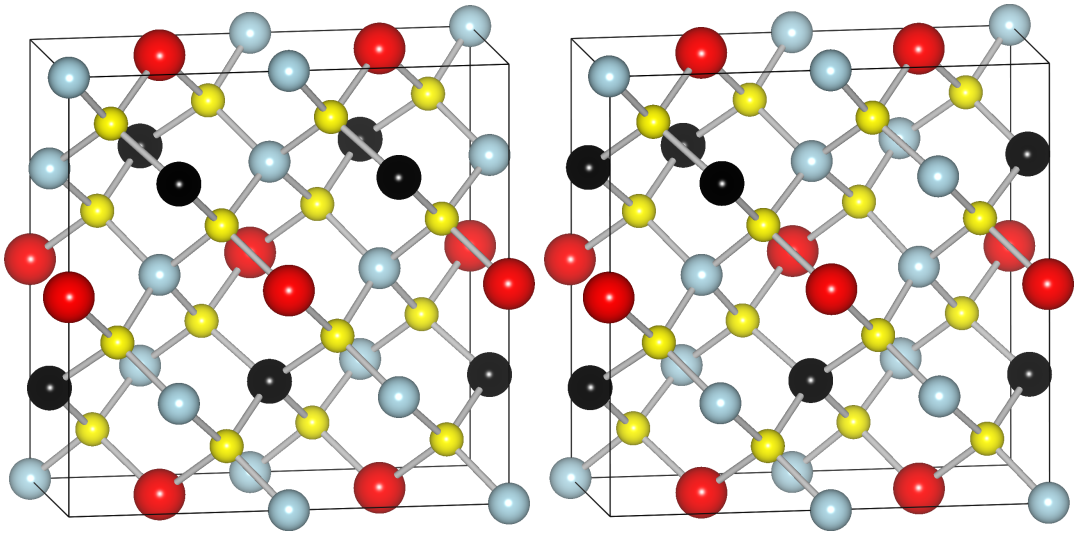

(a) Config 01

(b) Config 02

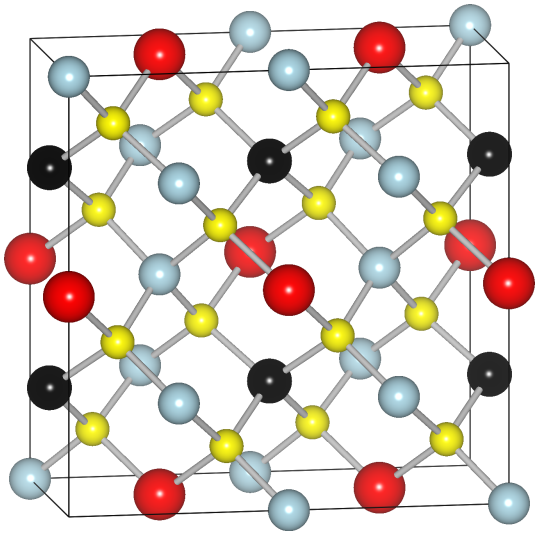

(c) Config 08

Figure 5.2: The structures of Cu_2ZnSnS_4 configurations 01 (kesterite), 02 and 08. Colours are similar to previous figures; where S (yellow), Sn (red), Zn (black) and Cu (green).

We examined the 49 symmetry-inequivalent configurations which arise as a result of varying the positions of all the Cu and Zn ions among the Cu/Zn sites in a $2 \times 1 \times 1$ supercell. Investigation of larger supercells and of disorder in the Sn sub-lattice was also considered. However, the number of configurations rapidly becomes intractable if too many variables are introduced; for example considering the Cu/Zn sublattice disorder in a $2 \times 2 \times 1$ supercell results in 24237 symmetry-inequivalent configurations rather than 49 for a $2 \times 1 \times 1$ supercell.

Figure 5.1 shows the configurational-probability (as defined in section 2.4) for each

of the 49 symmetry-inequivalent configurations in the temperature range 50-1250K. Above this range Cu_2ZnSnS_4 decomposes. The configurational-probability takes into account not only the formation energy for a given configuration but the degeneracy of that configuration, as discussed in chapter 2. This approach is superior to simply considering the formation energies for a given set of polymorphs, as entropic considerations are included.

Figure 5.1 indicates that the prevalence of a given configuration is highly temperature dependent. At temperatures below 800K perfectly ordered kesterite (configuration 01) dominates. However, it is only at temperatures below 300K that we predict it to account for the majority of a sample. Generally, synthesis of Cu_2ZnSnS_4 takes place at elevated temperatures. In the most efficient Cu_2ZnSnS_4 based devices the material is annealed at 813K. At these temperatures configuration 01 is no longer the dominant phase. Instead we predict that configurations 01, 02 and 08 (shown in Figure 5.2) account for ≈40% of a sample, and that the remainder is accounted for by other configurations. As a result, we suggest that the rate at which samples are cooled after annealing will have a significant impact on the cation ordering of the material, with samples which are quench-cooled exhibiting a more disordered Cu/Zn sublattice. Slow-cooled samples will be more "kesterite-like", as they will contain a higher proportion of the perfectly ordered kesterite configuration (Config 01). However, at 300K the configurational-probability for Config 01 is ≈56%, which suggests that the formation of phase pure kesterite may not be possible.

Inspecting the structures of the configurations that are predicted to be the most prevalent; 01, 02 and 08 (which are shown in figure 5.2), it is found that the deviations are restricted to the distribution of ions in the Cu/Zn layer at $z = \frac{3}{4}$. This can help to rationalise the observations of the experimental groups of Bonazzi[141] and Schorr[159], who find their samples of kesterite to be partially disordered and lacking order in the Cu/Zn layers at $z = \frac{1}{4}$ and $\frac{3}{4}$, which is in clear agreement with our calculated results.

Now turning to consider the stannite polymorph (configuration 49), there are a few reports of Cu_2ZnSnS_4 films with the stannite structure[46, 127]. However, when consulting figure 5.1 it is clear that the configurational-probability of stannite formation is low throughout the entire temperature range, and that formation of stannite is not preferred. Indeed it is difficult to distinguish the corresponding trend-line as there are a raft of alternative configurations with comparable formation probabilities. To address this issue, Figure 5.3 shows the probability of only stannite formation as well as the Zn occupancy of the Cu/Zn cation sites in the $z = 0$ and $z = \frac{1}{2}$ layers, as a function of temperature. We find that the maximal calculated configurational-probability of stannite is 0.0256 (550-575K), suggesting that samples annealed in this temperature range and then rapidly/quench-cooled would be composed of ≈2.5% stannite. Hence, our calculations do not predict stannite to be the dominant polymorph at any temperature, and therefore suggest that characterising Cu_2ZnSnS_4 films as stannite-type on the basis of XRD data may be unwarranted.

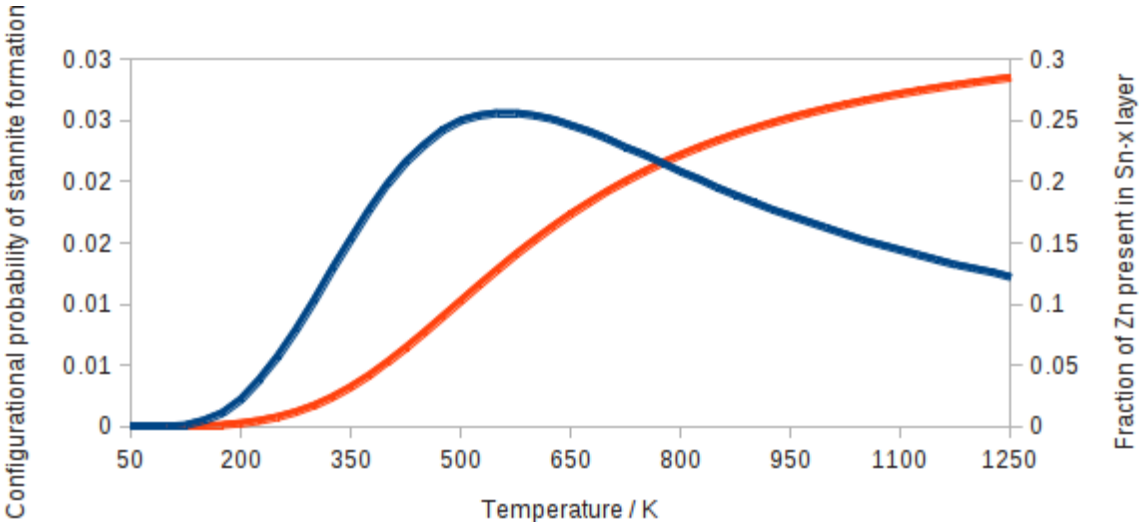

Figure 5.3: Calculated configurational probability for stannite (blue - primary axis), and the fraction of Zn located in the M-Sn layer (red - secondary axis), each as a function of temperature.

It should be reiterated that XRD studies cannot distinguish the isoelectronic Cu^{+} and Zn^{2+}, and so it is difficult to distinguish polymorphs of Cu_2ZnSnS_4 which are distinct due to the ordering of the Cu/Zn sublattice.

Figure 5.3 also shows the Zn occupancy of the Cu/Zn site in the Sn-x layers. We find that the maximal Zn occupancy of these sites, prior to material decomposition, is ≈29%, and that over the range of temperatures common in synthesis the Zn occupancy is 20-25%.This result supports the previous point regarding the unfavourability of stannite polymorph formation, and suggests that kesterite (and kesterite-type) configurations represent the majority of a Cu_2ZnSnS_4 sample irrespective of synthesis temperature.

5.3.2 Structural Properties and Tetragonal Distortion

As well as predicting the temperature dependence of the configurational composition (as is shown in Figure 5.1), we can predict average properties, such as lattice parameters, based upon the configurational composition of Cu_2ZnSnS_4 at different temperatures. Figure 5.4 shows the lattice parameters a, b and c as a function of temperature (note that this does not include the effect of thermal expansion and is more representative of the properties of samples which have been synthesised at a given temperature, and then quench cooled). We find that all the lattice parameters increase with temperature induce configurational change in Cu_2ZnSnS_4. However, while the increases in the a and b parameters are relatively small, being ≈0.002Å over the 1150° temperature range, the change in the c parameter is more noticeable as it is 0.008Å1mm (0.07%). As a result we have investigated whether the tetragonal

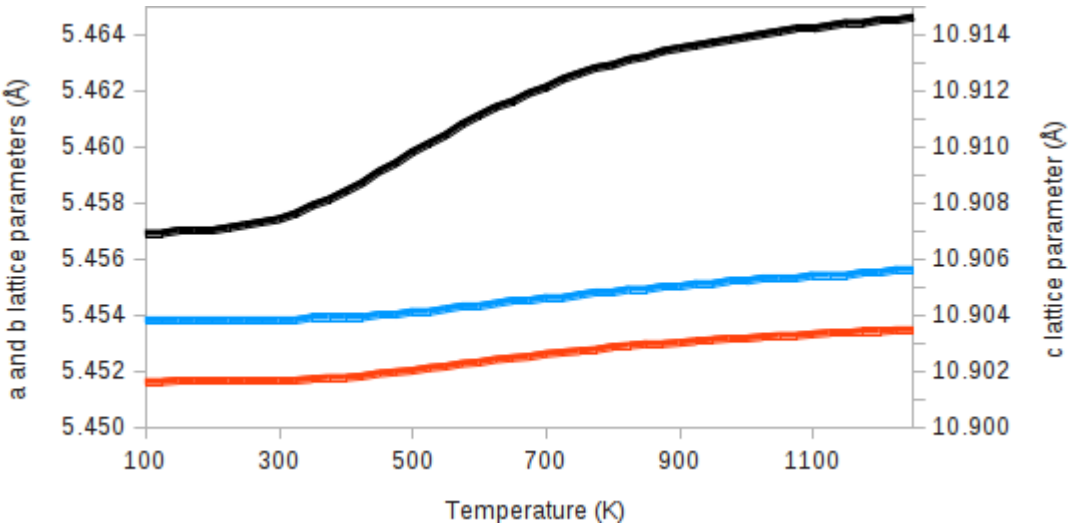

Figure 5.4: Calculated lattice parameters a (red), b (blue) and c (black) in Cu_2ZnSnS_4, as a function of temperature. The parameters a and b are relative to the primary axis and c is relative to the secondary axis.

distortion, which is a measure of the deviation of the unit cell from perfect tetragonal symmetry given by the ratio of the lattice parameters $\left(\frac{c}{2a}\right)$, is significantly affected by these changes.

The tetragonal distortion is an important property in semiconductors composed of tetrahedral networks, such as the chalcopyrites and kesterites, as deviation from perfect tetragonal symmetry affects the crystal field splitting of the orbitals comprising the valence band[134]. This indicates that tetragonal distortions lead to a non-degenerate valence band maximum[161]. The sign of the crystal field affects the symmetry of the valence band[161–163], which alters the anisotropy of the effective mass[164]. Hence, we have investigated whether the changes in configurational composition driven by synthesis temperature systematically affect the tetragonal distortion in Cu_2ZnSnS_4. We have plotted the tetragonal distortion as a function of temperature (Figure 5.5), based upon the data illustrated in Figure 5.4.

It should be noted that, because the lattice parameters are proportional averages of the parameters from a set of distinct configurations, the lattice parameter a is not equal to b. Consequently in Figure 5.5 we show data corresponding to the measurements of tetragonal distortions described by $\left(\frac{c}{2a}\right)$, $\left(\frac{c}{2b}\right)$ and $\left(\frac{c}{ab}\right)$. As well as this data, Figure 5.5 also shows the tetragonal distortions present in a selection of data from experimental studies[134, 141, 158, 160], where sufficient information about the cooling of the samples was provided. These are shown at 293K, because the slow cooling rate means that the cation configuration will have time to adjust to that most favoured at this temperature. The composition of the quench-cooled samples will remain that of the annealing temperature.

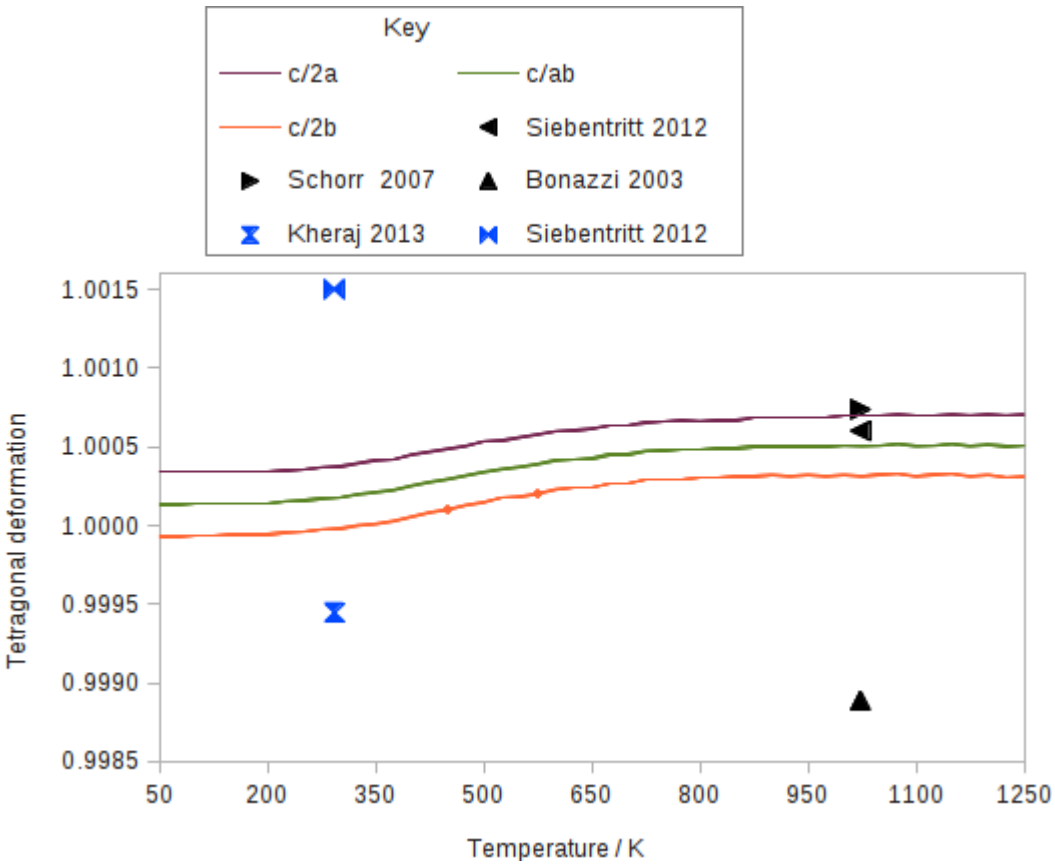

Figure 5.5: The tetragonal distortion $\left(\frac{c}{2a}\right)$ as a function of temperature. The tetragonal distortion of samples from the experimental work of Siebentritt[134], Schorr[158], Bonazzi[141] and Kheraj[160] are also shown. Samples which have been quench-cooled are denoted by a black marker, samples with a slower cooling rate are denoted by blue markers.

From the data presented in Figure 5.5, we find that there is a correlation between our predicted tetragonal distortion and temperature. Higher temperatures lead to larger distortions, although the magnitude of the change is rather small when compared to the spread of the experimental data ($\Delta = 0.5 \times 10^{-3}$ and 2.6×10^{-3} for the calculated and experimental distortions respectively). We also find that for temperatures of 300K and higher, the predicted tetragonal distortion is ≥ 1. Our calculated distortion appears to be in good agreement with that found in the samples prepared by Siebentritt[134] and Schorr[158]. However, there is a discrepancy with the work of Bonazzi[141] who found the tetragonal distortion to be significantly lower than 1.0. While all of these experimental groups quench-cooled their samples from an annealing temperature of 750°C (1023K), the samples of Siebentritt and Schorr were polycrystalline powders, whereas Bonazzi produced a single-crystal.

Relating the fact that our calculated tetragonal distortions are ≥ 1 above 300K to the finding by Siebentritt that thin-films of Cu_2ZnSnS_4 generally have tetragonal

distortions ≤ 1 (not shown in Figure 5.5 as information about the cooling rates of the thin-film samples were omitted from their paper). We support the suggestion that this is a result of the stress inherent in the prepared films, as we cannot rationalise the discrepancy in terms of distortions induced by the configurational composition of the sample.

We conclude that while there is a correlation between annealing temperature and tetragonal distortion in quench-cooled powder samples, the effect is rather small and its impact is obscured by other effects such as strain and sample composition. As our calculations predict tetragonal distortions ≥ 1 above 300K, our data does not predict a reversal in the sign of the crystal field splitting in this range. Consequently, we suggest that parameters other than the configurational composition will determine the anisotropy of the effective mass.

5.3.3 Surface Properties of Cu_2ZnSnS_4

A key component of materials' performance in electrochemical devices, such as photovoltaics, Li-ion batteries and fuel cells, is the surface and interface properties which they contribute to a device. These properties are dependent on the surface structures which are exhibited by a material. Therefore, developing our knowledge of these features on the atomic-scale is important for understanding the key mechanisms that determine a device's functionality.

Currently, the surface properties of Cu_2ZnSnS_4 are not fully characterised. This is in part due to the complexity of the material system, the variety of synthetic methods used and because it is difficult to identify distinct surface planes solely using experimental techniques. Nonetheless, it is widely thought that the surface-related properties exert a significant influence over the material's applicability as a photovoltaic absorber material. Studies of $CuInSe_2$-based photovoltaic devices have found that charge carrier recombination often occurs at surfaces and grain boundaries[165–171]. Given the similarities between Cu_2ZnSnS_4 and $CuInSe_2$, it is thought that similar effects may be present at the surfaces of Cu_2ZnSnS_4. Before this potential loss mechanism can be investigated, and potentially mitigated, it is necessary to improve the basic understanding of the surface structures of Cu_2ZnSnS_4. In this section we use potential based methods to investigate the low energy surfaces, and their atomic-scale structure. This will enable future investigation of the Cu_2ZnSnS_4/CdS interface, as well as enabling the investigation of surface-based charge carrier recombination.

We have used the METADISE (Minimum Energy Techniques Applied to Dislocation Interface and Surface Energies) code of Watson *et al.*[172], the underlying methodology of which is discussed in chapter 2. We have investigated the surface energies for a wide range of low index surfaces, a full list of these is given in the appendix (Table D.1).

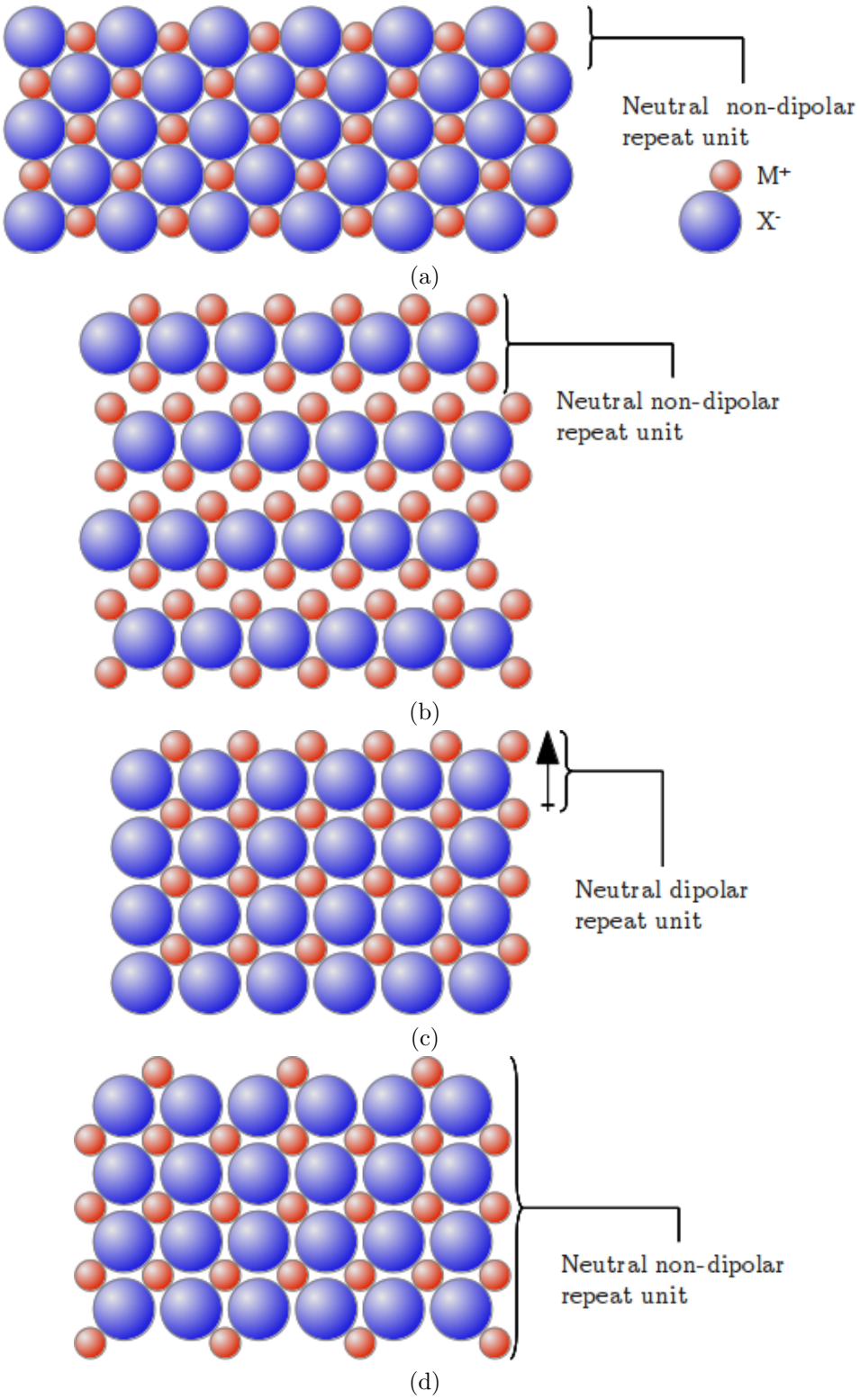

Figure 5.6: Schematic of the surface types defined by Tasker, showing a type I surface (a), a type II surface (b) and a type III surfaces before (c) and after (d) reconstruction.

It is common to describe the surfaces of polar solids according to the classifications introduced by Tasker[173], who defined three types of surface as follows:

- **Type I** Surfaces which are composed of stoichiometric layers, and have no dipole perpendicular to the surface. (Figure 5.6a)
- **Type II** Surfaces composed of multi-layer repeat units which do not have a dipole perpendicular to the surface. (Figure 5.6b)
- **Type III** Surfaces where it is not possible to cleave the layers to give a non-dipolar surface (Figure 5.6c). For these surfaces to exist the dipole must be removed, which can be achieved either by surface reconstruction (Figure 5.6d) or by oxidation/reduction of surface ions.

Illustrations of these surfaces and the reconstruction of type III surfaces in order to remove the dipole are shown in Figure 5.6, which is based on the work of Parker *et al.*[174].

The vast majority of the investigated surfaces in kesterite Cu_2ZnSnS_4 are type III, as they exhibit a net dipole when cleaved. It is clear that surface reconstruction is of critical importance in quaternary chalcogenide materials, as for some surfaces reconstruction eliminates the net dipole. Also, we find that relaxation of the surface significantly affects the surface energy for all of the investigated surfaces. For the stable surfaces, the reduction in surface energy upon relaxation is in the 75-97% range, resulting in increased stability of the terminating layers. We also find that relaxation can change the relative favourability of a set of surfaces. These findings demonstrate the importance of accounting for surface reconstruction/relaxation, and that the relative surface energies of the Cu_2ZnSnS_4 surfaces cannot be reliably predicted by assuming them to be rigid terminations of the bulk crystal lattice.

However, the presence of a net dipole in the vast majority of Cu_2ZnSnS_4 surfaces meant that in most of the studied cases, relaxation of the surface led to a divergent surface energy. Consequently, the number of surface planes with low relaxed surface energies is rather small. Table 5.1 lists the calculated surface energies for the most favourable surface cuts. We recognise that the surface energy for (101) is unusually low, which needs further investigation. Nevertheless, these atomistic simulations of Cu_2ZnSnS_4 surfaces are the first of their type and are useful preliminary studies to future work in this area. Turning to examine the structures of the low energy surfaces listed in Table 5.1, we find that for the (1 1 2) surface, the relaxed surface differs significantly from the as-cleaved surface (shown in Figure 5.10), which exposes a plane of Cu and Zn ions and is largely smooth. This is in stark contrast to the relaxed surface (shown in Figure 5.7), which is dominated by pairs of two-coordinate bridging S ions, that form Cu-S-Cu-S-Zn moieties (see the centre of Figure 5.7a). The bridging units are distorted, with the Zn-S-Cu angle being 100.58° and the Cu-S-Cu angle being 119.46°. Consequently, the S from the Zn-S-Cu unit projects further from the surface than the S of the Cu-S-Cu unit. Together, these projecting S ions form an uneven ridge aligned with the b direction and leave the terminal Cu

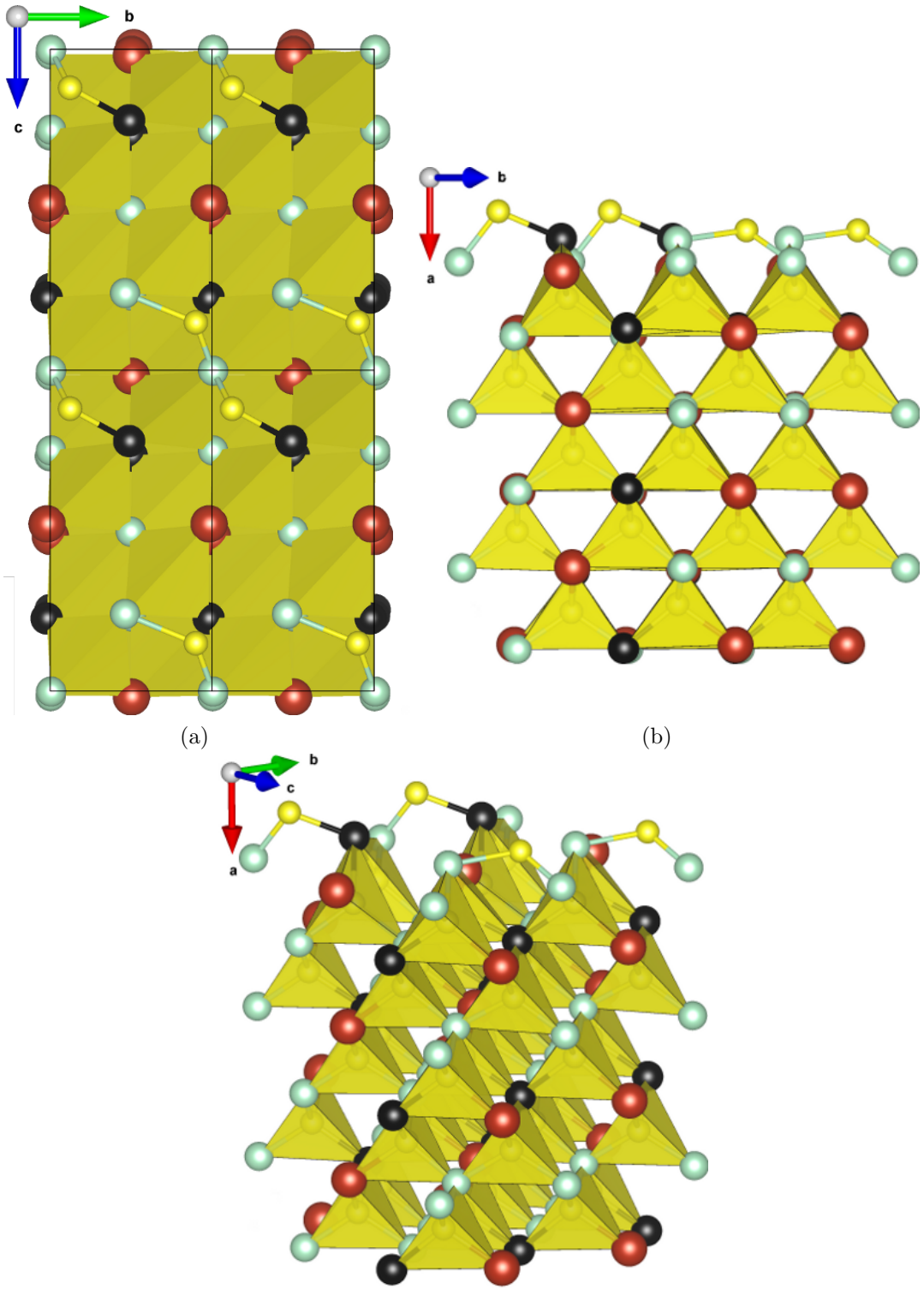

(a) (b)

(c)

Figure 5.7: Relaxed Structure of a 2×2 supercell slab of the (1 1 2) surface, shown from a top-down (a), side-on (b) and diagonal (c) perspective. Colours are similar to previous figures: Cu (green), Zn (black), Sn (red) and S (yellow).

Table 5.1: Relaxed and unrelaxed surface energies ($E_{surface}$) for the lowest energy cuts for kesterite Cu_2ZnSnS_4.

Miller index	Unrelaxed $E_{surface}$ / Jm^{-2}	Relaxed $E_{surface}$ / Jm^{-2}
(-1 0 1), (1 0 1), (0 1 -1), (0 -1 -1)	2.81	0.09
(1 0 0), (0 1 0),	4.85	1.27
(1 1 2)	4.74	1.27

and Zn three-coordinate. Between these ridges of exposed S there are two-coordinate Sn ions which are recessed from the surface and give rise to a trough, again parallel to the *b* direction. These surface features mean that the topology of the relaxed (1 1 2) surface is relatively uneven.

The (0 1 0) surface (shown in Figure 5.8) is comparatively smooth. The principal features are the zig-zag rows of exposed under-coordinated Cu which run along the surface in the (0 1 1) direction (see Figure 5.8c). These are arranged about an under-coordinated Zn which is recessed into the surface. Sn is removed from the surface by reconstruction. The tetrahedra in the uppermost layer are severely distorted as a result of the topmost cations (Cu and Zn) relaxing inwards towards the bulk. This can be seen clearly in the Cu-S-Zn angle which increases to 129.84° as a result.

The (1 0 1) surface exhibits a grooved uneven topology much like the (1 1 2) surface. However, in the (1 0 1) surface the ridges are topped by two-coordinate Zn which are aligned along the (0 1 1) direction of the surface (see Figure 5.9b). These are flanked by under-coordinated and exposed Cu on one face and S on the other. Like the (0 1 0) surface, Sn is removed from the surface layer by reconstruction.

Recently, the results of numerous investigations which have synthesised and characterised Cu_2ZnSnS_4 thin-films have been published[175–183]. It is found that due to the use of a variety of synthetic techniques and the challenges associated with synthesising a complex quaternary system (in which formation of secondary phases is likely), the quality of the Cu_2ZnSnS_4 thin-film samples varies greatly. However, there seems to be a consensus that in synthetic routes which involve sulphurisation, higher annealing temperatures generally lead to improved film quality.

In studies where the orientation of the film is reported, the majority of cases find samples to be oriented with the (1 1 2) plane[176, 177, 179, 184–186]. This finding appears to be in good agreement with our calculations as the (1 1 2) plane is one of the few surfaces which is able to reconstruct in order to eliminate the "as cleaved" dipole, whilst retaining a low surface energy. However, the work of Shi *et al.*[186] finds that in addition to alignment along the (1 1 2) direction, alignment with the (2 2 0) and (3 1 2) planes is also observed. Additionally, the work of Shinde and co-workers[187] which prepares Cu_2ZnSnS_4 through a novel layer by layer additive process, reports their samples to be aligned with the (0 0 2), (1 1 0) and (2 0 0)

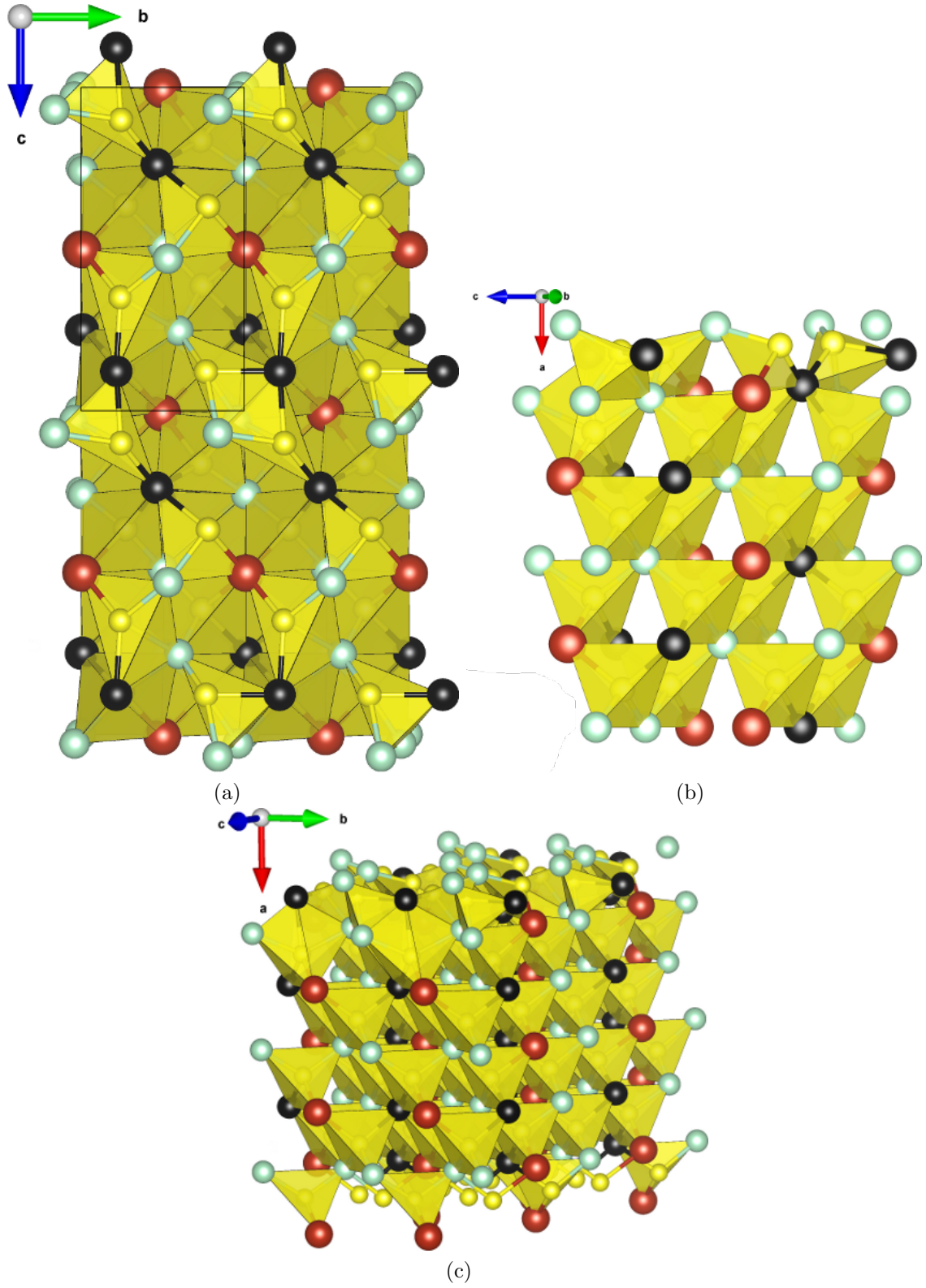

Figure 5.8: Relaxed Structure of the (0 1 0) surface shown from a top-down (a), side-on (b) and diagonal (c) perspective.

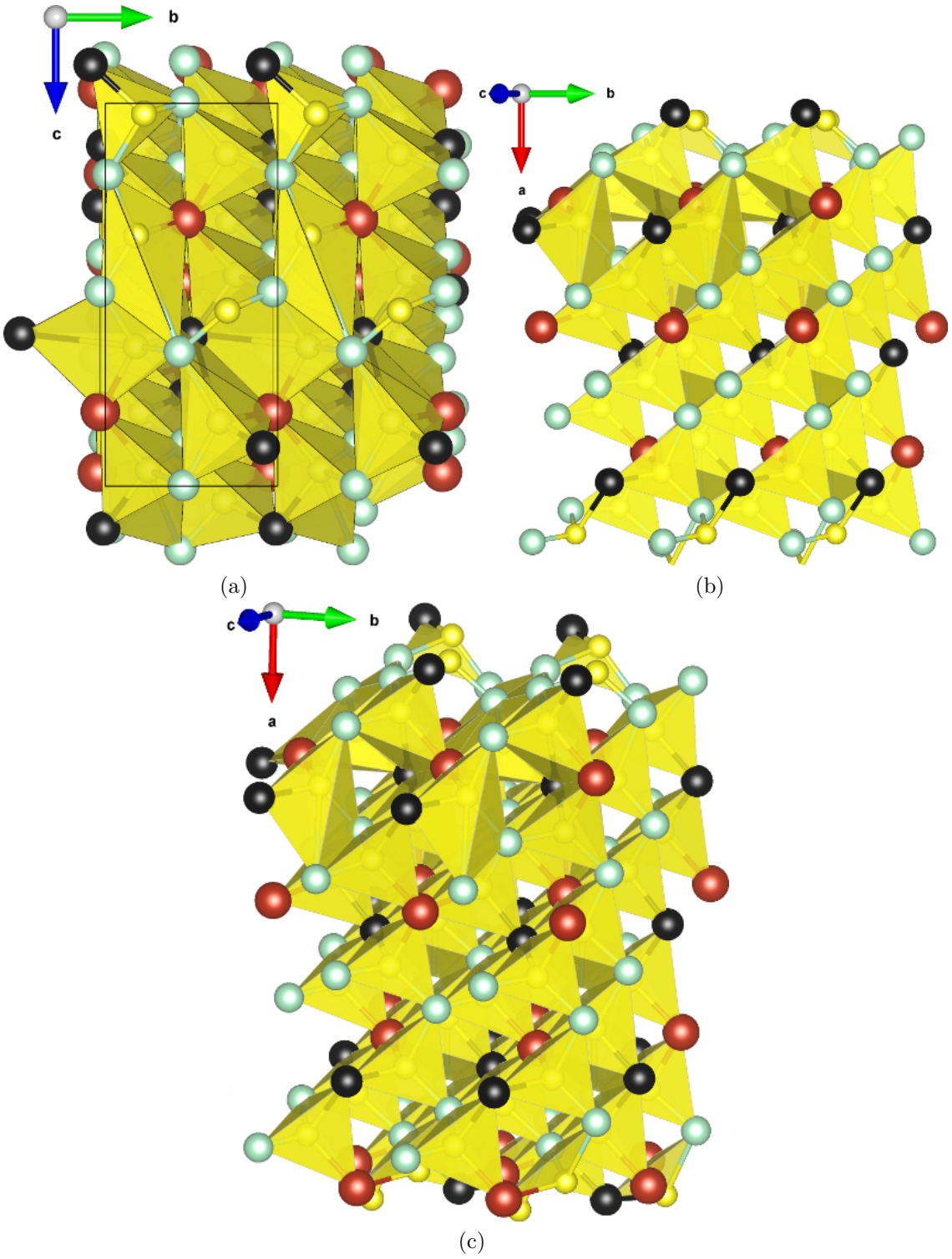

Figure 5.9: Relaxed Structure of the (1 0 1) surface shown from a top-down (a), side-on (b) and diagonal (c) perspective.

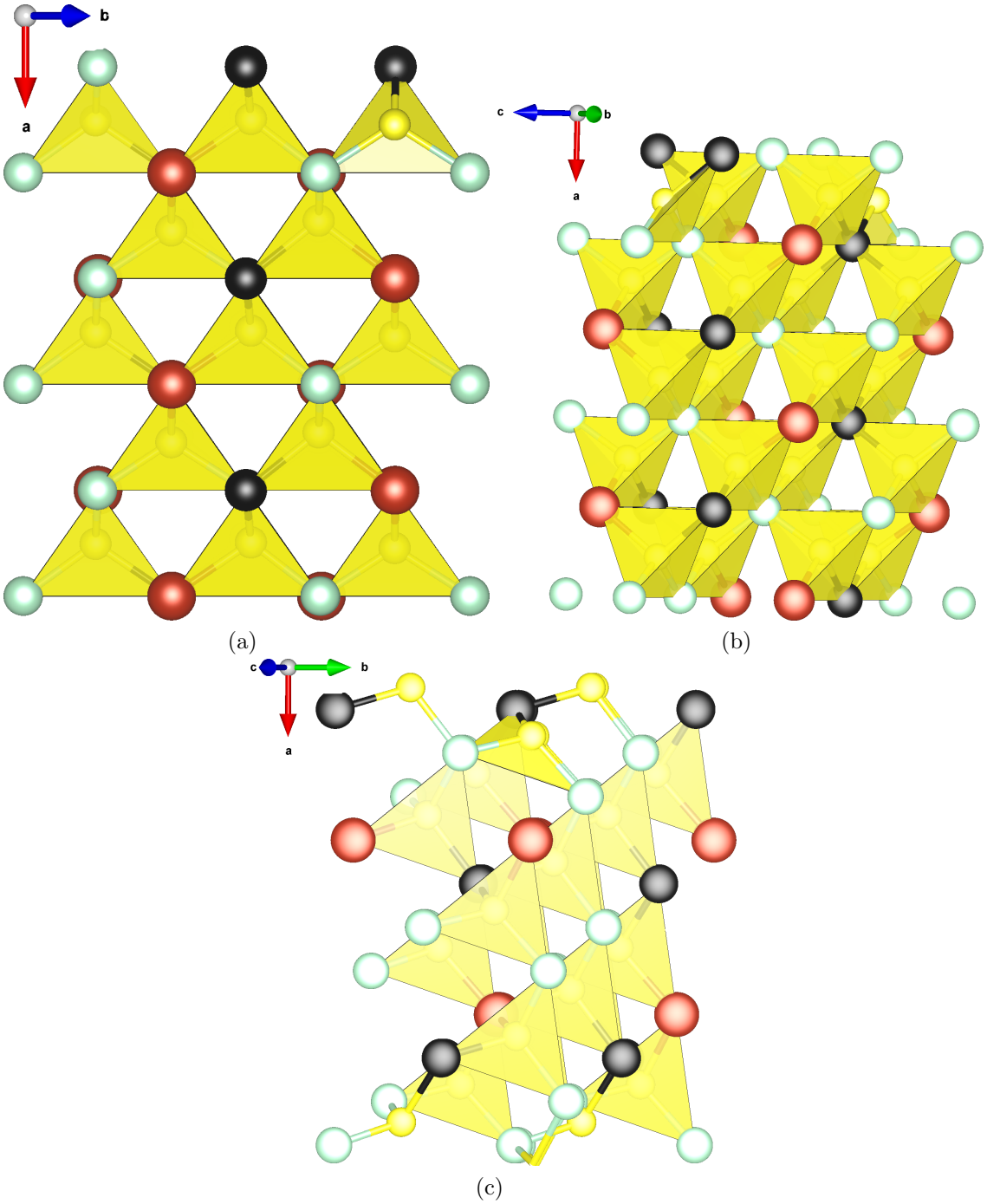

Figure 5.10: Unrelaxed Structure of the (1 1 2), (a); (0 1 0), (b) and (1 0 1), (c) surfaces shown from a side-on perspective.

planes. In the case of Shinde[187], the alignment of samples along these planes may be a result of the unusual synthetic process used, but it is also possible that the planes observed by these authors are passivated in some way which is not accounted for in our simulations.

We suggest that due to the dipolar nature of the vast majority of surface cuts, the effects of surface-passivation, either by the capping effect of additives such as templating agents present in the synthesis or the reduction/oxidation of surface cations such as $Cu^{+/2+}$ or $Sn^{2+/4+}$, will have a major impact on the relative energetics of surface cuts in Cu_2ZnSnS_4. We believe that this area warrants further investigation and that the scope of such studies should be extended to examine the Cu_2ZnSnS_4/CdS interface, as this is thought to be a major centre for charge-carrier recombination.

5.4 Chapter Summary

This chapter describes computational studies of the polymorphism, cation site disorder and surface properties of Cu_2ZnSnS_4, which can be summarised as follows.

1. We have investigated the polymorphism which arises in Cu_2ZnSnS_4 as a result of disorder in the Cu/Zn sublattice. Our results suggest that stannite and stannite-type polymorphs are unfavourable and only account for a small proportion of a given sample as found experimentally. We suggest that the composition of Cu_2ZnSnS_4 samples will be dominated by a mixture of cation ordering schemes that are kesterite-like. However, formation of perfectly ordered kesterite may not be possible due to entropic considerations.

2. We have shown the effect of temperature on the distribution of structural configurations in Cu_2ZnSnS_4 and how this configurational composition affects the lattice parameters a, b and c. We discuss how the variance in these parameters with composition leads to a change in the tetragonal distortion. We find that temperature-driven changes in the configurational composition affect the tetragonal distortion, and that our calculations are in good agreement with experimental data from quench-cooled powder samples. We show that the composition-driven changes in tetragonal distortion do not result in a reversal of the sign of the crystal field, and hence an alteration of the anisotropy of the effective mass. We also show that the magnitude of these changes in the tetragonal distortion is small with respect to the spread of the experimental data, and consequently we conclude that other factors such as strain and stoichiometry may affect the tetragonal distortion to a greater extent.

3. Interatomic potentials methods have been used for the first time to study the surface properties of kesterite Cu_2ZnSnS_4. We show that the vast majority of the low index surface cuts result in a dipolar surface, and that in only a few cases is surface reconstruction/relaxation able to eliminate the dipole whilst retaining a low surface energy. We have calculated the surface energies and

surface structures for the (1 1 2), (0 1 0) and (1 0 1) surfaces of Cu_2ZnSnS_4. We find that the majority of experimental thin-films report orientation with the (1 1 2) direction, which agrees with our low calculated surface energy for this surface. We suggest that due to the dipolar nature of the majority of surface cuts, the effect of surface-passivation upon the energetics (and hence relative expression of the various surface facets) of Cu_2ZnSnS_4, will be significant and warrants further investigation.

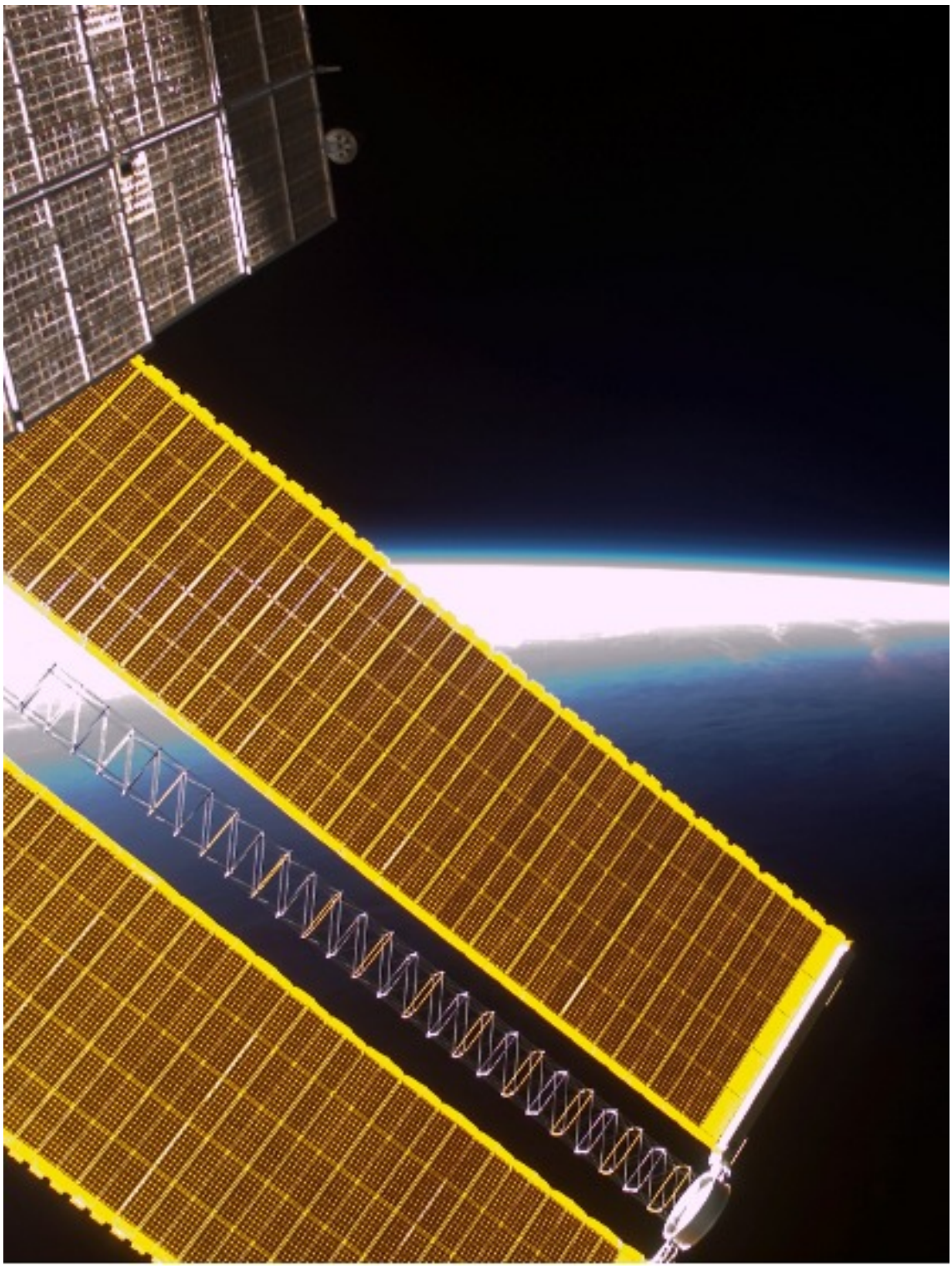

Chapter 6

Conclusions and Future Work

6.1 General Remarks

New thin-film solar cell materials and a greater understanding of their properties are needed to meet the urgent demand for sustainable, lower-cost and scalable photovoltaics. This thesis details the computer simulation studies of the potential photovoltaic absorber materials Cu_2ZnSnS_4, $CuSbS_2$ and $CuBiS_2$. We have attempted to develop the fundamental understanding of various atomic-scale properties of these novel and complex materials. This thesis is concluded by a summary of our findings and details of possible future work in each area of study.

6.2 Structural and Electronic Properties of the Ternary Sulphides $CuSbS_2$ and $CuBiS_2$

In chapter 3, we studied the structural and electronic properties of the ternary sulphides $CuSbS_2$ and $CuBiS_2$. Using a hybrid-DFT approach, we were able to accurately describe the complex and distorted structures of both these materials, and to predict the band gaps and densities of states in both cases. We calculated the band gaps to be 1.69 eV and 1.55 eV in $CuSbS_2$ and $CuBiS_2$ respectively. From our orbital-projected densities of states, we find that photoexcitation will lead to formation of hole carriers in the Cu d^{10} band, and consequently will involve oxidation of Cu(I). We have shown the stereoactivity of the Sb/Bi lone-pairs, and that the revised lone-pair model can explain the structural distortion observed in the SbS_5/BiS_5 units.

Future Work: In order to extend this study, future work could be focused in a number of areas. As little is known about the defect and ion transport properties of these materials, it would be instructive to investigate the favoured types of intrinsic defect disorder and what effect these exert on the structural/electronic

properties. In related Cu-containing sulphide semiconductors, Cu-transport has significant consequences for the material's utility in photovoltaic devices. Investigating the mobility and transport mechanism of atomic species, especially Cu, in $CuSbS_2$ and $CuBiS_2$ would inform their viability in devices. Our calculations show that the band gaps of $CuSbS_2$ and $CuBiS_2$ are relatively large when compared to semiconductors commonly used in photovoltaic applications. To further understand the success of $CuBiS_2$ and $CuSbS_2$ as absorber layer materials in photovoltaic cells band structure calculations are required to determine if they show direct or indirect band gaps. A study of possible dopants in both these materials which was able to assess the solubility of a wide range of cations and predicting the effects of these on electronic properties would be of great value. It may be that, as is the case in CIS/CIGS devices, additional dopants can be used to tune the band gap. Lastly, as with the other materials, a greater understanding of the surfaces and the interface with the CdS buffer layer may help to eliminate premature recombination and thus improve device efficiency.

6.3 Structural, Defect and Ion-Transport Properties of Cu_2ZnSnS_4

In Chapter 4 we investigated the quaternary Cu_2ZnSnS_4, focusing on the intrinsic defect and ion transport properties. We derive interatomic potentials which describe the structure of both the kesterite and stannite polymorphs accurately, and these were used to probe the favourability of a wide range of defect formation reactions. We find that the most favourable intrinsic defect is the Cu/Zn antisite, and defect cluster calculations suggest that small neutral defect clusters are favoured. This suggests a degree of self-passivation, which is important when we consider the trapping of short-lived charge carriers.

We find all forms of Schottky disorder, as well as the Zn Frenkel and Sn Frenkel defects, to be unfavourable due to their high formation energies. The Cu Frenkel has a moderate energy, and at the elevated temperatures common in many synthetic processes it may explain the higher mobility of Cu observed in synthesis.

We have studied the Cu migration in Cu_2ZnSnS_4 and find that migration occurs via a V'_{Cu} hopping mechanism that allow Cu-diffusion in three dimensions. We calculate the barrier to this hop to be 0.69 eV and 0.76 eV using the DFT and interatomic potential formalisms respectively, showing good accord. This leads to a calculated Cu diffusion coefficient in the $10^{-14} - 10^{-15}$ cm^2s^{-1} range, which is slower than in the related CIGS materials.

Future work: There are several areas upon which future work could focus. One of these is the issue of Cu out-diffusion. We have shown that Cu ions are able to migrate, although their diffusion is slower than in related materials. This may be beneficial to cell performance as it allows for a degree of "self-repair" following

radiation damage. However, if the chemical potential of Cu is lower in CdS than it is in Cu_2ZnSnS_4, then this Cu mobility will allow Cu to leach out of the absorber layer leading to device failure. Clarifying whether this is the case and if so, whether an alternative buffer layer could be used, is highly recommended.

6.4 Polymorphism and Surface Properties of Cu_2ZnSnS_4

In chapter 5 we investigated the Cu/Zn site disorder that leads to a large number of polymorphs. We find that the formation of stannite and stannite-type polymorphs of Cu_2ZnSnS_4 is not favoured, and indicate that the majority of a Cu_2ZnSnS_4 sample will be comprised of a mixture of kesterite and kesterite-like configurations as observed experimentally. We show how temperature will affect the distribution of configurations observed within a Cu_2ZnSnS_4 sample, and how these temperature driven configurational changes affect the unit cell parameters, and consequently the tetragonal distortion.

Studying the surfaces of Cu_2ZnSnS_4 we find that the vast majority of the low index surfaces are dipolar in nature when cleaved, and that only the (1 1 2), (0 1 0) and (1 0 1) type surfaces are able to achieve a low surface energy through reconstruction/relaxation. We have calculated the surface energy and surface structures for these indexes and suggest that surface passivation through capping or oxidation/reduction of surface ions will significantly affect the observed surface properties of Cu_2ZnSnS_4.

Future work: In this work we have not considered the effect of polymorphism upon the electronic properties, such as the band gap, of Cu_2ZnSnS_4. With sufficient resources to use hybrid DFT, it would be instructive to investigate how the variations in cation configuration we have identified affect the electronic properties of Cu_2ZnSnS_4, and whether controlling the composition with synthesis temperature, would allow control over electronic as well structural properties. Also, extending the studies of surfaces to include DFT calculations and the effects of surface passivation would allow a more complete picture of the interface properties.

Bibliography

[1] MacKay, D. J. *Sustainable Energy — without the hot air.* UIT, Cambridge, (2008).

[2] Goetzberger, A., Hebling, C., and Schock, H.-W. *Materials Science and Engineering R-Reports,* **40**(1), 1–46 (2003).

[3] Bequerel, E. *C.R. Acad. Sci.,* **9**, 145–149 (1839).

[4] Adams, W. and Day, R. *On the Action of Light on Selenium,* **1**, 113 (1876).

[5] Nelson, J. *The Physics of Solar Cells.* Imperial College Press, London, (2003).

[6] Shockley, W. and Queisser, H. J. *Journal of Applied Physics* **32**(3), 510–519 (1961).

[7] Peter, L. M. *Philosophical Transactions of the Royal Society A-Mathematical Physical and Engineering Sciences,* **369**(1942), 1840–1856 (2011).

[8] Green, M. A., Emery, K., Hishikawa, Y., Warta, W., and Dunlop, E. D. *Progress in Photovoltaics,* **20**(5, SI), 606–614 (2012).

[9] Cheng, Y. Y., Fuckel, B., MacQueen, R. W., Khoury, T., Clady, R. G. C. R., Schulze, T. F., Ekins-Daukes, N. J., Crossley, M. J., Stannowski, B., Lips, K., and Schmidt, T. W. *Energy and Environmental Science,* **5**, 6953–6959 (2012).

[10] Nazeeruddin, M., Kay, A., Rodicio, I., Humphrybaker, R., Muller, E., Liska, P., Vlachopoulos, N., and Gratzel, M. *Journal of the American Chemical Society,* **115**(14), 6382–6390 (1993).

[11] Oregan, B. and Gratzel, M. *Nature,* **353**(6346), 737–740 (1991).

[12] Gratzel, M. *Nature,* **414**(6861), 338–344 (2001).

[13] Gratzel, M. *Philosophical Transactions of the Royal Society A-Mathematical Physical and Engineering Sciences,* **365**(1853), 993–1005 (2007).

[14] Hardin, B. E., Snaith, H. J., and McGehee, M. D. *Nature Photonics,* **6**(3), 162–169 (2012).

[15] Li, G., Shrotriya, V., Huang, J., Yao, Y., Moriarty, T., Emery, K., and Yang, Y. *Nature Materials,* **4**(11), 864–868 (2005).

[16] Hagfeldt, A. and Gratzel, M. *Accounts of Chemical Research,* **33**(5), 269–277 (2000).

[17] Thompson, B. C. and Frechet, J. M. J. *Angewandte Chemie-International Edition,* **47**(1), 58–77 (2008).

[18] Schmidt-Mende, L., Fechtenkotter, A., Mullen, K., Moons, E., Friend, R., and MacKenzie, J. *Science,* **293**(5532), 1119–1122 (2001).

[19] Yang, X., Loos, J., Veenstra, S., Verhees, W., Wienk, M., Kroon, J., Michels, M., and Janssen, R. *Nano Letters,* **5**(4), 579–583 (2005).

[20] Liang, Y., Xu, Z., Xia, J., Tsai, S.-T., Wu, Y., Li, G., Ray, C., and Yu, L. *Advanced Materials,* **22**(20), 135 (2010).

[21] Bundgaard, E. and Krebs, F. C. *Solar Energy Materials and Solar Cells,* **91**(11), 954–985 (2007).

[22] Jorgensen, M., Norrman, K., and Krebs, F. C. *Solar Energy Materials and Solar Cells,* **92**(7), 686–714 (2008).

[23] Spanggaard, H. and Krebs, F. *Solar Energy Materials and Solar Cells,* **83**(2-3), 125–146 (2004).

[24] Cusano, D. *Solid-State Electronics,* **6**(3), 217–232 (1963).

[25] Levi, D., Woods, L., Albin, D., Gessert, T., Niles, D., Swartzlander, A., Rose, D., Ahrenkiel, R., and Sheldon, P. In *Thin-Film Structures for Photovoltaics,* Jones, ED and Kalejs, J and Noufi, R and Sopori, B, editor, volume 485, 209–214, (1998).

[26] Jaeger-Waldau, A. *International Journal of Photoenergy,* **2012**, 768368 (2012).

[27] Wagner, S., Shay, J., Migliora.P, and Kasper, H. *Applied Physics Letters,* **25**(8), 434–435 (1974).

[28] Kazmerski, L., Ayyagari, M., White, F., and Sanborn, G. *Journal of Vacuum Science and Technology* **13**(1), 139–144 (1976).

[29] Kazmerski, L., White, F., and Morgan, G. *Applied Physics Letters,* **29**(4), 268–270 (1976).

[30] Kazmerski, L., Morgan, G., Sanborn, G., and White, F. *Bulletin of the American Physical Society,* **21**(3), 378 (1976).

[31] Li, H., Zhang, Q., Pan, A., Wang, Y., Zou, B., and Fan, H. J. *Chemistry of Materials,* **23**(5), 1299–1305 (2011).

[32] Mesa, F., Gordillo, G., Dittrich, T., Ellmer, K., Baier, R., and Sadewasser, S. *Applied Physics Letters,* **96**(8), 082113 (2010).

[33] Mesa, F., Dussan, A., and Gordillo, G. *Physica Status Solidi C - Current Topics in Solid State Physics,* **7**(3-4), 917–920 (2010).

[34] Manolache, S., Duta, A., Isac, L., Nanu, M., Goossens, A., and Schoonman, J. *Thin Solid Films,* **515**(15), 5957–5960 (2007).

[35] Gerein, N. J. and Haber, J. A. *Chemistry of Materials,* **18**(26), 6297–6302 (2006).

[36] Mesa, F., Dussan, A., and Gordillo, G. *Physica B-Condensed Matter,* **404**(23-24), 5227–5230 (2009).

[37] Zhou, J., Bian, G.-Q., Zhu, Q.-Y., Zhang, Y., Li, C.-Y., and Dai, J. *Journal of Solid State Chemistry,* **182**(2), 259–264 (2009).

[38] Ezugwu, S. C., Ezema, F. I., and Asogwa, P. U. *Chalcogenide Letters,* **7**(5), 369–376 (2010).

[39] Rabhi, A., Kanzari, M., and Rezig, B. *Thin Solid Films,* **517**(7), 2477–2480 (2009).

[40] Rodriguez-Lazcano, Y., Nair, M., and Nair, P. *Journal of Crystal Growth,* **223**(3), 399–406 (2001).

[41] Pfitzner, A. *Zeitschrift fur Kristallographie,* **213**(4), 228–236 (1998).

[42] Pfitzner, A. *Zeitschrift fur Anorganische und Allgemeine Chemie,* **620**(11), 1992–1997 (1994).

[43] Makovicky, E. and Baliczunic, T. *Canadian Mineralogist,* **33**(Part 3), 655–663 (1995).

[44] Kocman, V. and Nuffield, E. *Acta Crystallographica Section B-Structural Science,* **29**(NOV15), 2528–2535 (1973).

[45] Scragg, J. J., Dale, P. J., and Peter, L. M. *Electrochemistry Communications,* **40**(4), 639–642 (2001).

[46] Ito, K. and Nakazawa, T. *Japanese Journal of Applied Physics Part 1-Regular Papers Short Notes and Review Papers,* **27**(11), 2094–2097 (1988).

[47] Seol, J., Lee, S., Lee, J., Nam, H., and Kim, K. *Solar Energy Materials and Solar Cells,* **75**(1-2), 155–162 (2003).

[48] Matsushita, H., Maeda, T., Katsui, A., and Takizawa, T. *Journal of Crystal Growth,* **208**(1-4), 416–422 (2000).

[49] Barkhouse, D. A. R., Gunawan, O., Gokmen, T., Todorov, T. K., and Mitzi, D. B. *Progress in Photovoltaics,* **20**(1), 6–11 (2012).

[50] Bag, S., Gunawan, O., Gokmen, T., Zhu, Y., Todorov, T. K., and Mitzi, D. B. *Energy and Environmental Science,* **5**(5), 7060–7065 (2012).

[51] Catlow, C. R. A., Guo, Z. X., Miskufova, M., Shevlin, S. A., Smith, A. G. H., Sokol, A. A., Walsh, A., Wilson, D. J., and Woodley, S. M. *Philosophical Transactions of the Royal Society A-Mathematical Physical and Engineering Sciences,* **368**(1923), 3379–3456 (2010).

[52] Catlow, C. R. A., Bell, R. G., and Gale, J. D. *Journal of Materials Chemistry,* **4**(6), 781–792 (1994).

[53] Catlow, C. R. A. and Mackrodt, W. C. *Computer simulation of solids.* Springer-Verlag, Berlin, (1982).

[54] Catlow, C. R. A. *Computer modelling in inorganic crystallography.* Academic Press; San Diego, (1997).

[55] Sayle, D. C., Catlow, C. R. A., Perrin, M. A., and Nortier, P. *Journal of Physics and Chemistry of Solids,* **56**(6), 799–805 (1995).

[56] Leach, A. R. *Molecular Modelling, Principals and Applications.* Pearson, Prentice Hall, 2^{nd} edition, (2001).

[57] Koch, W. and Holthausen, M. C. *A Chemist's Guide to Density Functional Theory.* Wiley-VCH, 2^{nd} edition, (2000).

[58] Shanno, D. *Mathematics of Computation,* **24**(111), 647 (1970).

[59] Mills, G., Jonsson, H., and Schenter, G. *Surface Science,* **324**(2-3), 305–337 (1995).

[60] Henkelman, G. and Jonsson, H. *Journal of Chemical Physics,* **113**(22), 9978–9985 (2000).

[61] Henkelman, G., Uberuaga, B., and Jonsson, H. *Journal of Chemical Physics,* **113**(22), 9901–9904 (2000).

[62] Grau-Crespo, R., Hamad, S., Catlow, C. R. A., and de Leeuw, N. H. *Journal of Physics-Condensed Matter,* **19**(25), 256201 (2007).

[63] Wang, Q., Grau-Crespo, R., and de Leeuw, N. H. *Journal of Physical Chemistry, B* **115**(47), 13854–13861 (2011).

[64] Born, M. *Physik,* **1**, 45–48 (1920).

[65] Morse, P. *Physical Review,* **34**, 57–64 (1929).

[66] Lennard-Jones, J. E. *Proc. R. Soc. Lond. A,* **106**(738), 463–477 (1924).

[67] Buckingham, R. *Proc. R. Soc. Lond. A,* **168**, 264–283 (1938).

[68] Armstrong, A. R., Lyness, C., Panchmatia, P. M., Islam, M. S., and Bruce, P. G. *Nature Materials,* **10**(3), 223–229 (2011).

[69] Islam, M. S. and Catlow, C. R. A. *Journal of Solid State Chemistry,* **77**(1), 180–189 (1988).

[70] Olson, C. L., Nelson, J., and Islam, M. S. *Journal of Physical Chemistry, B* **110**(20), 9995–10001 (2006).

[71] Sithole, H., Ngoepe, P., and Wright, K. *Physics and Chemistry of Minerals,* **30**(10), 615–619 (2003).

[72] Wright, K. and Jackson, R. *Journal of Materials Chemistry,* **5**(11), 2037–2040 (1995).

[73] Heyes, D., Barber, M., and Clarke, J. *Journal of the Chemical Society-Faraday Transactions II,* **73**(Part 10), 1485–1496 (1977).

[74] Dick, B. G. and Overhauser, A. W. *Physical Review,* **112**(1), 90 (1958).

[75] Mott, N. F. and Littleton, M. J. *Trans. Faraday Soc.,* **34**, 485–499 (1938).

[76] Kohn, W. *Reviews of Modern Physics,* **71**(5), 1253–1266 (1999).

[77] Thomas, L. *Proc. Cambridge Phil. Soc.,* **23**(5), 542–548 (1927).

[78] Fermi, E. *Rend. Accad. Naz. Lincei,* **6**, 602–607 (1927).

[79] Hohenberg, P. and Kohn, W. *Physical Review,* **136**(3B), B864–B871 (1964).

[80] Kohn, W. and Sham, L. J. *Physical Review,* **140**(4A), A1133–A1138 (1965).

[81] Schroedinger, E. *Physical Review,* **28**(6), 1049–1070 (1926).

[82] Perdew, J. P., Burke, K., and Ernzerhof, M. *Physical Review Letters* **77**(18), 3865–3868 (1996).

[83] Perdew, J. P. and Wang, Y. *Physical Review B,* **45**(23), 13244–13249 (1992).

[84] Wu, Z. and Cohen, R. *Physical Review B,* **73**(23), 235116 (2006).

[85] Blochl, P. *Physical Review B,* **50**(24), 17953–17979 (1994).

[86] Monkhorst, H. and Pack, J. *Physical Review B,* **13**(12), 5188–5192 (1976).

[87] Perdew, J. and Zunger, A. *Physical Review B,* **23**(10), 5048–5079 (1981).

[88] Cohen, A. J., Mori-Sanchez, P., and Yang, W. *Science,* **321**(5890), 792–794 (2008).

[89] Matsushita, Y.-i., Nakamura, K., and Oshiyama, A. *Physical Review B,* **84**(7), 075205 (2011).

[90] Becke, A. *Physical Review A,* **38**(6), 3098–3100 (1988).

[91] Becke, A. *Journal of Chemical Physics,* **98**(7), 5648–5652 (1993).

[92] Perdew, J., Emzerhof, M., and Burke, K. *Journal of Chemical Physics,* **105**(22), 9982–9985 (1996).

[93] Heyd, J., Scuseria, G. E., and Ernzerhof, M. *Journal of Chemical Physics,* **118**(18), 8207–8215 (2003).

[94] Krukau, A. V., Vydrov, O. A., Izmaylov, A. F., and Scuseria, G. E. *Journal of Chemical Physics,* **125**(22) (2006).

[95] Romeo, A., Terheggen, A., Abou-Ras, D., Batzner, D., Haug, F., Kalin, M., Rudmann, D., and Tiwari, A. *Progress in Photovoltaics,* **12**(2-3), 93–111 (2004).

[96] Ginley, D., Green, M. A., and Collins, R. *MRS Bulletin,* **33**(4), 355–364 (2008).

[97] Schmidtke, J. *Optics Express,* **18**(19), A477–A486 (2010).

[98] Todorov, T. K., Reuter, K. B., and Mitzi, D. B. *Advanced Materials,* **22**, 1 (2010).

[99] Xiao, H., Tahir-Kheli, J., and Goddard, W. A. *Journal of Physical Chemistry Letters,* **2**(3), 212–217 (2011).

[100] Scanlon, D. O. and Watson, G. W. *Applied Physics Letters,* **97**(13), 131904 (2010).

[101] Pohl, J. and Albe, K. *Journal of Molecular Catalysis A-Chemical,* **328**(1-2), 023509 (2010).

[102] Seminovski, Y., Palacios, P., and Wahnon, P. *Thin Solid Films,* **519**(21, SI), 7517–7521 (2011).

[103] Paier, J., Asahi, R., Nagoya, A., and Kresse, G. *Physical Review B,* **79**(11), 115126 (2009).

[104] Chen, S., Gong, X. G., Walsh, A., and Wei, S.-H. *Applied Physics Letters,* **94**(4), 036601 (2009).

[105] Kresse, G. and Joubert, D. *Physical Review B,* **59**(3), 1758–1775 (1999).

[106] Kresse, G. and Furthmuller, J. *Computational Materials Science,* **6**(1), 15–50 (1996).

[107] Kresse, G. and Furthmuller, J. *Physical Review B,* **54**(16), 11169–11186 (1996).

[108] Parker, D. and Singh, D. J. *Physical Review B,* **83**(23), 233206 (2011).

[109] Islam, M. S. *Philosophical Transactions of the Royal Society A-Mathematical Physical and Engineering Sciences,* **368**(1923), 3255–3267 (2010).

[110] Walsh, A., Ahn, K.-S., Shet, S., Huda, M. N., Deutsch, T. G., Wang, H., Turner, J. A., Wei, S.-H., Yan, Y., and Al-Jassim, M. M. *Energy and Environmental Science,* **2**(7), 774–782 (2009).

[111] Kyono, A. and Kimata, M. *American Mineralogist,* **90**(1), 162–165 (2005).

[112] Pawar, S., Pawar, A., and Bhosale, P. *Bulletin of Materials Science,* **8**(3), 423–426 (1986).

[113] Sonawane, P., Wani, P., Patil, L., and Seth, T. *Materials Chemistry and Physics,* **84**(2-3), 221–227 (2004).

[114] Colombara, D., Peter, L. M., Rogers, K. D., Painter, J. D., and Roncallo, S. *Thin Solid Films,* **519**(21, SI), 7438–7443 (2011).

[115] Weber, A., Mainz, R., and Schock, H. W. *Journal of Applied Physics,* **107**(1), 013516 (2010).

[116] Yang, Z., Meinhardt, K., and Stevenson, J. *Journal of the Electrochemical Society,* **150**(8), A1095–A1101 (2003).

[117] Colombara, D., Peter, L. M., Hutchings, K., Rogers, K. D., Schaefer, S., Dufton, J. T. R., and Islam, M. S. *Thin Solid Films,* **520**(16), 5165–5171 (2012).

[118] Chen, S., Yang, J.-H., Gong, X. G., Walsh, A., and Wei, S.-H. *Physical Review B,* **81**(24), 245204 (2010).

[119] Brik, M. G. *Journal of Physics-Condensed Matter,* **21**(48), 485202 (2009).

[120] Gillespie, R. and Nyholm, R. *Quarterly Reviews,* **11**, 339–380 (1957).

[121] Walsh, A., Payne, D. J., Egdell, R. G., and Watson, G. W. *Chemical Society Reviews,* **40**(9), 4455–4463 (2011).

[122] Tanaka, T., Nagatomo, T., Kawasaki, D., Nishio, M., Guo, Q., Wakahara, A., Yoshida, A., and Ogawa, H. *Journal of Physics and Chemistry of Solids,* **66**(11), 1978–1981 (2005).

[123] Katagiri, H. *Thin Solid Films,* **480**(Sp. Iss. SI), 426–432 (2005).

[124] Katagiri, H., Jimbo, K., Yamada, S., Kamimura, T., Maw, W. S., Fukano, T., Ito, T., and Motohiro, T. *Applied Physics Express,* **1**(4), 041201 (2008).

[125] Katagiri, H., Jimbo, K., Maw, W. S., Oishi, K., Yamazaki, M., Araki, H., and Takeuchi, A. *Thin Solid Films,* **517**(7), 2455–2460 (2009).

[126] Wang, K., Gunawan, O., Todorov, T., Shin, B., Chey, S. J., Bojarczuk, N. A., Mitzi, D., and Guha, S. *Applied Physics Letters,* **97**(14), 143508 (2010).

[127] Nakayama, N. and Ito, K. *Applied Surface Science,* **92**, 171–175 (1996).

[128] Scragg, J. J., Dale, P. J., Peter, L. M., Zoppi, G., and Forbes, I. *Physica Status Solidi B-Basic Solid State Physics,* **245**(9), 1772–1778 (2008).

[129] Scragg, J. J., Dale, P. J., and Peter, L. M. *Thin Solid Films,* **517**(7), 2481–2484 (2009).

[130] Ramasamy, K., Malik, M. A., and O'Brien, P. *Chemical Science,* **2**(6), 1170–1172 (2011).

[131] Washio, T., Shinji, T., Tajima, S., Fukano, T., Motohiro, T., Jimbo, K., and Katagiri, H. *Journal of Materials Chemistry,* **22**(9), 4021–4024 (2012).

[132] Chen, S., Gong, X. G., Walsh, A., and Wei, S.-H. *Applied Physics Letters,* **90**, 021902 (2010).

[133] Walsh, A., Chen, S., Wei, S.-H., and Gong, X.-G. *Advanced Energy Materials,* **2**(4), 400–409 (2012).

[134] Siebentritt, S. and Schorr, S. *Progress in Photovoltaics,* **20**(5, SI), 512–519 (2012).

[135] Redinger, A., Berg, D. M., Dale, P. J., and Siebentritt, S. *Journal of the American Chemical Society,* **133**(10), 3320–3323 (2011).

[136] Guo, Q., Hillhouse, H. W., and Agrawal, R. *Journal of the American Chemical Society,* **131**(33), 11672+ (2009).

[137] Steinhagen, C., Panthani, M. G., Akhavan, V., Goodfellow, B., Koo, B., and Korgel, B. A. *Journal of the American Chemical Society,* **131**(35), 12554+ (2009).

[138] Riha, S. C., Parkinson, B. A., and Prieto, A. L. *Journal of the American Chemical Society,* **131**(34), 12054+ (2009).

[139] Wright, K. and Gale, J. *Physical Review B,* **70**(3), 036601 (2004).

[140] Wright, K. and Vaughan, D. J. *Molecular Simulation,* **21**(2-3), 89–103 (1998).

[141] Bonazzi, P., Bindi, L., Bernardini, G., and Menchetti, S. *Canadian Mineralogist,* **41**(Part 3), 639–647 (2003).

[142] Evans, H. *Zeitschrift fur Kristallographie,* **150**(1-4), 299–320 (1979).

[143] Ballentyne, D. *Journal of Physics and Chemistry of Solids,* **10**(2-3), 242 (1959).

[144] Hazen, R. and Finger, L. *American Mineralogist,* **63**(3-4), 289–292 (1978).

[145] Zhang, S., Wei, S., Zunger, A., and Katayama-Yoshida, H. *Physical Review B,* **57**(16), 9642–9656 (1998).

[146] Schorr, S. *Thin Solid Films,* **515**(15), 5985–5991 (2007).

[147] Schorr, S., Tovar, M., Hoebler, H.-J., and Schock, H.-W. *Thin Solid Films,* **517**(7), 2508–2510 (2009).

[148] Guillemoles, J., Kronik, L., Cahen, D., Rau, U., Jasenek, A., and Schock, H. *Journal of Physical Chemistry, B* **104**(20), 4849–4862 (2000).

[149] Otte, K., Chasse, T., Lippold, G., Rauschenbach, B., and Szargan, R. *Journal of Applied Physics,* **91**(3), 1624–1627 (2002).

[150] Diaz, R. *Journal of Physics D-Applied Physics,* **41**(18), 185102 (2008).

[151] Kutner, R. *Physics Letters A,* **81**(4), 239–240 (1981).

[152] Tripathi, R., Gardiner, G. R., Islam, M. S., and Nazar, L. F. *Chemistry of Materials,* **23**(8), 2278–2284 (2011).

[153] Vineyard, G. H. *Journal of Physics and Chemistry of Solids,* **3**(1–2), 121–127 (1957).

[154] Van der Ven, A. and Ceder, G. *Journal of Power Sources,* **97-8**(SI), 529–531 (2001).

[155] Lyubomirsky, I., Rabinal, M., and Cahen, D. *Journal of Applied Physics,* **81**(10), 6684–6691 (1997).

[156] Nadazdy, V., Yakushev, M., Djebbar, E., Hill, A., and Tomlinson, R. *Journal of Applied Physics,* **84**(8), 4322–4326 (1998).

[157] Ichimura, M. and Nakashima, Y. *Japanese Journal of Applied Physics,* **48**(9, Part 1), 090202 (2009).

[158] Schorr, S., Hoebler, H.-J., and Tovar, M. *European Journal of Mineralogy,* **19**(1), 65–73 (2007).

[159] Schorr, S. *Solar Energy Materials and Solar Cells,* **95**(6, SI), 1482–1488 (2011).

[160] Kheraj, V., Patel, K. K., Patel, S. J., and Shah, D. V. *Journal of Crystal Growth,* **362**, 174–177 (2013).

[161] Shay, J. L. and Wernick, J. H. *Ternary chalcopyrite semiconductors: growth, electronic properties, and applications*. Pergamon Press, (1975).

[162] Alonso, M., Garriga, M., Rincon, C., Hernandez, E., and Leon, M. *Applied Physics A-Materials Science and Processing,* **74**(5), 659–664 (2002).

[163] Hones, K., Eickenberg, M., Siebentritt, S., and Persson, C. *Applied Physics Letters,* **93**(9), 092102 (2008).

[164] Persson, C. *Applied Physics Letters,* **93**(7), 072106 (2008).

[165] Herberholz, R. In *Ternary and Multinary Compounds,* Tomlinson, RD and Hill, AE and Pilkington, RD, editor, volume 152 of *Institute of Physics Conference Series*, 733–740, (1998).

[166] Ashour, S., Alkuhaimi, S., Moutinho, H., Matson, R., and Abouelfotouh, F. *Thin Solid Films,* **226**(1), 129–134 (1993).

[167] Herberholz, R., Igalson, M., and Schock, H. *Journal of Applied Physics,* **83**(1), 318–325 (1998).

[168] Niemegeers, A., Burgelman, M., Herberholz, R., Rau, U., Hariskos, D., and Schock, H. *Progress in Photovoltaics,* **6**(6), 407–421 (1998).

[169] Abouelfotouh, F., Moutinho, H., Bakry, A., Coutts, T., and Kazmerski, L. *Solar Cells,* **30**(1-4), 151–160 (1991).

[170] Heath, J., Cohen, J., and Shafarman, W. *Thin Solid Films,* **431**, 426–430 (2003).

[171] Chakrabarti, R., Maity, A., Maiti, B., Dutta, J., Chaudhuri, S., and Pal, A. *Vacuum,* **47**(11), 1371–1378 (1996).

[172] Watson, G. W., Kelsey, E. T., and Parker, S. C. *Philosophical Magazine A-Physics of Condensed Matter Structure Defects and Mechanical Properties,* **79**(3), 527–536 (1999).

[173] Tasker, P. *Journal of Physics C-Solid State Physics,* **12**(22), 4977–4984 (1979).

[174] Parker, S. C., Oliver, P. M., DeLeeuw, N. H., Titiloye, J. O., and Watson, G. W. *Phase Transitions,* **61**(1-4), 83–107 (1997).

[175] Chalapathy, R. B. V., Jung, G. S., and Ahn, B. T. *Solar Energy Materials and Solar Cells,* **95**(12), 3216–3221 (2011).

[176] Shin, S. W., Pawar, S. M., Park, C. Y., Yun, J. H., Moon, J.-H., Kim, J. H., and Lee, J. Y. *Solar Energy Materials and Solar Cells,* **95**(12), 3202–3206 (2011).

[177] Jeon, M., Tanaka, Y., Shimizu, T., and Shingubara, S. *Energy Procedia* **10**, 255–260 (2011).

[178] Yoo, H. and Kim, J. *AIP Conf. Proc.* **1399**, 157–158 (2011).

[179] Liu, F., Li, Y., Zhang, K., Wang, B., Yan, C., Lai, Y., Zhang, Z., Li, J., and Liu, Y. *Solar Energy Materials and Solar Cells,* **94**(12), 2431–2434 (2010).

[180] Kobayashi, T., Jimbo, K., Tsuchida, K., Shinoda, S., Oyanagi, T., and Katagiri, H. *Japanese Journal of Applied Physics, Part 1-Regular Papers Brief Communications and Review Papers* **44**(1B), 783–787 (2005).

[181] Moriya, K., Tanaka, K., and Uchiki, H. *Japanese Journal of Applied Physics, Part 1-Regular Papers Brief Communications and Review Papers* **44**(1B), 715–717 (2005).

[182] Katagiri, H., Ishigaki, N., Ishida, T., and Saito, K. *Japanese Journal of Applied Physics, Part 1-Regular Papers Short Notes and Review Papers* **40**(2A), 500–504 (2001).

[183] Salome, P. M. P., Malaquias, J., Fernandes, P. A., Ferreira, M. S., Leitao, J. P., da Cunha, A. F., Gonzalez, J. C., Matinaga, F. N., Ribeiro, G. M., and Viana, E. R. *Solar Energy Materials and Solar Cells,* **95**(12), 3482–3489 (2011).

[184] Li, W., Jiang, K., Zhang, J., Chen, X., Hu, Z., Chen, S., Sun, L., and Chu, J. *Physical Chemistry Chemical Physics,* **14**(28), 9936–9941 (2012).

[185] Yoo, H. and Kim, J. *Thin Solid Films,* **518**(22, SI), 6567–6572 (2010).

[186] Shi, C., Shi, G., Chen, Z., Yang, P., and Yao, M. *Materials Letters,* **73**, 89–91 (2012).

[187] Shinde, N. M., Dubal, D. P., Dhawale, D. S., Lokhande, C. D., Kim, J. H., and Moon, J. H. *Materials Research Bulletin,* **47**(2), 302–307 (2012).

Appendix A

Glossary of photovoltaic terms

A.1 Acronyms

CIS / CIGS $CuInSe_2$ / $Cu(inGa)(SSe)_2$ used as absorber layers in high efficiency thin-film photovoltaics.

CZTS / CZTSe Cu_2ZnSnS_4 / $Cu_2ZnSnSe_4$, often alloyed together to allow the band gap to be tuned via alteration of the S/Se ratio.

EQE External Quantum Efficiency

HSE03 / HSE06 The hybrid functional developed by Heyd, Sucseria, and Ernzerhof using screening parameters given in the 2003[93] and 2006[94] papers respectively.

IQE Internal Quantum Efficiency

NEB Nudged Elastic Band methodology for locating transition states in the simulations, a description of the approach is given in section 2.3.2.

PBE The semi-local functional produced by Perdew, Burke and Ernzerhof[82].

XRD X-ray diffraction

A.2 Glossary

Concentrating solar power The use of mirrors or lenses to focus radiation from the sun into a small area, greatly increasing the photon flux. There are two forms of concentrating solar power; concentrating photovoltaic power and concentrating solar thermal, with the latter being the more common means of large scale energy generation.

Concentrating Photovoltaic Power Directing concentrated light onto a small high-efficiency photovoltaic cell to gain maximum use of the cell's high efficiency. The requirement for high efficiency cells means multi-junction devices are often used. Cells must exhibit fast hole transport (as in GaAS) in order to avoid saturation which limits efficiency.

Concentrating Solar Thermal Power Directing concentrated light onto a heat exchanger where the thermal energy of the radiation heats either water or a molten salt allowing power to be generated by spinning a turbine with steam.

Solar Thermal Power The domestic use of roof-top panels where radiation from the sun heats water passing through the panels, thus reducing the amount of energy the household spends on heating water for domestic applications.

Doping The deliberate introduction of impurities (dopants) into a material in order to affect the material's properties. Dopants are classified as being either isovalent or aliovalent.

Host Ion An ion in a crystal lattice which is replaced by a dopant ion.

Aliovalent (dopant) Where the charge of a dopant ion is different to that of the host ion. Acceptor dopants have fewer valence electrons than the host ion, and donor dopants have a greater number of valence electrons than the host ion.

Isovalent (dopant) Where the charge of a dopant ion is the same as the host ion.

p-type (material) A material in which the majority charge carriers are positive (electron holes), commonly a result of doping with acceptor dopants.

n-type (material) A material where the majority charge carriers are negative (electrons), in semiconductors, which normally have a poor conductivity, this is achieved via the introduction of donor dopants.

Effective Mass The mass which a charge carrier (electron or electron hole) appears to have when moving in a solid material according to the semi-classical model of transport in crystals. It can be anisotropic due to the presence of electric or magnetic fields, and this dependence upon direction is represented by the effective mass tensor.

External Quantum Efficiency (EQE) The ratio of: the number of electrons provided to the external circuit (per second) by a solar cell; to the number of photons, of a given energy, which are incident upon the cell (per second). A measure of how effectively a cell converts incident photons into useful electrons.

Internal Quantum Efficiency (IQE) The ratio of: the number of electrons provided to the external circuit (per second) by a solar cell; to the number of photons, of a given energy, which are absorbed by the cell (per second). A

measure of how effictively a cell converts photons to useful electrons, once they have been absorbed by the cell.

Open Circuit Voltage ($\mathbf{V}_{oc}$) The maximum voltage produced by the cell. It is dependent on the cell being illuminated and being connected to an infinite resistance. The magnitude is determined by the energy difference between the fermi levels of the n-type and p-type material which comprise the cell.

Photovoltaic Solar Cell An electrochemical device which converts the energy of photons, which are incident upon it, directly into useful electrical power.

Short Circuit Current ($\mathbf{I}_{sc}$) The maximum current a cell can deliver, i.e. when the terminals are connected with no resistance.

Short Circuit Current Density ($\mathbf{J}_{sc}$) The short circuit current per unit area for the solar cell.

A.3 Kroger-Vink Notation

Throughout this work we have used the notation devised by Kroger and Vink in the description of lattice defects. This nottation allows a sucinct description of both a defect's evironment within the lattice, and its effective charge. As well as making a clear distinction between the effective charge of a point defect and the oxidation state of an ion involved in the defect.

In Kroger-Vink notation the main symbol used to describe a defect denotes whether the defect is a vacancy (V) or an atom (using the normal atomic label). This is complimented by a subscript and superscript component. The subscript component details the position of the defect in the lattice. This can be either an interstitial site (denoted by i) or a lattice site (denoted using the atomic label of the species which occupies that site). The superscript component details the effective charge of the defect. Defects with the same charge as the normal lattice site are denoted with an x. Whereas, defects with an effective positive charge are marked with a $\cdot$ and an effective negative charge with a $\prime$.

In the context of Cu_2ZnSnS_4 some examples include:

i S_S^x : A S^{2-} ion on a S^{2-} site; despite the sulphur ion being S^{2-}, the defect has no effective charge and so the superscript x is shown.

ii V'_{Cu} : A vacancy on a copper site; as the copper normally carries a 1+ charge the defect has a singular effective negative charge denoted by $\prime$.

iii Zn''_{Sn} : A Zn^{2+} on a Sn^{4+} site; the defect has an effective charge of 2-.

iv $Cu_i^{\cdot}$: A Cu^{+} on an interstitial site; the defect has an effective posetive charge.

Appendix B

Intrinsic defects in Cu_2ZnSnS_4 supplementary material

This appendix gives details of an alternate interatomic potential to describe the pair-wise interactions of ions in Cu_2ZnSnS_4. This potential is referred to as potential 1 as it was developed, based on the work of Wright *et al.*, prior to the derivation of potential 2, upon which the work detailed in chapter 4 is based. Potential 1 is able to accurately describe the crystal structures of both kesterite and stannite Cu_2S to a high level of accuracy, however the form of the three-body term is unusual and proved to be incompatible with the implementation of the Nudged Elastic Band (NEB) methodology in GULP and also with the METADISE code, hence the derivation of potential 2.

The series of tables which follow give the parameters for potential 1 (Table B.1), a comparison of the calculated structure for kesterite and stannite to experimental data (Tables B.2 and B.3), the defect energies for various point defects (Tables B.4, B.5 and B.6) and the formation energies for various intrinsic defects based upon this data (Table B.7 and B.8)

We find that the results of potentials 1 and 2 are broadly comparable, based upon inspection of their reproduction of the crystal structure and the predicted formation energies for the various defects. However, one small difference between the formation energies calculated with the two potentials is that of the Cu Frenkel formation energy. Use of potential 1 gives a value of 0.97 eVdefect^{-1} and 0.96 eVdefect^{-1} in kesterite and stannite Cu_2ZnSnS_4 respectively. In contrast use of potential 2 changes this to 1.23 eVdefect^{-1} and 1.28 eVdefect^{-1}. While the magnitude of this change is no more significant than for the other defects it is of interest as formation of the Cu Frenkel is the only defect with a low enough formation energy for a small change to be significant. Potential 2 suggests that intrinsic formation of Cu Frenkel defects is not as favourable as initially thought, which is significant as it detracts from the theory

Table B.1: Parameters of potential 1 used to model Cu_2ZnSnS_4

Buckingham Term	A (eV)	ρ (Å)	c (eV/Å^6)	
S - S	1200.00	0.1490	0.0	
S - Cu	1226.95	0.2993	0.0	
S - Zn	672.28	0.3908	0.0	
S - Sn	1374.92	0.4038	0.0	
Three Body	k(eV/rad^2)	Θ_0(°)	ρ_1/ρ_2(Å)	Cut-off (Å)
S Shell - Zn Core - S Shell	0.942834×10^{07}	109.4700	0.3	12.0
Torsional	k_t(eV)	m/n	(Å)	r_{max} (Å)
Zn Core - S Shell - S Shell - Zn Core	0.005	+1/+3	2.5	3.0
Species	Core charge (e)	Shell Charge (e)	Spring Constant k(eV/Å^2)	
S	1.03061	-3.03061	13.302743	
Cu	1.0	-	-	
Zn	2.0	-	-	
Sn	4.0	-	-	

Table B.2: Comparison of calculated lattice parameters and bond lengths in kesterite Cu_2ZnSnS_4(potential 1) with experimental data.

Property		Expt	Calc.	Δ	%
a, b	/Å	5.43	5.44	0.003	0.06
c	/Å	10.86	10.74	-0.115	-1.06
Volume	/Å^3	320.56	317.53	-3.03	-0.94
$\alpha = \beta = \gamma$	(°)	90	90	0	0
Cu(1)-S	/Å	2.334	2.244	-0.090	-3.86
Cu(2)-S	/Å	2.332	2.278	-0.054	-2.32
Zn-S	/Å	2.334	2.374	0.040	1.71
Sn-S	/Å	2.409	2.501	0.092	3.82

Table B.3: Comparison of the calculated lattice parameters and bond lengths in stannite Cu_2ZnSnS_4)[potential 1) with experimental data.

Property		Expt	Calc.	Δ	%
a, b	/Å	5.434	5.416	-0.018	-0.32
c	/Å	10.856	10.712	-0.144	-1.33
Volume	/Å^3	320.560	314.262	-6.298	-1.96
$\alpha = \beta = \gamma$	(°)	0	0	0	0
Cu(1)-S	/Å	2.409	2.231	-0.178	-7.39
Cu(2)-S	/Å	2.332	2.231	-0.101	-4.33
Zn-S	/Å	2.334	2.405	0.071	3.04
Sn-S	/Å	2.334	2.504	0.170	7.28

that $Cu_i^{\cdot}$ migration could contribute towards Cu mobility in Cu_2ZnSnS_4 at normal temperatures, as if a defect is not present its ability to move is inconsequential.

Migration paths denoted as interlayer indicate Cu ion migration between the cation

Table B.4: Defect energies for vacancy defects in kesterite and stannite Cu_2ZnSnS_4 (potential 1)

Type of Defect	Symbol	Defect formation energy /eV	
		Kesterite	Stannite
Cu(1) vacancy	V'_{Cu}	6.21	6.26
Cu(2) vacancy	V'_{Cu}	6.24	6.26
Zn vacancy	V''_{Zn}	19.67	19.53
Sn vacancy	V''''_{Sn}	72.65	71.33
S vacancy	$V^{\cdot\cdot}_{S}$	20.59	20.38

Table B.5: Defect formation energies (E_F) for interstitial defects in kesterite and stannite Cu_2ZnSnS_4 (potential 1)

Interstitial		Kesterite		Stannite	
Species	Coordinates	layer	E_F /eV	layer	E_F /eV
Cu'_i	(0,$^1/_2$,0), (0,$^1/_2$,$^1/_2$), ($^1/_2$,0,0), ($^1/_2$,0,$^1/_2$)	CuSn	-4.27	CuCu	-3.99
Cu'_i	($^1/_2$,$^1/_2$,$^1/_4$), (0,0,$^1/_4$), ($^1/_2$,$^1/_2$,$^3/_4$), (0,0,$^3/_4$)	CuZn	-4.09	ZnSn	-4.35
Zn''_i	(0,$^1/_2$,0), (0,$^1/_2$,$^1/_2$), ($^1/_2$,0,0), ($^1/_2$,0,$^1/_2$)	CuZn	-12.62	CuCu	-12.74
Zn''_i	($^1/_2$,$^1/_2$,$^1/_4$), (0,0,$^1/_4$), ($^1/_2$,$^1/_2$,$^3/_4$), (0,0,$^3/_4$)	CuSn	-12.42	ZnSn	-13.15

Table B.6: Defect energies for substitutional defects in kesterite and stannite Cu_2ZnSnS_4 (potential 1)

Impurity	Defect energy /eV	
	Kesterite	Stannite
Cu'_{Zn}	12.11	12.04
Cu'''_{Sn}	62.49	62.17
$Zn^{\cdot}_{Cu}$	-11.00	-11.08
Zn''_{Sn}	47.85	47.69
$Sn^{\cdot\cdot}_{Zn}$	-43.31	-43.24
$Sn^{\cdot\cdot\cdot\cdot}_{Cu}$	-52.32	-52.82

Table B.7: Defect formation energies for a range of Schottky type and Frenkel defects in kesterite and stannite Cu_2ZnSnS_4 (potential 1)

Defect	Equation	Defect formation energy /eV			
		kesterite		stannite	
		process	per defect	process	per defect
Full Schottky	4.1	30.81	3.85	28.66	3.58
Cu_2S Schottky	4.2	6.31	2.10	6.17	2.06
ZnS Schottky	4.3	6.80	3.40	6.45	3.22
SnS_2 Schottky	4.4	30.02	10.01	28.27	9.42
Cu Frenkel	4.6	1.93	0.97	1.91	0.96
Zn Frenkel	4.7	7.05	3.52	6.38	3.19

layers, as shown in Figure 4.4a, and so involve net displacement of the migrating ion c coordinate. Whereas in migration paths denoted as intra-layer, the migrating ion has no net displacement in the c direction following its hop.

Table B.8: Defect energies ($E_{defectt}$) and cluster binding energies (E_{bind}) for antisite defects in kesterite and stannite Cu_2ZnSnS_4 (potential 1)

Defect	Equation	Isolated defects		Pair cluster		Binding energy	
		E_F / eV	E_F / eV defect^{-1}	E_F / eV	E_F / eV defect^{-1}	E_{bind} / eV	E_{bind} / eV defect^{-1}
kesterite							
Cu/Zn Antisite	4.10	1.11	0.55	0.50	0.25	-0.61	-0.31
Zn/Sn Antisite	4.11	4.54	2.27	1.94	0.97	-2.60	-1.30
Cu/Sn Antisite	4.12	10.17	5.09	4.67	2.34	-5.50	-2.75
stannite							
Cu/Zn Antisite	4.10	0.97	0.48	0.35	0.18	-0.62	-0.31
Zn/Sn Antisite	4.11	4.45	2.22	1.93	0.96	-2.52	-1.26
Cu/Sn Antisite	4.12	9.35	4.68	3.99	1.99	-5.36	-2.68

Table B.9: Energy barriers to Cu migration via V'_{Cu} and $Cu_i^{\cdot}$ migration mechanisms in kesterite and stannite Cu_2ZnSnS_4, calculated using a constrained minimisation approach (potential 1)

	V'_{Cu} migration		$Cu_i^{\cdot}$ migration	
	Path type	Migration barrier / eV	Path type	Migration barrier / eV
kesterite	interlayer	0.92	interlayer	0.9
	CuZn intra-layer	1.27	CuZn intra-layer	-
	CuSn intra-layer	1.11	CuSn intra-layer	1.34
stannite	2Cu intra-layer	1.38	ZnSn intra-layer	1.28

Appendix C

Polymorphism and surface properties of Cu_2ZnSnS_4 supplementary material

This appendix details the structures of the 49 symmetry independent cation ordering schemes upon which the work in chapter 5 is based. These 49 configurations are derived by investigating the permutations for arranging the Cu and Zn ions amongst the Cu/Zn sites in a $2 \times 1 \times 1$ supercell of Cu_2ZnSnS_4. They have been determined using the approach embodied in the Site Occupancy Disorder (SOD) code, refer to chapter 2 and the work of Grau-Crespo[62], and cover the complete configurational space for a supercell of this size.

Diagrams of the structures are given in Tables C.1-C.4 full relaxation of the lattice parameters and ionic positions was allowed during an energy minimisation calculation performed upon these structures using the VASP code.

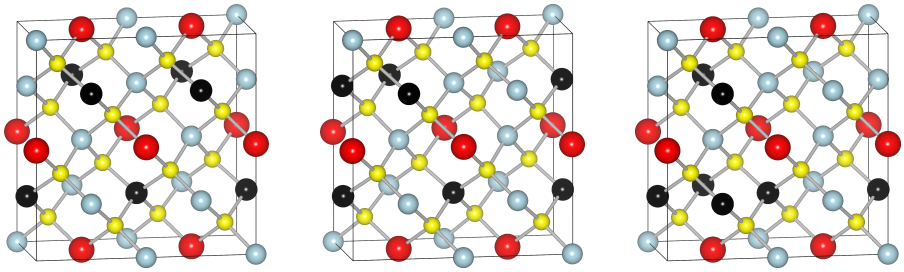

(a) Config 01 (b) Config 02 (c) Config 03

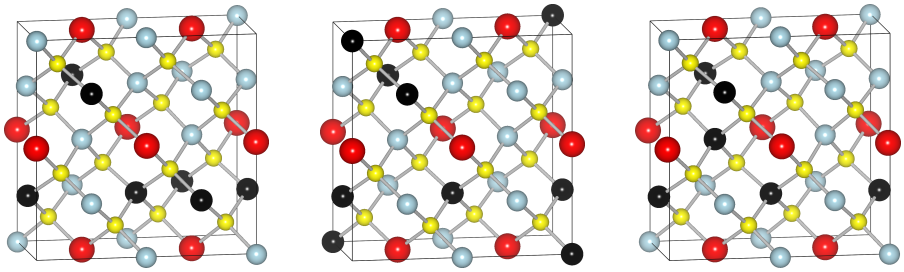

(d) Config 04 (e) Config 05 (f) Config 06

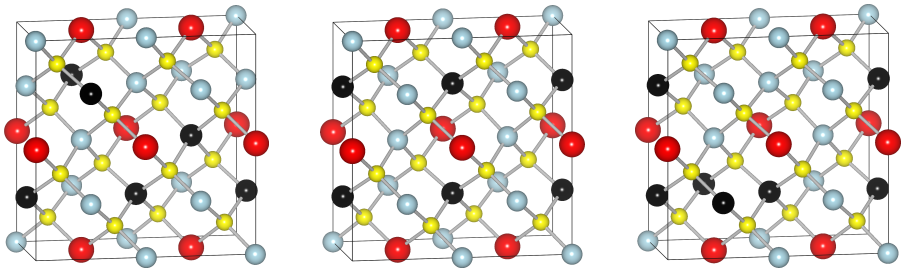

(g) Config 07 (h) Config 08 (i) Config 09

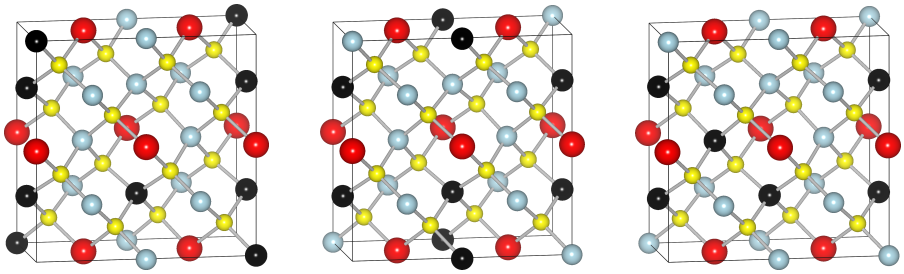

(j) Config 10 (k) Config 11 (l) Config 12

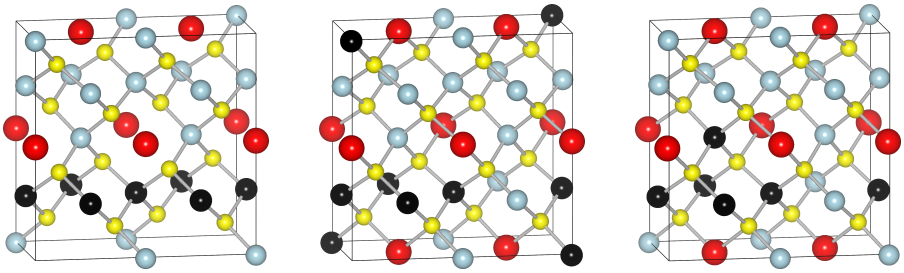

(m) Config 13 (n) Config 14 (o) Config 15

Figure C.1: Configurations of Cu_2ZnSnS_4 investigated with SOD set 1

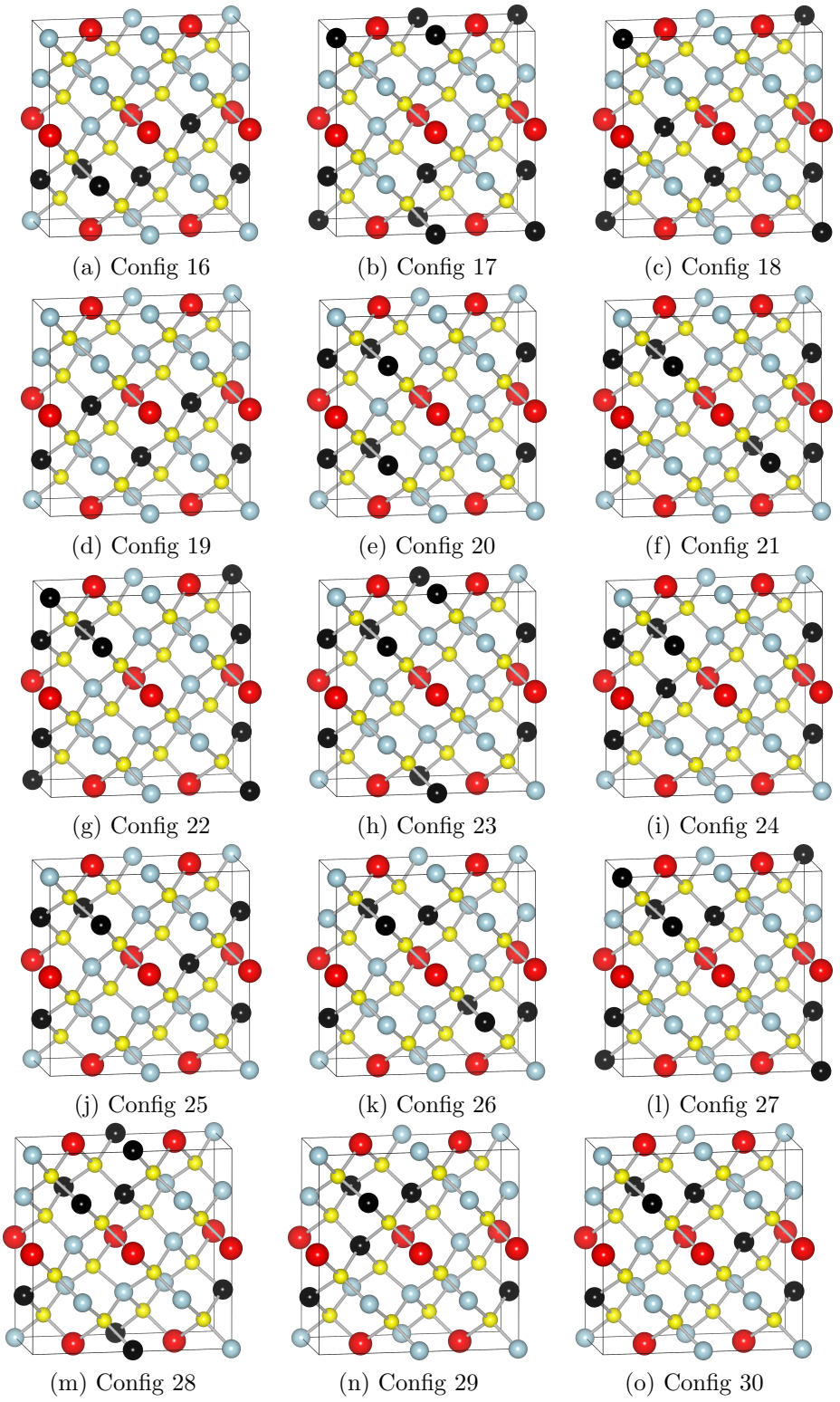

(a) Config 16 (b) Config 17 (c) Config 18

(d) Config 19 (e) Config 20 (f) Config 21

(g) Config 22 (h) Config 23 (i) Config 24

(j) Config 25 (k) Config 26 (l) Config 27

(m) Config 28 (n) Config 29 (o) Config 30

Figure C.2: Configurations of Cu_2ZnSnS_4 investigated with SOD set 2

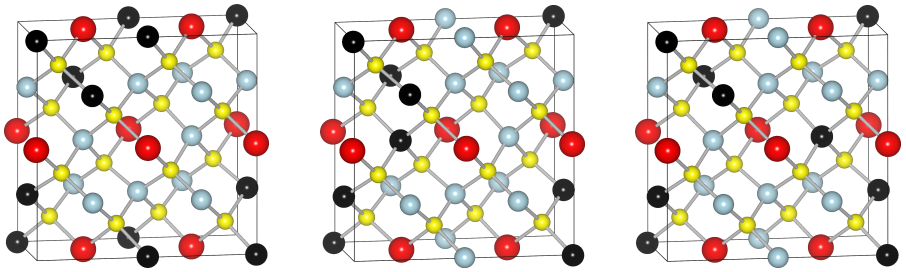

(a) Config 31 (b) Config 32 (c) Config 33

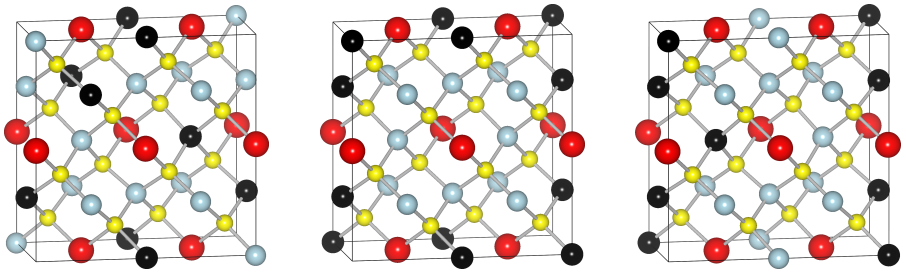

(d) Config 34 (e) Config 35 (f) Config 36

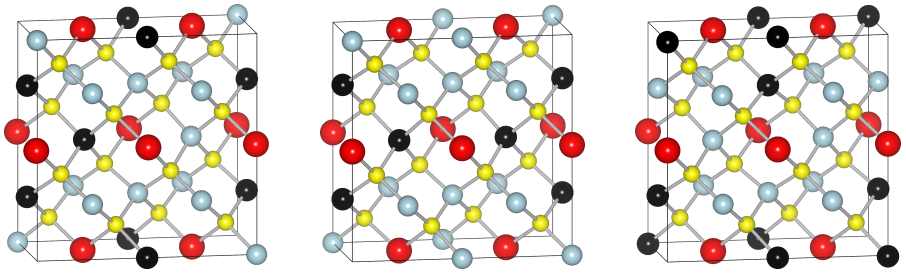

(g) Config 37 (h) Config 38 (i) Config 39

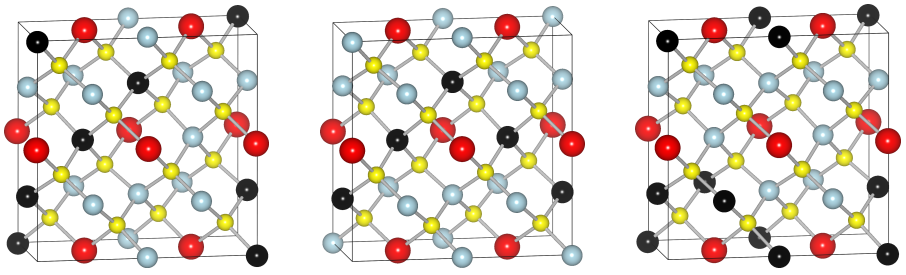

(j) Config 40 (k) Config 41 (l) Config 42

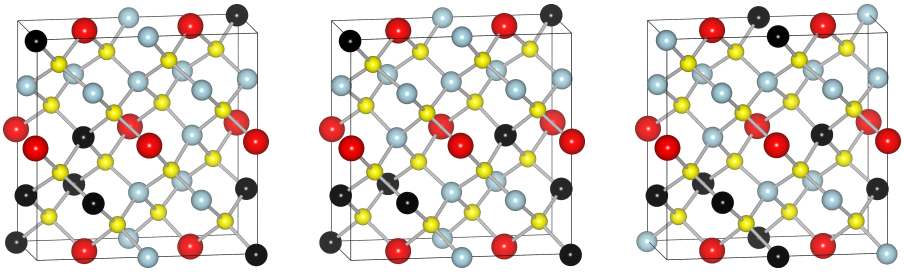

(m) Config 43 (n) Config 44 (o) Config 45

Figure C.3: Configurations of Cu_2ZnSnS_4 investigated with SOD set 3

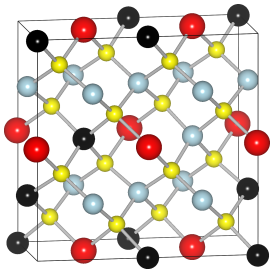

(a) Config 46

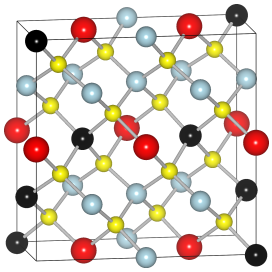

(b) Config 47

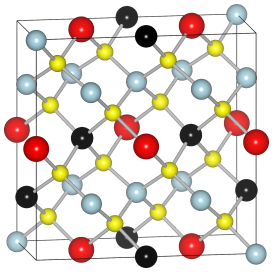

(c) Config 48

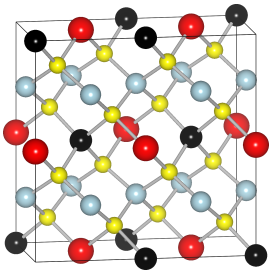

(d) Config 49

Figure C.4: Configurations of Cu_2ZnSnS_4 investigated with SOD set 4

Appendix D

List of investigated surfaces

Table D.1 gives a complete list of Miller indices for the surfaces of Cu_2ZnSnS_4 which were investigated as part of Section 5.3.3.

Table D.1: List of the miller indexes for which the surface properties of CZTS were investigated.

(0 0 1)	(0 -1 2)	(1 0 2)	(-1 1 2)
(0 0 -1)	(0 -1 -2)	(1 0 -2)	(1 -1 2)
(0 0 2)	(0 1 2)	(-1 1 0)	(1 1 2)
(0 0 -2)	(-1 0 0)	(1 -1 0)	(1 1 4)
(0 -1 0)	(1 0 0)	(1 1 0)	(2 2 0)
(0 1 0)	(-1 0 1)	(1 -1 1)	(2 2 2)
(0 -1 1)	(-1 0 -1)	(1 -1 -1)	(3 1 2)
(0 -1 -1)	(1 0 1)	(1 1 1)	
(0 1 1)	(1 0 -1)	(1 1 -1)	
(0 1 -1)	(-1 0 2)	(-1 -1 2)	

Appendix E

Published paper Thin Solid Films 2012

Appendix F

Published paper Physical Chemistry Chemical Physics 2012